UiT Norges arktiske universitet

Faculty of Science and Technology

Department of Physics and Technology

Exploring methane detection with Sentinel-2 data: capabilities for monitoring landfill emissions

Johanna Mankova Buseth

EOM-3901 Master's thesis in Energy, Climate and Environment 30 SP - June 2024

Abstract

Methane is an extremely potent greenhouse gas, as it is about 80 times more effective at trapping heat than carbon dioxide. To mitigate global warming and the related consequences, reducing our emissions of methane is crucial. Therefore, being able to detect unknown releases and monitor the effects of emission mitigation efforts is essential. A few satellites with methane monitoring as one of their main objectives have been launched and in recent years a range of studies have investigated the possibility of using other already existing satellites for the same purpose with promising results. About one fifth of the global annual methane releases originates from the waste sector, and monitoring of these areas can help mitigation efforts. Hence, this study centers around a one-year monitoring of a landfill in New Orleans, utilizing already published methods and the short-wave infrared bands (band 11 & band 12) of the freely available Sentinel-2 data. Landfills can act as both point sources and area sources, and remote sensing monitoring of such sites can help provide frequent emission data, as well as monitor areas that are inaccessible on foot.

The investigated methods show positive results over two different test sites with ideal background properties; however, we find that the inhomogeneous background and the operational-related changes in the surface of the landfill make it challenging to detect and monitor methane over the area.

Acknowledgements

I would like to express my gratitude to my supervisor at UiT The Arctic University of Norway, Malin Johansson, for her constant positivity, motivating supervision sessions, and for always being available to guide me through this work. I would also like to thank Charlotte Bishop at KSAT for inspiring the subject of this thesis and for her support

Furthermore, I am grateful to Dr. Daniel J. Varon at Harvard University for supplying the code for the multi-band multi-pass (MBMP) method and for his quick and comprehensive responses to my inquiries. His assistance has been invaluable.

I am very grateful for all the friends I have made throughout these five years, for the unreasonably long breaks, and all the fun we had through conversations and hours of playing pool and table tennis. A special thanks to my partner Nikolai, for always being there by my side and making even the most hectic exam periods enjoyable. These years would not have been the same without him, and I am excited about our adventures to come.

Finally, I would like to express my deepest gratitude towards my family. For challenging me, making me laugh and always having my back. I would not have been the same without them.

The thesis contains freely available Sentinel-2 Copernicus data (2019).

Table of content

1 Introduction

Methane is among the most impactful greenhouse gases that contributes to human induced global warming (IPCC 2023). The warming potential of methane is much higher than for carbon dioxide, though the atmospheric lifetime of methane is relatively short (10 years) compared to that for carbon dioxide (300 – 1000 years). Over a period of 100 years, methane is estimated to be about 30 times more effective at trapping heat than carbon dioxide, and in a 20-year period, by a factor of 80 (IEA 2021). Considering the warming potential of methane, as well as the shorter life span of the gas, a reduction of methane emissions is a necessary step towards mitigating global warming and reaching the goal of net zero greenhouse gas emissions by 2050. Knowledge about emission sources and rates is crucial for reducing the emissions, and remote sensing provides the necessary areal coverage and temporal repeats to detect and monitor methane emissions over time. For example, satellites can be used as an early warning system as they are enabling rapid identification of releases, which can help cease them and consequently reduce the total released quantities

Landfills are a major contributor to the global annual methane releases, accounting for about 20% of the anthropogenic emissions (IEA 2024). According to Ocko et. al (2021) 16% of methane emissions from landfills could be ceased at no cost. Monitoring of landfill emissions are commonly performed in-situ, through walking surface emission monitoring surveys, which can be difficult to perform due to limited accessibility or danger related to approaching certain areas e.g. due to slope steepness (Cusworth et. al 2024). In the United States, emission measurements are only required by law four times a year, meaning that great release events might pass unnoticed. Cusworth et. al (2024) performed an extensive airborne study monitoring about 1/5 of the open landfills in the U.S. and identified methane plumes in more than half of them. Their results agreed well with ground measurements, however, aerial surveys are resource demanding, hence the spatial and temporal coverage of satellites can be a useful complementary tool. For example, satellites can be used to monitor seasonal variations and to detect unknown release sources. A challenge with landfills is that they often constitute of both diffuse methane source as well as point sources. While diffuse sources can release significant amounts of methane, most satellite sensor retrieval methods have been developed for point sources, e.g. Varon et.al (2021) and Sanchez-García et. al (2022), Guanter et. al. (2021).

The goal of this study is to investigate the possibility of utilizing the freely available open-source Sentinel-2 satellite data to monitor methane emissions from landfills. The study centers around one-year monitoring over a landfill outside of New Orleans in the year of 2022. Two different methods, Varon et.al (2021) and Jia et.al (2022), developed to detect releases from point sources, are tested to determine which is the most suitable for the analysis, before the analysis itself is conducted.

This thesis is structured into a total of 11 chapters. Chapter 2 presents some background for the subject of the thesis, as it goes through how methane contributes to global warming, methane emission sources and emission monitoring. In Chapter 3 the necessary remote sensing theory for understanding the methods and challenges is reviewed. Further, Chapter 4 goes through satellites suitable for methane monitoring purposes, a range of previous studies, as well as the limitations of the respective satellites. In Chapter 5 the data used for testing and analysis is reviewed, before the methods are presented and evaluated in Chapter 6. In Chapter 7 the results from the New Orleans landfill site are presented and discussed, and the conclusion and suggestions for further research can be found inn Chapter 8 and 9.

2 Background

2.1 The greenhouse effect and global warming

To understand what greenhouse gases are, and how methane emissions contribute to global warming, an understanding of the greenhouse effect is necessary. Briefly explained, it is the process where certain gases in the Earth´s atmosphere trap heat resulting in surface temperatures suitable for life (Mamen & Benestad 2023). Gases with such absorption properties are what we know as greenhouse gases, and the most important ones are water vapor, carbon dioxide and methane. Even though some of the incoming solar energy is reflected back into space, most is absorbed by the Earth, causing the surface to heat. The surface then emits the heat as infrared radiation, which is absorbed by greenhouse gases, and reemitted in random directions, including back to Earth. This process of absorption and reemission happens continuously, and effectively traps heat in the atmosphere, causing the surface temperatures of the Earth to be about 15°C, compared to the no-atmosphere scenario where the average surface temperatures would be -18°C (Mamen & Benestad 2023). Figure 2.1 shows a schematic illustration of the greenhouse effect.

Increasing concentrations of greenhouse gases in the atmosphere causes stronger absorption and therefore more heat to be trapped by the atmosphere, resulting in increasing surface temperatures, also known as global warming. According to IPCC (2023) the global surface temperatures in the decade 2011-2020, were about 1.1°C higher than the average for 1850-1900, and greenhouse gas emissions due to human activity have, without doubt, been the driving force. Global warming has a great range of consequences impacting humanity directly, or indirectly, including more frequent extreme weather events (e.g. drought and extreme precipitation) and natural catastrophes (e.g. floods and landslides), and ecosystem disruptions (e.g. changes in phenology and the ranges where species can live) (IPCC 2023). In order to mitigate global warming and the related consequences, 194 states, as well as the European union, has agreed to aim for a limit of 1.5°C increase in temperature compared to preindustrial time. To achieve this goal, the greenhouse gas emissions must be reduced by 45% within 2030 and reach net zero by 2050 (United Nations n.d. (1) & (2)).

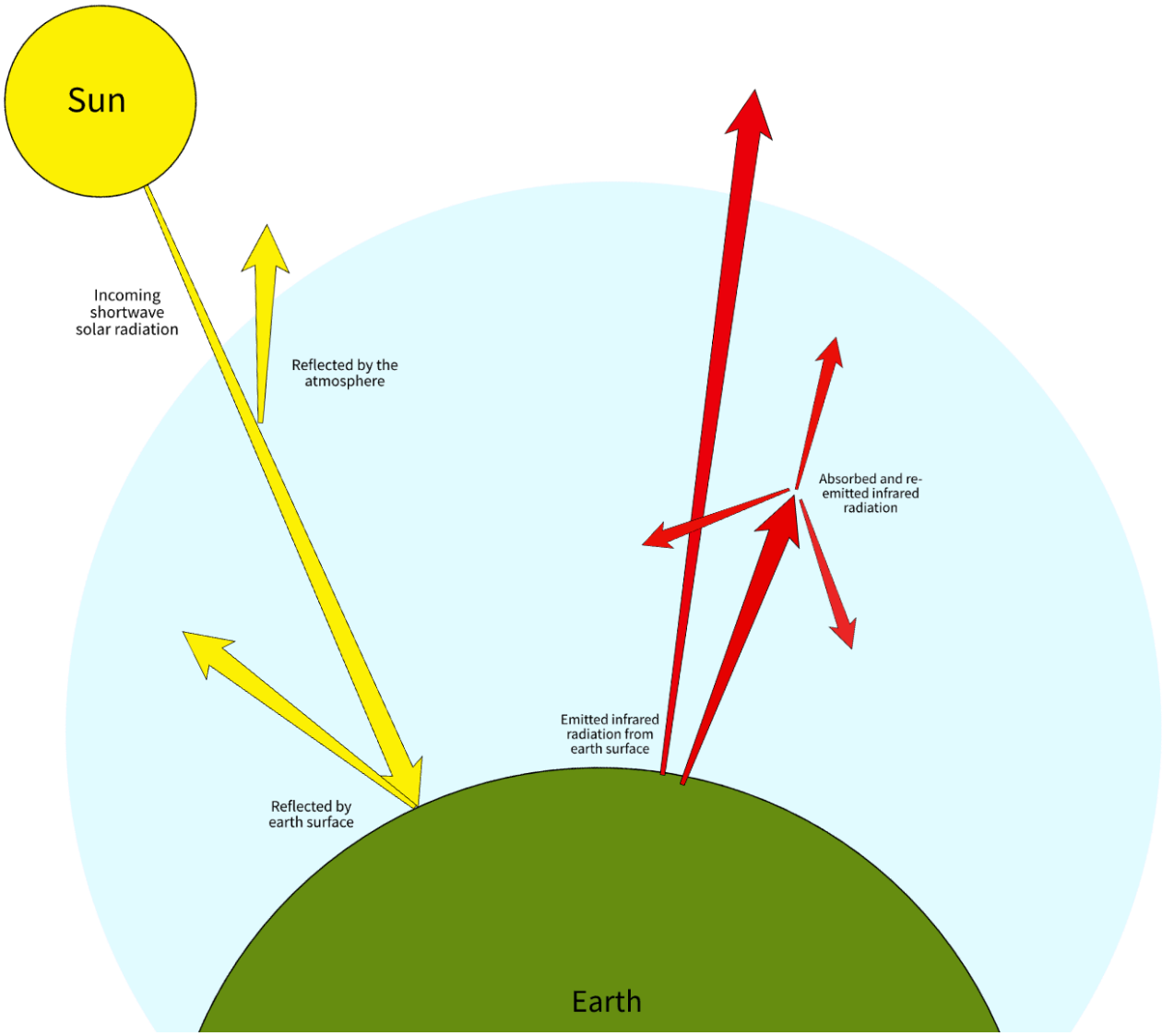

Figure 2.1 Schematic illustration of the greenhouse effect. Incoming solar radiation is reflected by the Earth´s surface and atmosphere or absorbed, causing the surface to heat. The Earth surface reemits the energy, which is partly absorbed and reemitted in all direction by atmospheric greenhouse gases, including back to the surface. Source: Buseth (2023) (2)

2.2 Methane emissions

In 2019 the atmospheric methane concentrations were 1866 parts per billion (ppb), which is an 156% increase from preindustrial time, and the highest value it has been for at least 800 000 years (IPCC 2023). According to the International Energy Agency (IEA), methane is responsible for about one third of global warming since preindustrial time, and with the increasing atmospheric concentrations the temperatures are predicted to continue to rise (IEA, 2023).

The global annual methane releases were estimated to be 576 million tons in the decade 2011-2020, including both anthropogenic and natural emission sources, which was an increase of 24 million tons compared to the annual average between 2003-2012 (Saunois et.al 2020).

Saunois et. al (2020) found that about 40% of the annual releases between 2008-2017 originated from natural sources, e.g. wetlands, thawing of permafrost and geological sources, whereas the rest are anthropogenic. Out of the anthropogenic categories in the study, agriculture and waste was found to be the most emitting sector, accounting for about 217 million tons methane annually, followed by the fossil fuel industry accounting for about 111 million tons. IEA (2024) provided updated numbers with estimates for the global methane emissions in 2023, where the estimated methane emissions from natural and anthropogenic sources were 583 million tons in total, which is an increase of 7 million tons compared to the 2011-2020 average. Their findings indicate a slight reduction in methane emissions from the combined agriculture and waste sector, however they point to an increase of about 17 million tons methane related to fossil fuels and the energy sector.

Methane releases can be categorized into two main groups, point source releases and diffuse releases (Saunois et. al 2020). Following the definition of Irakulis-Loitxate et. al. (2023), diffuse releases come from a large area where the methane is emitted from many different points (also known as area sources), whereas point source releases origin from single, relatively small, sources, emitting large volumes of the gas. An example of a diffuse emission source is wetlands, that contributed approximately one third of the total methane releases in 2023 (IEA, 2024). Point sources, on the other hand, are typically found in relation to human activity, such as unlit flares in oil and gas production facilities. Landfills that are investigated in this thesis can contribute through point source releases, often related to operational activities, e.g. construction/maintenance, or malfunctions in gas-capture-systems, and through diffuse releases (Cusworth et. al 2024). The latter occurs from e.g. diffusion through soil layers and cracks in the cover due to drought, strong precipitation etc. (Cusworth et. al 2024).

Globally, the waste sector accounted for about 20% of the anthropogenic methane emissions in 2023, releasing more than 70 million tons of methane (IEA 2024). Methane form through anaerobic bacterial decomposition of organic material, and in landfills the gas form through decay of sludge and buried organic waste (Britannica 2024, Blindheim & Levy 2023, Cusworth et. al 2024).

2.3 Methane emission monitoring

Understanding the methane emissions origin and related release volumes is important when working towards emission reductions, and therefore monitoring of methane releases is

essential. There are different approaches to methane monitoring, and generally we distinguish between bottom-up and top-down approaches.

Bottom-up approaches include, e.g., on-site measurements, and utilizes a statistically representative selection to calculate standardized emission factors which are then extrapolated to a larger population to estimate total emissions (Allen 2014). For example, Sheng et al. (2019) created a high-resolution overview over methane emissions from coal mining in China, based on existing data from over 10 000 mines. There are, however, some limitations to the accuracy of bottom-up approaches, one being the difficulty of getting an adequately sized representative sample (Allen 2014). Another major challenge with these approaches is that unpredictable events, such as accidents in the oil-and gas sector, can lead to large methane releases, and are often not included in bottom-up inventories (IEA 2023).

Top-down estimates are done by measuring the atmospheric concentration of methane from above, including from tall observation-towers on site, as well as using sensors mounted on aircrafts or satellites (MDE 2023). Because methane has distinct absorption properties in the short-wave infrared (SWIR) parts of the electromagnetic spectrum, passive satellite sensors that have bands covering the respective wavelengths can be used for monitoring purposes. Some satellites have methane monitoring as one of the main missions, such as GOSAT (launched in 2009), GHGsat (launched in 2016) and MethaneSat (launched in 2024). However, there are several other satellites with bands covering the required SWIR spectrum, and in the last few years the potential for monitoring using, e.g., Sentinel-2, WorldView-3 and PRISMA has been explored (Varon et. al 2021, Sánchez-García et.al. 2022 & Guanter et.al. 2021). The top-down measured atmospheric methane concentrations can either be used to quantify emission rates from a single monitored release source, or be fed into atmospheric inversion models to analyze fluxes (National Academies of Sciences, Engineering, and Medicine. 2018).

In order to improve methane monitoring methods, and regional and global emission estimates, a combination of top-down and bottom-up approaches must be applied. Accidental releases are challenging to monitor instantaneously from the ground and here satellites and airborne methods can play a vital role. Moreover, as satellites can monitor methane over large areas with frequent repeats, they can help advance the monitoring of global emissions by identifying origins, concentrations and durations of releases. They provide an especially useful tool when it comes to identifying, and monitoring of, unknown releases and accidents that bottom-up methods do not account for, as lack of knowledge about time and place

hinders the use of observation towers and aircrafts. Through remote sensing, areas that should be monitored in greater details from the ground can be identified, allowing for the establishment of ground monitoring systems. Top-down systems can also be used to monitor locations where remediating efforts has been established, to evaluate the effect. In this thesis Sentinel-2 satellite data will be used, due to the free and open data policy and relatively high resolutions (see Chapter 4 and Table 4.2).

3 Passive remote sensing theory

Remote sensing is the process where physical information is obtained from a distance, by a sensor that is not in contact with the observed object, usually the Earth's surface. The information is transmitted to the sensor through electromagnetic (EM) radiation reflected or emitted from the object. To detect methane, we make use of passive sensors, utilizing the sun as the illumination source by measuring the reflected EM radiation from the Earth's surface after it has been transmitted through the atmosphere. Figure 3.1 is a simple illustration of how incoming solar radiation interacts with the atmosphere and the Earth's surface, before it reaches the satellite sensor.

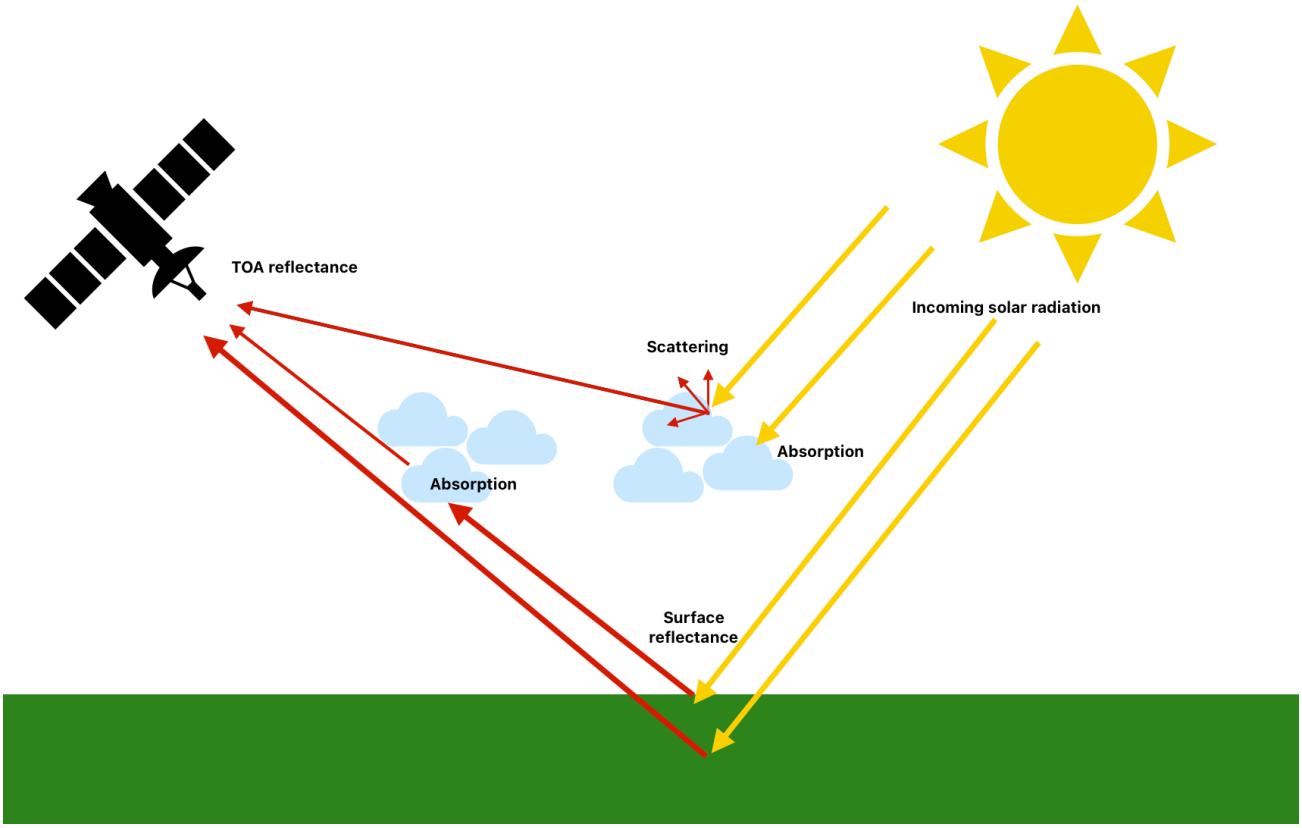

Figure 3.1. Illustration of how passive satellite sensors utilize the sun as an illumination source. Incoming solar radiation is either reflected, scattered or absorbed by the atmosphere, or transmitted through it. The transmitted radiation is then reflected from the Earth surface. The satellite sensor detects the top of atmosphere (TOA) reflectance, which is the combined reflectance measured from the Earth's surface and atmosphere.

3.1 Electromagnetic spectrum and methane absorption properties

In classical physics, EM energy is transferred through EM waves that are propagating at the speed of light and are characterized by their wavelength and amplitude. The EM spectrum

ranges from gamma rays in the short-wave end to radio waves in the other end, as shown in Figure 3.2. The energy carried by the EM waves increases with decreasing wavelength and vice versa.

Only wavelengths between ca 400nm -700nm are visible to the human eye, covering the colors of the rainbow. Even though most of the EM spectrum falls outside of the visible range, all EM radiation behaves similarly to visible light, as the radiation can be reflected or absorbed when interacting with an object. Due to their composition, all substances have unique absorption spectrums, and these can be used to identify the observed substance. When sunlight is transmitted through a gas, one can measure what wavelengths are absorbed and hence identify what molecules the gas consists of. To understand why different substances, have different absorption properties, and therefore why some gases are greenhouse gases and others not, one must look at the differences at a molecular level.

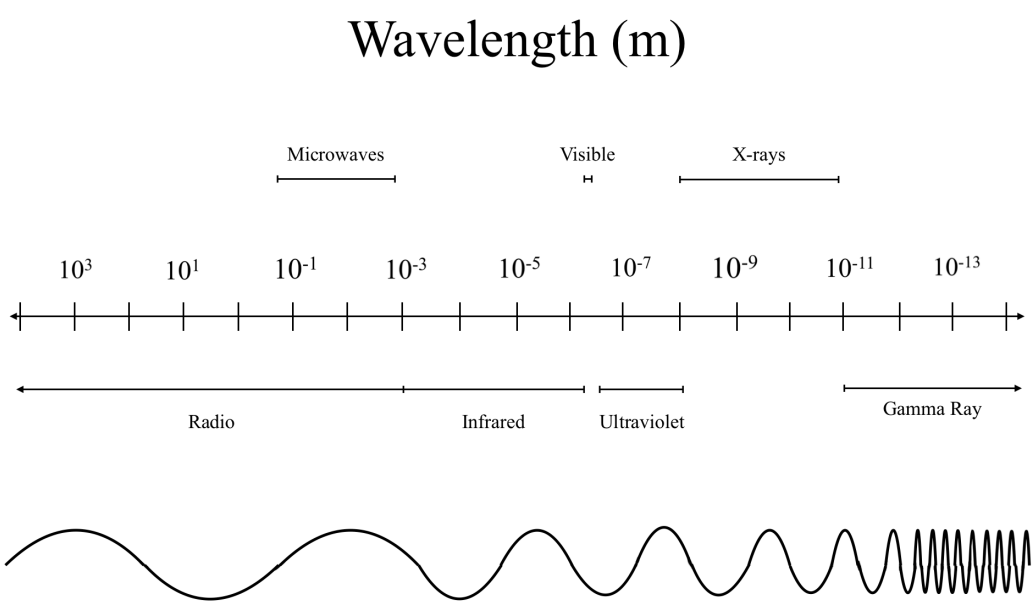

Figure 3.2 Simple overview of the EM-spectrum, ranging from radio waves to gamma rays. The wavelength ranges for each of the categories are obtained from Wiström et. al (2021).

Gas molecules can exist in different distinct energy levels, where the lowest possible level is called the ground state. EM radiation corresponding to the gap between different energy levels can easily be absorbed, exciting the molecule to a higher energy level. An excited molecule is not stable, and will shortly go back to its ground state, re-emitting the absorbed radiation in a random direction. A molecule has energy due to rotation and vibration, as well as electron energy, and the energy required for excitation is different between the three energy

modes. While electronic energy transitions absorb wavelengths in the energy dense UV-, Visible and Near infrared (NIR) parts of the EM spectrum, the vibrational modes are sensitive to infrared (IR) radiation, and the rotational modes to the microwave region. Methane and other greenhouse gases are triatomic, allowing more vibrational modes than diatomic gases, hence they absorb IR-radiation, contrary to the most common compounds of the atmosphere, nitrogen, and oxygen. The short-wave infrared (SWIR) spectrum is a subset of the IR-spectrum and covers wavelengths between 1400-3000nm. As shown in Figure 3.3, methane has strong absorption in the SWIR-spectrum, making sensors covering the absorption peaks within these wavelengths suitable for methane detection.

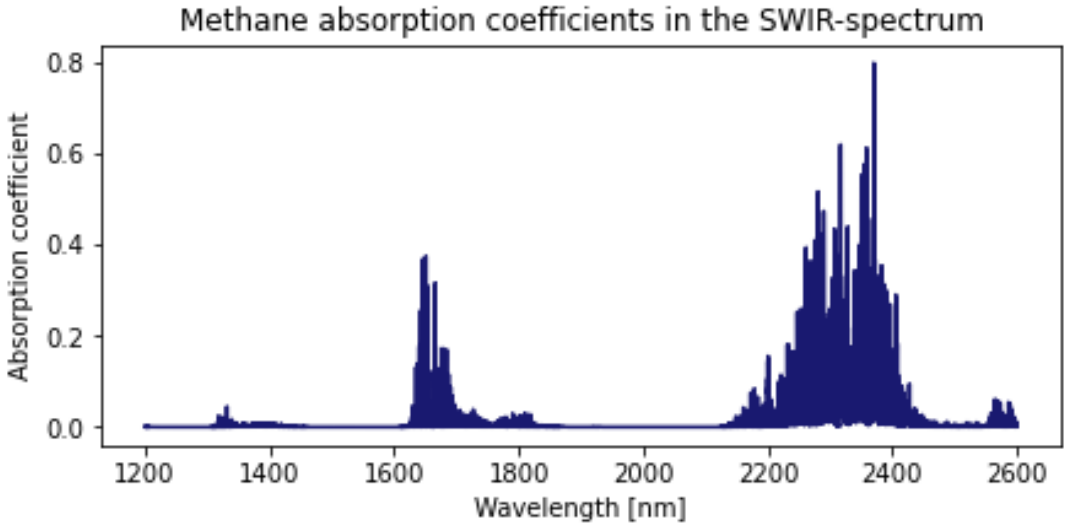

Figure 3.3 Methane absorption coefficients in the SWIR-spectrum. The strongest absorption find place for wavelengths between 2200 nm and 2400nm. Additionally, there is a smaller absorption peak between 1600-1700 nm. Absorption data obtained from HITRAN (Kochanov et. al. 2016)

3.2 Passive satellite properties important for methane detection

Passive satellites are not able to measure the location within the atmosphere where the absorption takes place, resulting in the atmosphere being viewed as one thin layer. However, the travel path of the electromagnetic radiation is crucial, as it provides information about how much mass of air the radiation has been transmitted through, and therefore also the length where the radiation is exposed to the atmospheric methane. The radiation travel path depends on two parameters, the observing angle of the satellite, as well as the solar zenith angle at time of image acquisition. The observing angle (θ), often also referred to as viewing angle, is the angle which the sensor is pointed to the Earth surface with, compared to the nadir angle, which is directly below the satellite. The solar zenith angle (β) is the angle between the

sunbeam and the vertical. Both the solar zenith angle and the satellite observing angle is usually provided in the metadata which comes with the satellite imagery. Figure 3.3 shows a schematic illustration of the angles of interest. The travel path is accounted for by the air mass factor, which depends on both the solar zenith angle and the sensor observing angle. This will be elaborated in the methods section 6.1.2.

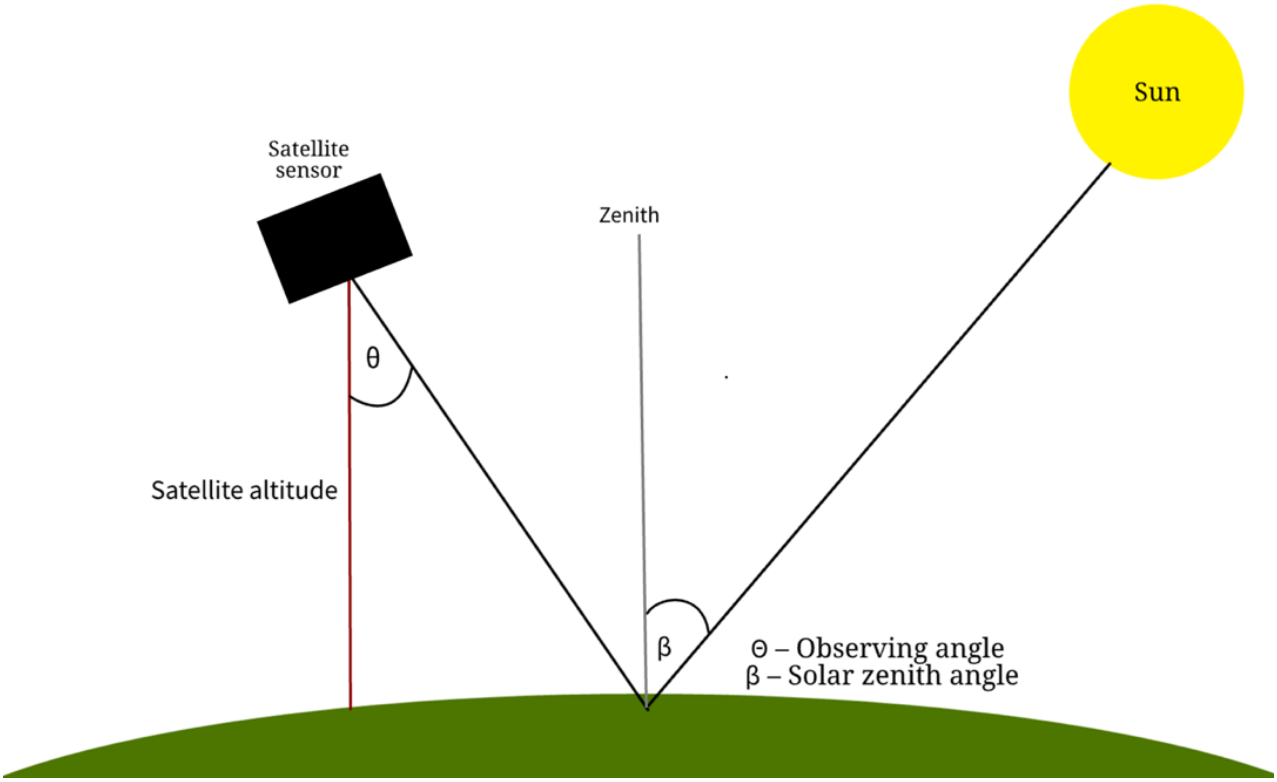

Figure 3.4 Schematic illustration of some satellite specifics important for methane detection.

In addition to the observing angle and the solar angle, information about the satellites orbit is crucial for successful methane monitoring. For the temporal resolution (see section 3.3), the frequency at which imagery can be repeated is important. Most satellites with Earth observation purposes orbit the Earth consistently, through a series of repeating orbits. The repeat cycle is the time it takes for a satellite to image the Earth at the same time in the same orbit, resulting in the same observing angle. Areas may be covered by multiple orbits, and the revisit time, which is the time between imagery is obtained over the same location, can therefore be shorter than the repeat cycle, depending on where the site of interest is located.

3.3 Sensor properties and resolutions to consider for methane monitoring

Passive satellite sensors acquire data within different bands, and each of the bands cover a range of wavelengths. A band, or a combination of multiple bands, make up satellite images. For example, true color images are images composed as perceived by the human eye, and consists of three spectral bands, red, green, and blue. Therefore, to create a true color image, the satellite must capture data within the red, green, and blue part of the spectrum. The range which the satellite uses for each of the different bands is called the band width. For example, the red band 4 of Sentinel-2 covers the wavelengths between 640 nm and 680 nm, and hence have a band width of 30 nm (Sentinel-2 MSI User Guide). The central wavelength of a band is the middle value of the band range. For the red band of Sentinel-2 the central wavelength is about 665 nm. The sensor perceives all wavelengths within the band range the same, and wavelengths within the same band are therefore not distinguishable. All optical satellites capture reflectance data in one or more spectral bands, covering different parts of the electromagnetic spectrum depending on their area of use.

The band widths and central wavelengths, as well as the revisit time, are important for the resolution of a satellites data, and therefore also for the detection limits. Moreover, for methane detection we need to consider the i) spectral, ii) spatial and iii) temporal resolutions.

The spectral resolution refers to the spectral detail level the sensor is capable to provide, and thus the ability to distinguish different wavelengths from each other. The spectral resolution depends on the total number of imaging bands of the sensor, and their respective bandwidths, as smaller bandwidths and more bands make more detailed spectral information available.

The spatial resolution is defined by the ground area represented within each pixel of the imagery. For example, the imagery acquired by the Sentinel-2 satellites within SWIR wavelengths, have a spatial resolution of 20 meters. This means that each pixel in the data covers an area of about 400 square meters on the ground, and smaller objects than this will not be possible to accurately resolve.

The ability to detect and monitor methane releases depend on the frequency that an area is imaged, determined by the temporal resolution. The temporal resolution refers to the revisit time of the satellite, or how often the sensor can obtain new imagery over the same area. Passive satellites typically have a revisit time within the range of a few days to a few weeks.

Additionally, the frequency of which meaningful information can be obtained about the atmosphere and surface properties is weather dependent, as cloud coverage may prevent useful satellite data.

Satellites with a high spatial resolution can detect smaller methane releases and are better for identifying the exact location of the emission source, whereas satellites with high spectral resolution within the wavelengths coinciding with the methane absorption spectrum can detect lower concentrations and give more accurate concentration estimates. The temporal resolution is crucial because methane releases often occur sporadically and over short periods of time, and a higher temporal resolution increases the likelihood of capturing an event. A high revisit frequency can, for example, be a crucial tool towards reducing the time of discovery and intervention for large methane releasing anthropogenic accidents, and therefore reducing the total emissions. One way to increase the temporal resolution is to combine a range of different satellite sensors, though the spatial and spectral resolutions for these sensors will still be sensor specific.

4 Satellites used for methane detection

The SWIR spectrum is highly sensitive to methane, as shown in Figure 3.3, and satellites obtaining data within these wavelengths can therefore be used for methane detection followed by release volume estimates. The satellite sensor detects the amount of radiation that is transmitted from the Earth's surface and since the presence of methane in the atmosphere reduce the transmitted energy, the signal detected by the sensor is reduced. Consequently, areas with higher methane concentrations have lower measured reflectance compared to their surroundings, and in theory, a methane plume can therefore be visible as a darker spot in imagery obtained within methane sensitive SWIR- bands. Therefore, methane can be detected and quantified through the measured reflectance by comparing an image with methane to one without methane. There are two main ways to do this; i) compare imagery obtained within the same methane sensitive band during two separate satellite passes, one with and one without methane present, or ii) compare the reflectance of a methane sensitive band to a non-methane sensitive band from the same satellite pass.

Satellite missions with methane monitoring and detection as specific objectives have been launched, e.g., GHGsat, GOSAT and MethaneSAT, though other satellites that collect data using methane sensitive bands can also be exploited for this purpose, e.g. Sentinel-2, WorldView-3 and Landsat-8. The inclusion of other satellite sensors ensures more frequent data collections, as well as allowing establishment of time series of detection and monitoring back in time, due to the often-extensive data archives. In recent years a large range of studies has been performed using imagery from different satellites and various methods to detect methane releases, and an overview of some of these studies, together with the satellites used are presented in Table 4.1. Common to all the satellites in this table is that they were not launched with methane monitoring as their main mission objective, however they are useful for that purpose, as they have bands covering high-absorption regions of the SWIR-spectrum (see Table 4.2). As one can see from Table 4.1, out of the presented satellites, Sentinel-2 is the most commonly used, largely a consequence of its open and free data policy and relatively high resolutions.

Table 4.1. Overview of methane detection studies using satellite imagery. The satellite sensors used for the different studies are indicated with Xs, and the following abbreviations have been used WorldView-3 (WV-3), Sentinel-2 (S2), Sentintel-3 (S3), Sentinel-5p (S5P), Gaofen-5 (GF5), Ziyuan-1 (ZY1), Hyperspectral Precursor and Application Mission (PRISMA) and Landsat-8 (L8). Extended from Buseth (2023)(1).

	Satellites used							
Scientific study	**WV3**	**S2**	**S3**	**S5P**	**GF5**	**ZY1**	**PRISMA**	**L8**
Sánchez-García et.al. 2022	**X**							
Irakulis-Loitxate et.al 2021					**X**	**X**	**X**	
Pandey et.al 2023		**X**	**X**	**X**				
Varon et.al. 2021		**X**						
Zhang et.al. 2022		**X**						
Guanter et.al. 2021							**X**	
Ehret et.al. 2022		**X**						
Hayden & Christy 2023	**X**							
Groshenry et.al 2022							**X**	
Gorroño et.al 2023		**X**						
Chen et. al 2023				**X**				
Lorente et.al 2021				**X**				
Dogniaux et.al 2023		**X**						**X**
Irakulis-Loitxate et.al 2022	**X**							**X**
Jia, M et. al. 2022		**X**						**X**
De Gouw et. al 2020				**X**				
Radman et. al 2023		**X**						
Lorente et. al 2022				**X**				

In Table 4.2 the most commonly used satellites for methane detection are presented together with the sensor specific spectral, spatial, and temporal resolutions. They are important for the detection limitations both with respect to the areal extent of a methane plume and the minimum concentrations that can be measured. Note that only the specifics for the methane sensitive bands in the SWIR-region are included.

Of the satellites presented in Table 4.2, PRISMA and WorldView-3 gather data when tasked, and the rest do it continuously. WorldView-3 data is made available upon request for a fee,

and PRISMA data is made available upon request. The data from all other presented satellites are open access and freely available.

*Table 4.2. Overview of satellite specifics for the sensors commonly used for methane detection. *PRISMA carries a hyperspectral sensor collecting data within two bands, divided into 239 channels covering the visible-near infrared and near infrared- SWIR region of the EM-spectrum, and is therefore not listed with band names and respective central wavelengths and bandwidths (eoPortal 2012).*

Satellite	**Central wavelength**	**Band width**	**Spatial resolution**	**Revisit time**
Sentinel-2[1]				5 days
Band 11	~ 1610 nm	90 nm	20 m	
Band 12	~ 2110 nm	174 nm	20 m	
Sentinel-3[2]				<1 day
Band 5	1613 nm	61 nm	500 m	
Band 6	2256 nm	50 nm	500 m	
Sentinel-5p[3]				< 1 day
SWIR-1	1633 nm	85 nm	7 km	
SWIR-3	2345 nm	80 nm	7 km	
PRISMA[4]				7 days
Hyperspectral	*	*	30 m	
WorldView-3[5]				<1 day
Band 3	1660 nm	40 nm	3.7 m	
Band 7	2260 nm	70 nm	3.7 m	
Band 8	2330 nm	50 nm	3.7 m	
Landsat-8[6]				16 days
Band 6	1610 nm	80 nm	30 m	
Band 7	2150 nm	80 nm	30 m	

[1]. Sentinel-2 MSI User Guide (n.d.). [2]. Sentinel-3 SLSTR User guide (n.d.) [3]. Sentinel-5P TROPOMI User Guide (n.d.) & Sentinel-5P (n.d). [4]. PRISMA (2012) [5]. WorldView-3 (n.d.) [6]. Landsat-8.

Images from the satellites presented in Table 4.2 have different detection limits (kg/h), and these depend on the satellite sensors used, the method used to obtain the methane concentrations, and the background properties, among others. In Table 4.3, identified detection limits are presented. Note that not all studies presented in Table 4.1 have identified detection limits, and where no such limit has been identified the studies have been omitted

from Table 4.3. As one can see, the detection limits are not stated for a good share of the papers. However, the table suggests that Sentinel-2 detections of releases down to 500 kg/hour under ideal conditions are possible (Gorroño et. al 2023). It is worth noticing that the high spatial and spectral resolution offered by WorldView-3 enables the lowest detections limits, indicating that for small scale localized releases this might be the preferred satellite.

Table 4.3. Detection limits identified within a range of scientific studies. Modified from Buseth (2023)(1).

Scientific study	**Detection limits**	**Satellite used**
Sánchez-García et.al. 2022	< 100 kg/h	WorldView-3
Irakulis-Loitxate et.al 2021	>500 kg/h	Gaofen-5, Ziyuan-1, PRISMA
Pandey et.al 2023	8000 kg/h – 20 000 kg/h	Sentinel-2, Sentinel-3, Sentinel-5p
Varon et.al. 2021	>2600 kg/h	Sentinel-2
Guanter et.al. 2021	500 – 2000 kg/h	PRISMA
Ehret et.al. 2022	1500 – 12 000 kg/h	Sentinel-2
Hayden & Christy 2023	>33 kg/h	WorldView-3
Gorroño et.al 2023	500 – 2000 kg/h	Sentinel-2
Irakulis-Loitxate et.al 2022	500 kg/h	WorldView-3, Landsat-8

In this thesis, it was decided to focus on two different methods developed using Sentinel-2 data, further presented in Section 6. The satellite was chosen due to its freely available data with relatively high resolutions (see Table 4.2), the frequent occurrence in the earlier published work, and the potential to detect releases down to 500 kg/h.

5 Data

In this thesis focus will be on utilizing Sentinel-2 data for methane monitoring. Two test sites with known release fluxes are used, as well as a full year (2022) of monitoring of a landfill in New Orleans.

5.1 Sentinel-2 data

The Sentinel-2 constellation consists of the two satellites, Sentinel-2A and Sentinel-2B, launched in June 2015 and March 2017 respectively. They are operated by the European Space Agency (ESA) and provide freely available global data. The satellites both carry a multispectral instrument (MSI), collecting data in 13 spectral bands, distributed over the visible, SWIR and near IR wavelengths. Two of the bands are in the SWIR part of the spectrum and can be used for methane monitoring, band 11 (B11) and band 12 (B12). The bands are indicated in Figure 5.1 together with the methane absorption spectrum. The band widths are 90 nm for B11 and 180 nm for B12, and the spatial resolution within these bands is 20 meters. The satellites are in the same sun synchronic orbit, which means that every repeated overflight happens at the same local time, and the satellites fly at a mean altitude of 786 km. As each of the two satellites have a revisit time of ten days, new imagery can be obtained minimum every fifth. For more detailed information about the satellite specifications see the Sentinel-2 MSI User guide by ESA (n.d.), and Table 4.2.

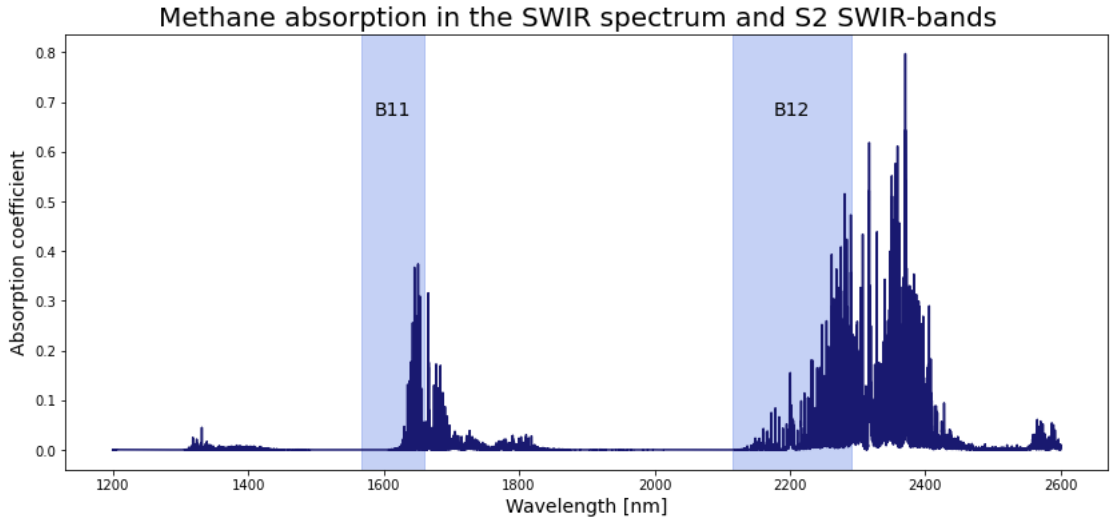

Figure 5.1 Methane absorption spectrum in the SWIR region of the electromagnetic spectrum and the bandwidths of Sentinel-2 B11 and B12. Source: absorption data obtained from Hitran (Kochanov 2016)

Sentinel-2 satellite data is downloadable through multiple data portals, and with different levels of processing. Level 1C data is top of atmosphere (TOA) reflectance, whereas level 2A data is atmospherically corrected surface reflectance (Sentinel-2 MSI Technical Guide n.d.). For the methods in this study the level 1C data products were used, as we are interested in the atmospheric composition. The image data used in this thesis was mainly downloaded from EO-browser provided by Sentinelhub at https://apps.sentinel-hub.com/eo-browser , however all metadata, and imagery for some scenes, were obtained from Creodias at https://explore.creodias.eu/.

5.2 Test data

To test and compare the two methods used in this study (Section 6), Sentinel-2 satellite data collected over two blind test sites presented in Sherwin et al. (2023 and 2024) were used. Sherwin et. al 2023 and Sherwin et. al 2024 performed controlled methane releases to test and compare different retrieval methods by multiple participating teams. The participating teams were not informed about the release rates and the aim was to evaluate whether the teams were able to identify releases, and if so, how accurate estimates they were able to derive. An overview of the in-situ data, as reported in the papers, is presented in Table 5.1, including the measured 10-meter wind speeds, reported release rates and the approximate location of the releases. The date, location and wind speeds were used to evaluate the methods presented in this thesis, similarly to the approach by Sherwin et. al. (2023 & 2024). For the MBMP method (See section 6.1.1) elevation data is necessary, and in this study elevation data was obtained from U.S. Geological Survey (https://ngmdb.usgs.gov/topoview/viewer/#15/32.8160/-111.7908).

Table 5.1. Overview of the test sites with ground truths used in this study. Note that the locations are approximate, and that the methane releases are controlled. For further information about the test site and method see Sherwin et. al 2023 and Sherwin et. al 2024.

Type of release	**Release rate (Kg/hour)**	**Wind speed (m/s)**	**Date / Location**	**Reference**
Test site 1	3500 kg/h	4.3 m/s	27/10/2021 [33.630637°, -114.487755°]	Sherwin et. al. 2023
Test site 2 Date 1 Date 2 Date 3 Date 4	 1100 kg/h 1200 kg/h 1600 kg/h 1500 kg/h	 2.0 m/s Not provided 2.5 m/s 1.3 m/s	 26/10/2022 08/11/2022 15/11/2022 18/11/2022 [32.8218205°, −111.7857730°]	Sherwin et. al 2024

5.3 Data for analysis

All available Sentinel-2 data overlapping a landfill site in New Orleans (~29.93 N,~90.26 W) (see Figure 5.2) from the year 2022 was used in this study. All land fill sites in the US are by law required to be monitored four times yearly, and as pointed out in Cusworth et. al (2024), the infrequent measurements can lead to missed release events and dynamics. Additionally, in-situ monitoring may not be possible on steep slopes, and even though drone or airplane monitoring is possible to carry out, regardless of terrain limitations, the operation is expensive and time consuming. Therefore, the addition of Sentinel-2-satellite estimates can be desirable, providing measurements at minimum every fifth day, under cloud free conditions.

The landfill under inspection was chosen because measurements performed by airplane in Cusworth et al. (2024), indicate release rates between 0.4 tons/hour and 10.1 tons/hour at multiple occasions in 2021 and 2022. They reported a persistent plume in all overflights, likely originating from a vent or an unlit flare, as well as larger plumes at various locations over the landfill. In this study, the location of the persistent plume, enclosed by the red circle in Figure 5.2, is referred to as location 1, whereas the rest of the landfill is referred to as location 2. An overview of the plume locations and emission rates found by Cusworth et. al

(2024) are presented in Table 5.2. As one can see from the table, most emission rates are well within the reported detection limits for Sentinel-2 (see Table 4.3). Knowing high resolution imagers had detected large plumes over the landfill, the aim of this study was to see whether it was possible to detect methane over the site using Sentinel-2 imagery.

Figure 5.2 New Orleans landfill study site. Location 1 is indicated by the red circle. Satellite image from Airbus. Source: Google Earth.

Table 5.2 Flight dates, emission rates and origin coordinates of the methane plumes detected by Cusworth et. al (2024) over the New Orleans landfill.

Location	Coordinates	Date	Emission rate (kg/hour)
1	29.931215 - 90.253519	04.06.2022	2731
2	29.935104 - 90.262639	04.06.2022	6131
1	29.931344 - 90.253389	06.05.2021	875[1]
2	29.933745 - 90.260272	06.05.2021	1344
2	29.93763 - 90.263031	06.05.2021	417
2	29.935453 - 90.262612	26.10.2021	10 151
2	29.933796 - 90.262095	26.10.2021	5978
1	29.931314 - 90.253604	26.10.2021	1366

[1] *Cusworth et. al (2024) did a methane plume detection at approximate same location 6 minutes later. The estimated emission rate was then 473 kg/hour.*

To estimate the methane release rate of a satellite observed plume, the 10-meter wind speed is needed. This is the wind speed at 10 meters height above ground and were here collected from Giovanni dataset by NASA (Global Modeling and Assimilation Office (GMAO) (2015)), which has a spatial resolution of 0.5° × 0.625°, or approximately 55.6 × 60.1 km.

6 Methods

In accordance with the range of different satellites used for methane monitoring purposes (see Table 4.1) numerous different methods to detect and quantify methane plumes have been developed. The methods can be divided into three main stages: firstly, identifying the methane plume, secondly masking it out, and thirdly estimating the respective methane mass flow rates.

The different steps are shown in Figure 6.1. For the first step, a methane enhancement image is created, which is a map showing variations of satellite derived methane concentrations over the scene. There are several different methods to obtain these maps, and in this thesis the multi band multi pass (MBMP) method by Varon et.al (2021) and a simple Beers-law method (Jia et.al 2022) are used. For both methods, areas of higher methane concentrations within the enhancement images are evaluated to determine whether they are methane plumes or falsely high methane concentration due to e.g. surface texture or composition. The following two steps (Figure 6.1) are identical for the two different methods, where the methane plume is segmented out from the background, before the emission rates are estimated following the so-called integrated mass enhancement (IME) method presented by Varon et.al (2018). In the following sections, the three stages are outlined in more detail.

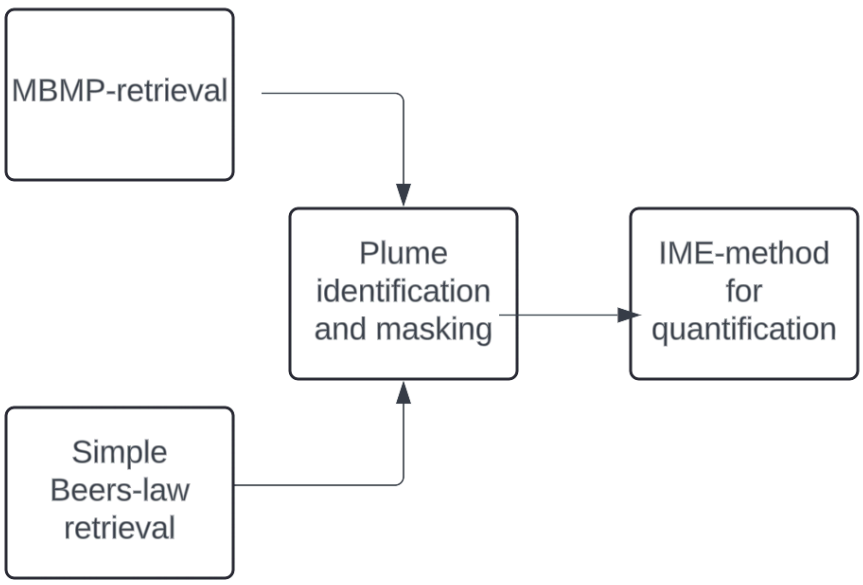

Figure 6.1. Flowchart illustrating the main steps of the methane plume detection and quantification presented in this thesis.

To illustrate the different steps of the methods, Sentinel-2 imagery obtained during the controlled test release in Ehrenberg, Arizona the 27th of October 2021 is used throughout this chapter (Sherwin et. al 2023). An optical image centered over the study site is shown in Figure 6.2. Sherwin et. al (2023) provides the approximate location of the release [33.630637°, − 114.487755°], as well as the emission rate of 3.5 tons per hour during the satellite pass. Additionally, the 10-meter wind speeds are stated to be 4.3 m/s. A Sentinel-2 image from the 17th of October 2021 is used for a methane-free comparison date. In Table 5.1 and in the following sections, this imagery, and the connected results, are referred to as Test site 1.

Figure 6.2 Airbus satellite image surrounding the point of the controlled release 27th October 2021 (Sherwin et. al 2023). Note that this image was obtained in 2024, thus the background might differ from the controlled release date. Source: Google Earth

6.1 Obtaining methane enhancement images

Two different methods are investigated in this thesis, the MBMP method by Varon et.al (2021) and a simple Beers-law method, slightly modified from Jia et.al 2022.

6.1.1 The multi band multi pass method

The multi band multi pass (MBMP) method by Varon et al. (2021) is among the most commonly used methods to create methane enhancement images for plume identification using satellite data (e.g. Zhang et. al 2022, Watine-Guiu et al 2023, Radman et.al 2023). The method was derived using both methane sensitive bands of Sentinel-2, band 11 (B11) and

band 12 (B12), however, the method is transferrable to satellites with similar bands and resolutions (Varon et.al 2021). The methane enhancement for an image is obtained by comparing it to an image of the same area without any known releases. The atmospheric methane concentrations for each of the satellite passes are obtained using the absorption properties of methane in B11 and B12, and the increase in the atmospheric concentrations are thereby assumed to be equal to the excess methane concentrations during a release. In Figure 6.3 the two bands for the emission date and the comparison date are shown.

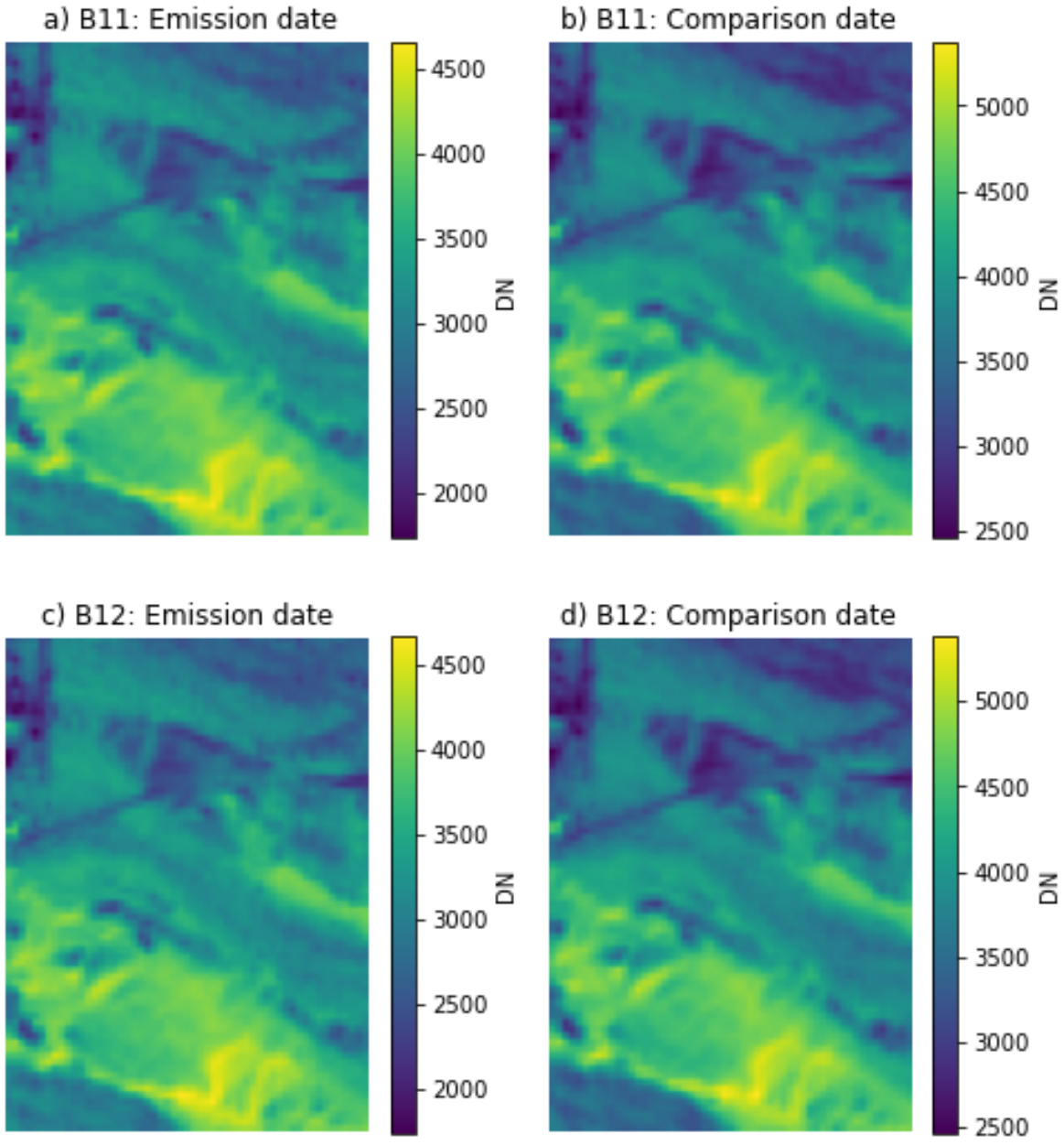

Figure 6.3 Sentinel-2 image covering an approximate area of 1.1 km x 1.5 km around the controlled release (Sherwin et. al 2023) The images on the left are from the day of the emission (27th of October 2021) and the images on the right was taken 10 days prior (17th October 2021). The two methane sensitive bands are shown in a) B11 date of emission b) B11 date of comparison c) B12 date of emission d) B12 date of comparison. The unit is digital numbers, and for S2 data the value is the reflectance multiplied by 10 000.

As shown in Figure 5.1, B12 is more methane sensitive than B11, and the MBMP method utilizes this by calculating the fractional change in reflectance (ΔR) between the two bands to extract the methane enhancements in a single image. To do this, a scaling factor c must first be obtained by performing a least square fitting of B12 to B11. Thereafter the following equation is applied:

$$\Delta R = \frac{c \cdot B_{12} - B_{11}}{B_{11}} \quad (1)$$

The derived ΔR images for the emission date at and the comparison date at test site 1 are shown in Figure 6.4.

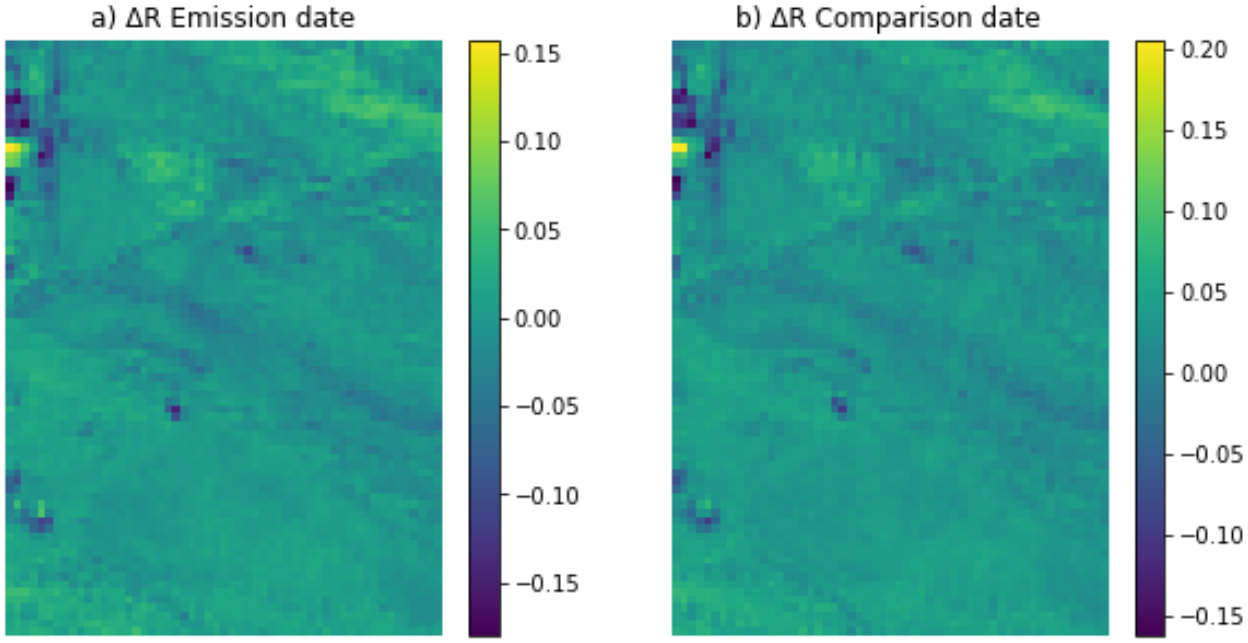

Figure 6.4 Fractional change in reflectance ΔR between B12 and B11 on date of the release (a) and date of comparison (b).

To extract the methane enhancement values from the fractional change in reflectance, they must be compared to simulated top of atmosphere (TOA) reflectance for different methane concentrations obtained with a radiative transfer model. The model used by Varon et al. (2021) takes the following form:

$$M(\Delta\Omega) = \frac{T_{12}(\Omega+\Delta\Omega) - T12(\Omega)}{T_{12}(\Omega)} - \frac{T_{11}(\Omega+\Delta\Omega) - T_{12}(\Omega)}{T_{11}(\Omega)} \quad (2)$$

where M(ΔΩ) refers to the simulated reflectance at the TOA, $T_{12}(\Omega)$ and $T_{11}(\Omega)$ refer to the simulated TOA reflectance of B12 and B11 under methane free conditions, and $T_{11}(\Omega + \Delta\Omega)$ and $T_{12}(\Omega + \Delta\Omega)$ refer to the simulated TOA reflectance for the bands given a methane

enhancement of ΔΩ. ΔΩ can then be found by minimalizing $\Delta R - M(\Delta\Omega)$, or in other words finding the methane enhancements with simulated TOA reflectance's fitting the measured data the best. Through personal communication, Dr. Daniel J. Varon at Harvard university kindly provided the python code used in Varon et. al 2021 to create the radiative transfer model and obtain the ΔΩ values, and in this thesis the script has been used for the same purposes. In Figure 6.5 the MBMP derived ΔΩ-maps for test site 1 are shown, both for the emission date and the assumed methane-free comparison date.

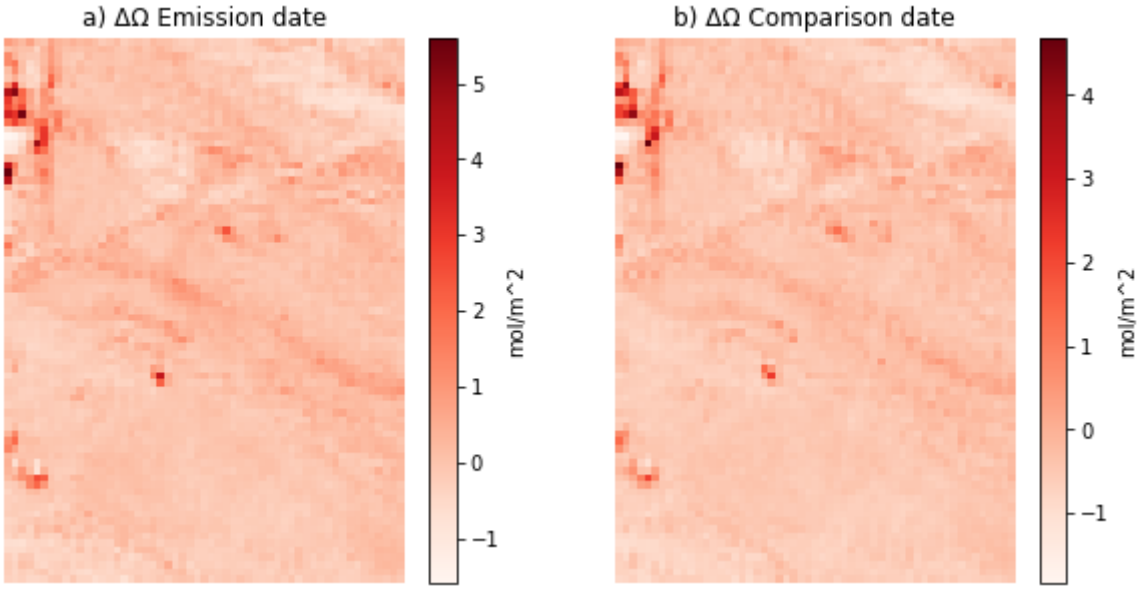

Figure 6.5. Methane enhancement images at test site 1 for the emission date (a) and comparison date (b)

As the MBMP method utilizes two images, one with and one without methane releases, ΔΩ must be calculated for each of the images. The total methane enhancement for the emission site at the date of an emission can then be found through equation 3, which is applied to reduce noise and false methane observations due to surface properties.

$$\Delta X_{CH_4} = \Delta\Omega_{\text{emission date}} - \Delta\Omega_{\text{emission free date}} \quad (3)$$

Figure 6.6 shows the methane enhancement ΔX_{CH_4} for test site 1, derived by the MBMP method. The observed methane plume is enclosed by the blue ellipse.

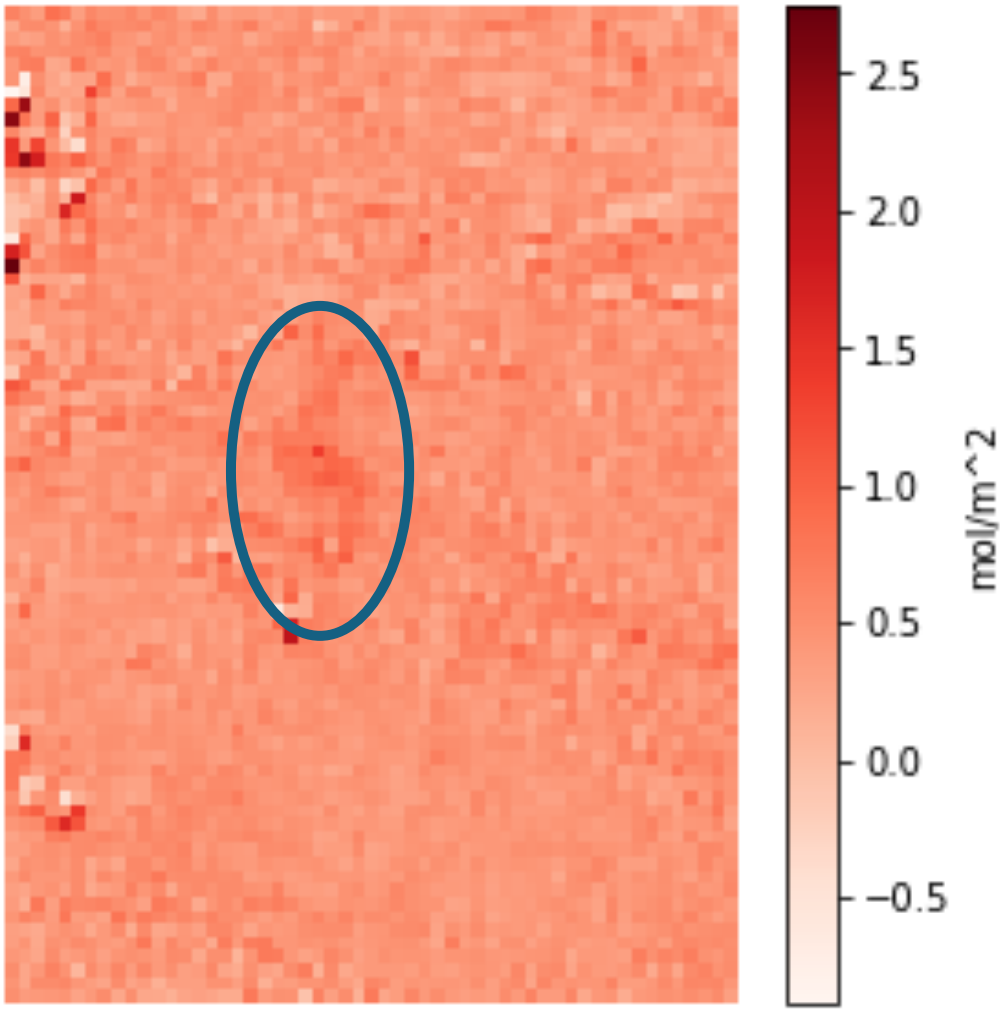

Figure 6.6 Methane enhancement map for the date of the controlled release, created using the MBMP-method. The assumed methane plume is enclosed by the blue ellipse.

6.1.2 The simple Beer-law method

Another way to generate methane enhancement images is through a simple Beer´s-law retrieval (Jia et. al 2022). The method utilizes the transmittance (T) of a methane plume, defined as the ratio between a methane sensitive band (L) and a spectrally close reference band (Lref) with no methane sensitivity. As stated by, e.g., Jia et. al (2022), Sanchez-García et. al 2022 and Gorroño et. al (2023), the relationship can mathematically be expressed as:

$$T = \frac{L}{Lref} = e^{-AMF * \sigma CH4 * \Delta\Omega} \quad (4)$$

Where AMF refers to the geometric air mass factor, taking the light travel path from the sun to the sensor into consideration. Further, σCH4 [cm^2/molecule] refers to the methane absorption cross section, which is a measure of the probability of an absorption finding place

in a methane molecule for a given wavelength. In other words, it is a measure of how strongly methane absorbs EM-radiation within the wavelengths of interest. Lastly, $\Delta\Omega$ refers to the methane enhancement, which is the quantity of interest, as it is the increase by the plume compared to the background methane (Gorroño et. al 2023).

Solving for $\Delta\Omega$, the expression becomes:

$$\Delta\Omega = \frac{-\ln\left(\frac{L}{Lref}\right)}{AMF * \sigma CH4} \quad (5)$$

The relationship presented in Eq. 5. is applicable to obtain methane enhancements using multispectral satellites, such as WorldView-3, Sentinel-2, and Landsat 8 (Sanchez-García et. al 2022, Jia et. al 2022). Where the air mass factor is calculated from the solar zenith angle, and the satellite viewing angle, defined as:

$$AMF = \frac{1}{\cos(observing\ angle)} + \frac{1}{\cos(solar\ zenith\ angle)} \quad (6)$$

In this study Eq. 5 was applied to Sentinel-2 data, where B12 is the methane sensitive band (L) and B11 is the spectrally close reference band (Lref), as suggested in Figure 5.1. The mean observing angle and the mean solar zenith angle for the scene were obtained from the satellite metadata. The methane absorption cross sections were obtained through Hitran Application Programming Interface (hapi) by Kochanov (2016) and in the calculations the absorption cross section band average for B12 was applied, see Figure 5.1. In Figure 6.7, $\Delta\Omega$ for the emission and the comparison dates are shown.

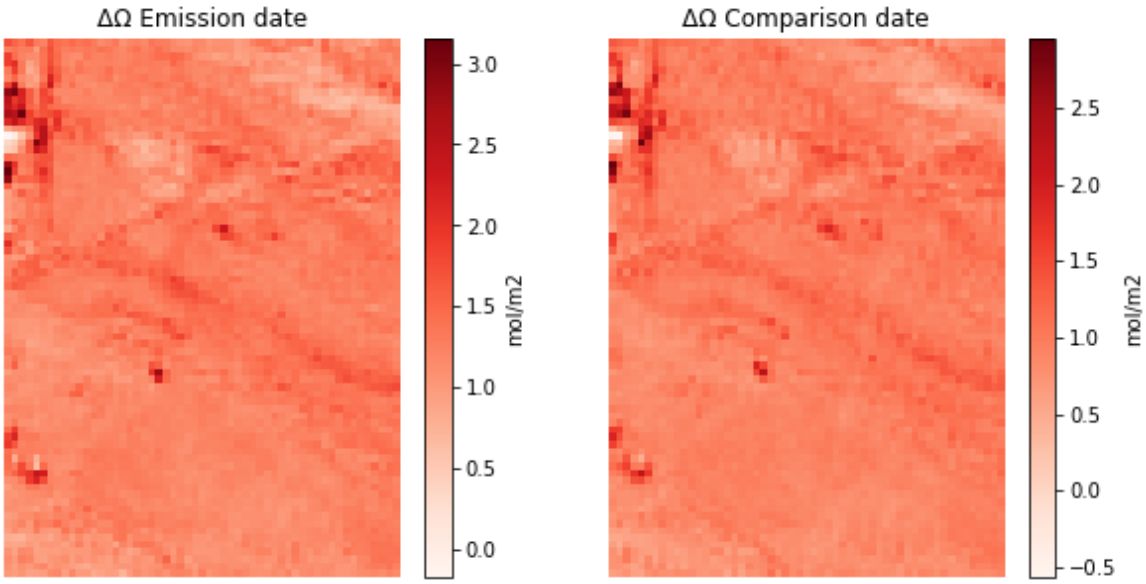

Figure 6.7 Methane enhancement for date of emission and comparison date, created using the Simple Beer's law method.

To reduce noise in the methane concentration maps a step is introduced in this thesis, where the difference between the methane enhancement on the date of observation and a presumed methane free date is derived following Eq. 3, similarly to the MBMP-method presented in section 6.1.1. Figure 6.8 shows the methane enhancement ΔX_{CH_4} after the last step. Enclosed by the blue ellipse is the methane plume detected through this method.

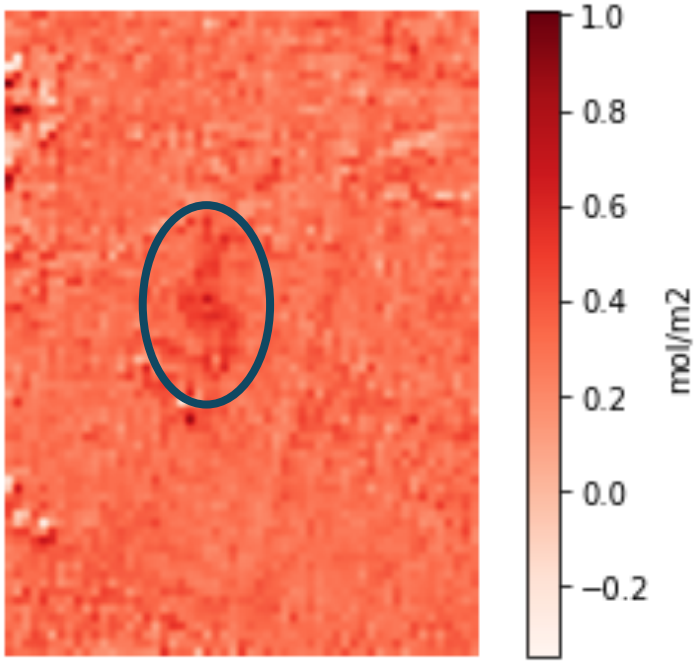

Figure 6.8 Methane enhancement difference image created using the simple Beer´s law method. The observed methane plume is enclosed by the blue ellipse.

6.2 Plume identification and plume masking

Once the methane enhancement images are created, methane plumes can be identified through visual inspection, where the characteristic shapes of methane plumes are used to distinguish releases from background noise and the appearance of falsely high methane concentrations. Methane plumes typically have soft edges, with higher concentrations towards the middle, contrary to buildings and infrastructure that typically have sharp edges and uniform reflectance. The background noise, and distinguishability of methane at a site, is dependent on background properties, where bright and uniform backgrounds give the best results (Schuit et. al 2023, Gorroño et. al 2023, Zhang 2023).

Following the method for plume identification and masking by Varon et. al (2021), a plume mask is created by applying a percentile threshold, followed by a median filter smoothening. In this thesis the threshold used varies, based on the surface background properties and the method used to create the enhancement maps. The thresholds used here are mostly determined by testing, where the aim has been to conserve the plume shape and simultaneously remove as much of the background as possible. In the example images below, a threshold of 90% is set for the MBMP-methane enhancement image (Figure 6.9a), and a threshold of 85% is set for the simple Beers law method (Figure 6.10a). After the threshold-mask is created, a smoothening 3*3 median filter is applied to remove noise (Figure 6.9b and 6.10b). Lastly, the methane plumes were, when needed, manually obtained through indexing, to discard remaining outliers.

Finally, the methane plumes and the respective concentrations given in moles/m^2 is presented in Figure 6.11 for the MBMP method and in Figure 6.12 for the Beer law's method. The masked plumes are overlayed on the same optical background image as shown in Figure 6.2.

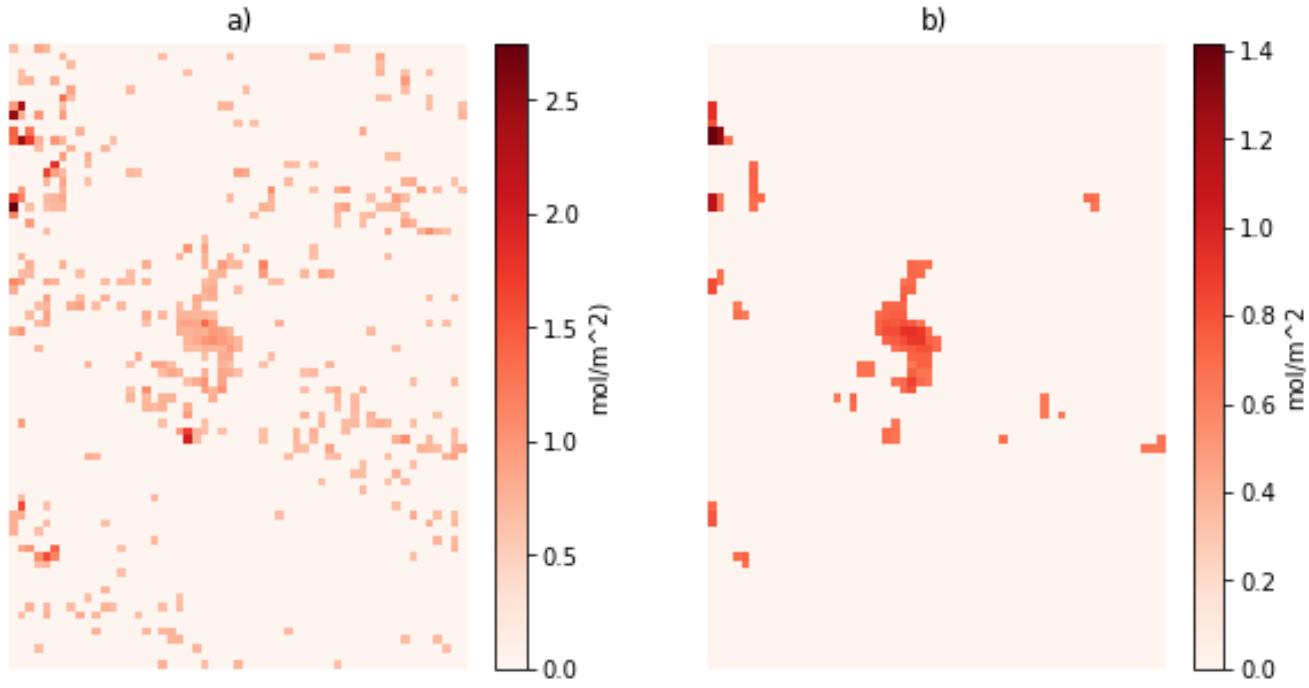

*Figure 6.9 a) Methane enhancement map after threshold at the 90 percentile. b) Methane enhancement map after threshold masking and a 3*3 median smoothening filter.*

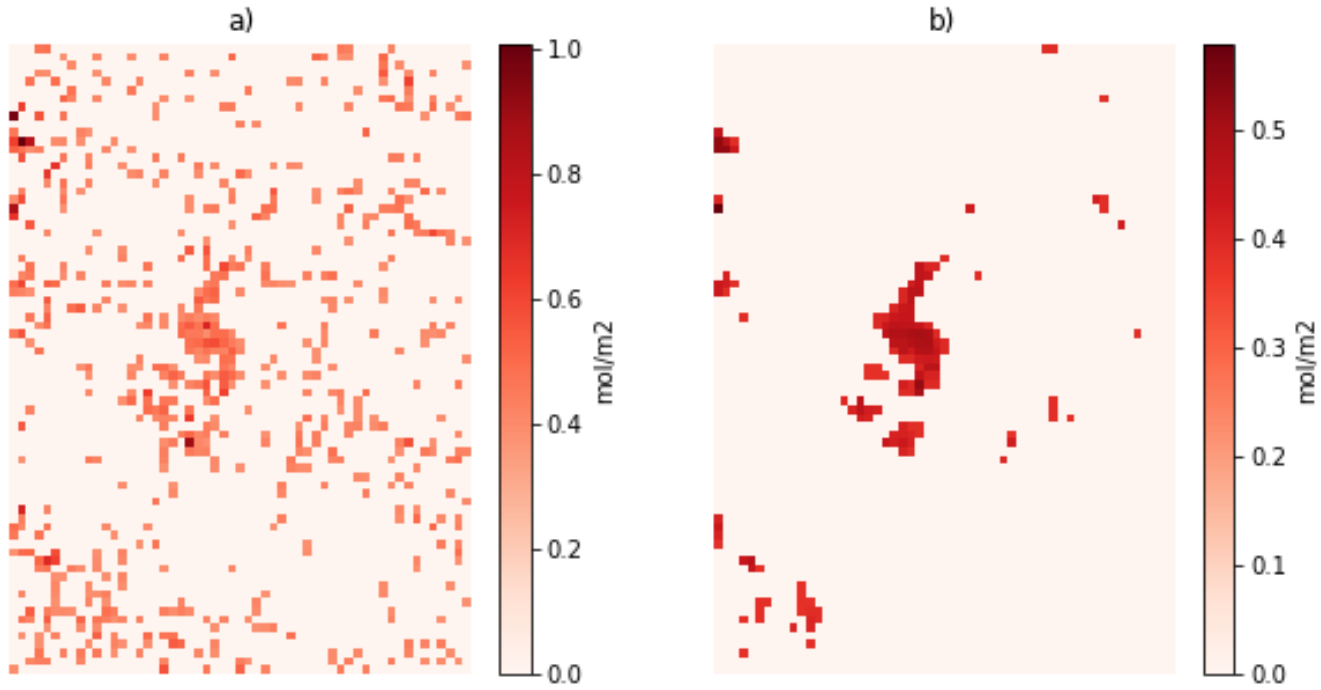

*Figure 6.10 a) Methane enhancement map after threshold at the 85 percentile. b) Methane enhancement map after threshold masking and a 3*3 median smoothening filter.*

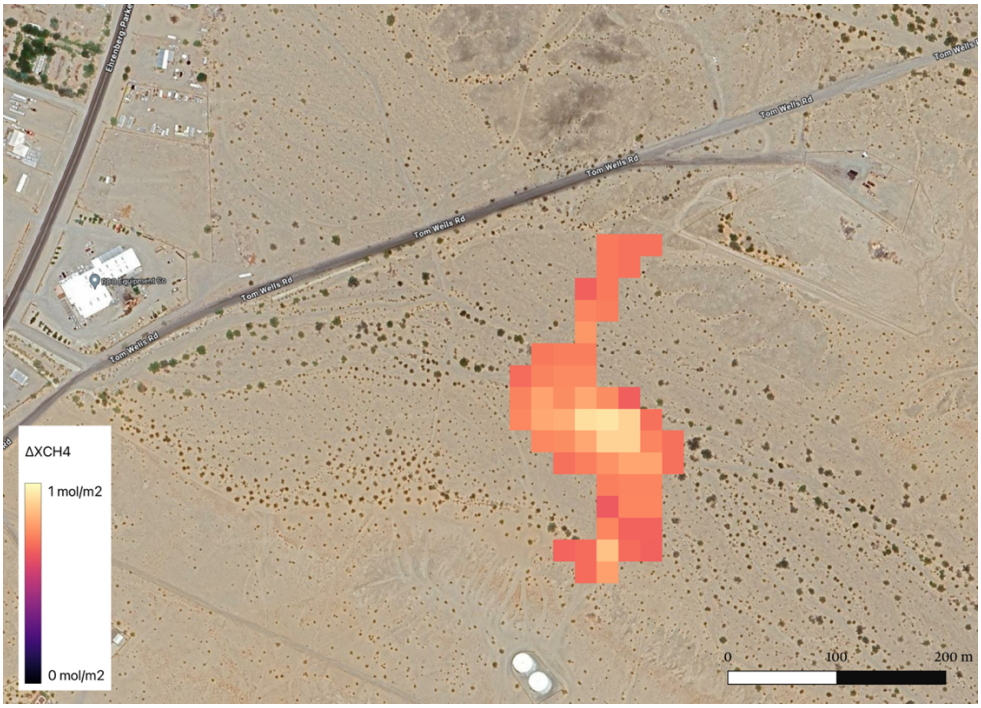

Figure 6.11. Methane plume in moles per square meter showing the location of the plume and the variations in methane concentrations across it. This methane enhancement was obtained using the MBMP method. The background image is provided by Google Earth.

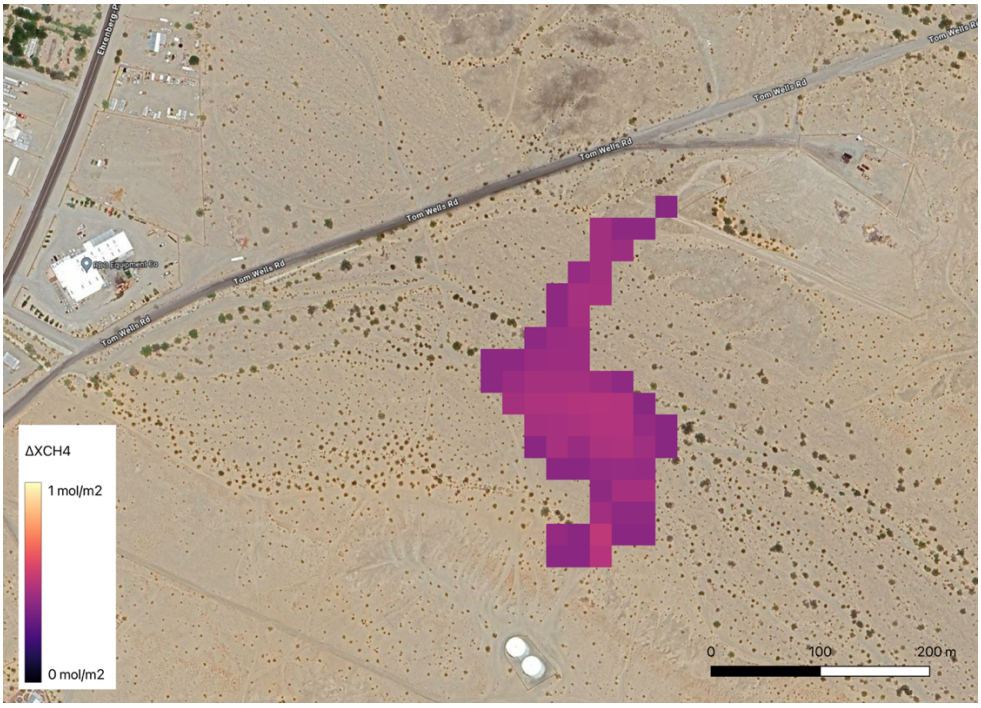

Figure 6.12. Methane plume in moles per square meter showing the location of the plume and the variations in methane concentrations across it. This methane enhancement was obtained using the plume transmittance method. The background image is provided by Google Earth.

6.3 IME-Method

Once the methane concentrations are derived, and the plumes identified, the mass flow rates must be calculated to derive the released methane volumes. The integrated mass enhancement (IME) method presented in Varon et al. (2018) is the most commonly used method for this purpose, e.g., Schuit et. al (2022), Jia et. al (2022), Varon et. al (2021) & Sanchez-García et. al (2022). The method relates the total observed mass of methane within a plume (IME) during image acquisition and the plume residence time (T), to the hourly mass of methane released from the point source, also known as the mass flow rate (Q). The relationship is defined as:

$$Q = \frac{1}{T} * IME * 3600 \quad (7)$$

The IME is the mass of excess methane in the plume, obtained directly from the plume mask (moles/m^2) by multiplying each pixel value with the molar mass of methane (0.0164kg/mol), and the pixel size (400m^2 for Sentinel-2), and finally sum up (see Eq. 8). The residence time of the plume is related to the plume length L (in meters) and an effective wind speed Ueff (in m/s), as shown in Eq. 9.

$$IME\ [kg] = \sum_{plume\ mask} \Delta\mathrm{XCH4}\ [\mathrm{mol/m2}] * 400\ [m2] * 0.0164\ [kg/mol] \quad (8)$$

$$T = \frac{L}{Ueff} \quad (9)$$

The plume length can be obtained directly from the detected methane plume, through the number of pixels in the plume mask, as well as the pixel size. As shown in equation 4 and 5, the residence time of a plume, and therefore the mass flow rate, is strongly dependent on the plume size, here materialized as the plume length. The plume length most commonly used for the IME method, is obtained by taking the square root of the total plume area, i.e. the size of the plume mask (Varon et.al 2018, Varon et.al 2021, Sanchez-García et. al 2022, Jia et.al. 2022). According to Varon et. al (2018), inclusion of plume length is essential, however the exact method used is not critical as long as there is a physical basis relating it to the plume geometry. The authors suggest an alternative approach which is using the perimeter of the mask for plume length.

Obtaining the plume length by taking the square root of the total plume area can be inaccurate for long and narrow plumes, as the value do not realistically represent the actual plume length. For example, the calculated plume length of a plume covering an area of 10 000 m^2 would be the same, both for a plume of approximate size 100m*100m and a plume of size 250m * 40 m, even though the latter is 2.5 times longer. In order to reduce the influence the shape of the plume has on the computed plume length, the methods presented in this thesis utilizes the longest axis of the plume as the plume length, see Figure 6.13.

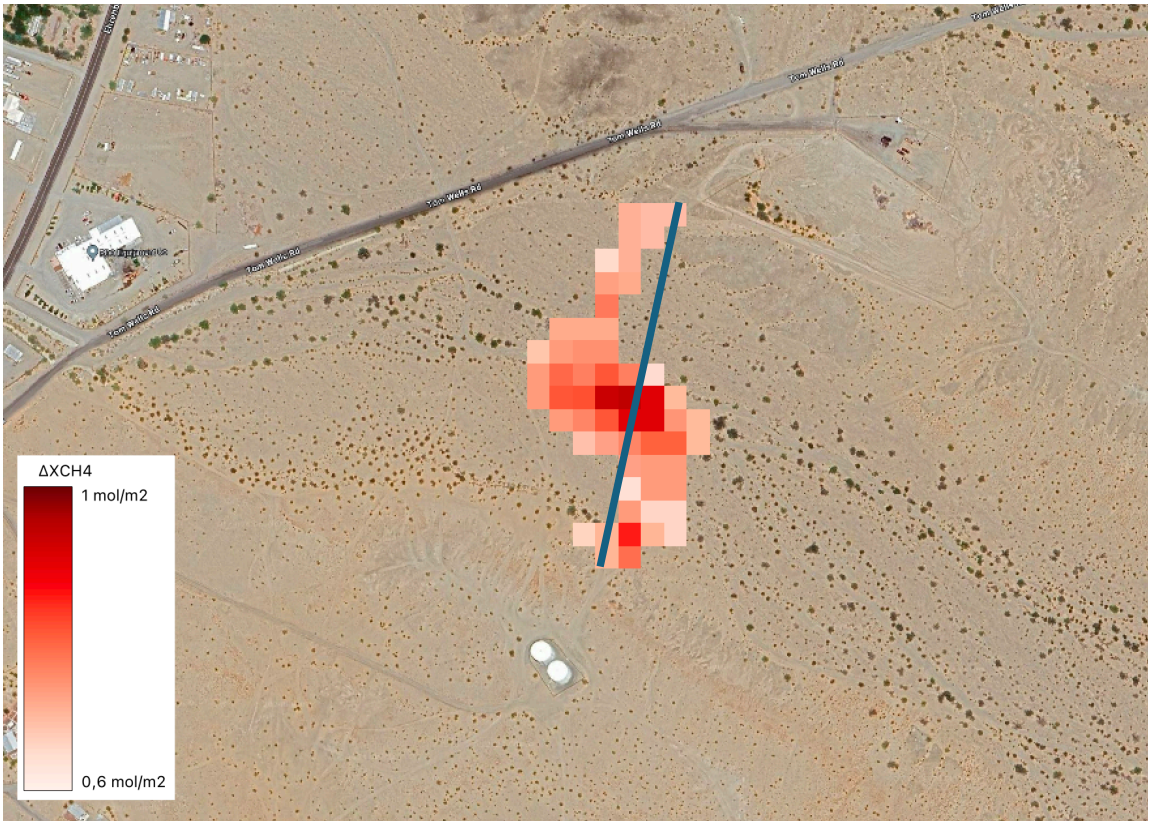

Figure 6.13. Illustration of manually obtained plume length. Background image captured by Airbus. Source: Google Earth.

The effective wind speed (in Eq. 9) refers to the wind speed which the plume is transported with. The effective wind includes three-dimensional effects and turbulence, which also need to be considered, and must therefore be calculated from the 10-meter wind speed at the site (Dogniaux 2023). The relationship between the two wind speeds may be found through large-eddy simulations and has among others been empirically determined by Varon et.al (2018), Varon et.al (2021) and Sanchez-García et. al. (2022). The empirically determined relationship varies between the different studies, and between different satellite sensors.

From what was uncovered during the literature review for this thesis, Varon et al. (2018) was the first to calculate U_{eff} for methane releases, and they found the relationship to be logarithmic, defined as:

$$U_{eff} = \alpha \cdot \log(\mathrm{U}_{10}) + 0.6\ \mathrm{m/s} \quad (10)$$

Where α range from 0.9 to 1.1, depending on instrument precision which ranges from 1%-5% percent. Figure 6.14a shows how the value of α impact the effective wind speed, and how the importance increases with increasing U10 wind speeds.

According to Varon et. al. (2021) the satellite instruments and plume masking methods must be considered in the large-eddy simulations to obtain the Ueff vs U10 relationship. For Sentinel-2 data, and the plume masking methods described previously, with a 95% threshold and a 3*3 median filter of the methane enhancement image, they empirically determined the linear relationship shown in equation 11 and plotted in Figure 6.14b.

$$Ueff = 0.33 * U10 + 0.45 \frac{m}{s} \quad (11)$$

Sanchez-García et. al (2022) performed the simulations mimicking the WorldView-3 instrument specifications and got a linear relationship for Ueff vs U10 as well, defined in Eq. 12. As one can see from Figure 6.14, the slope is shallower than what was found by Varon et. al. (2021).

$$Ueff = 0.12 * U10 + 0.38 \frac{m}{s} \quad (12)$$

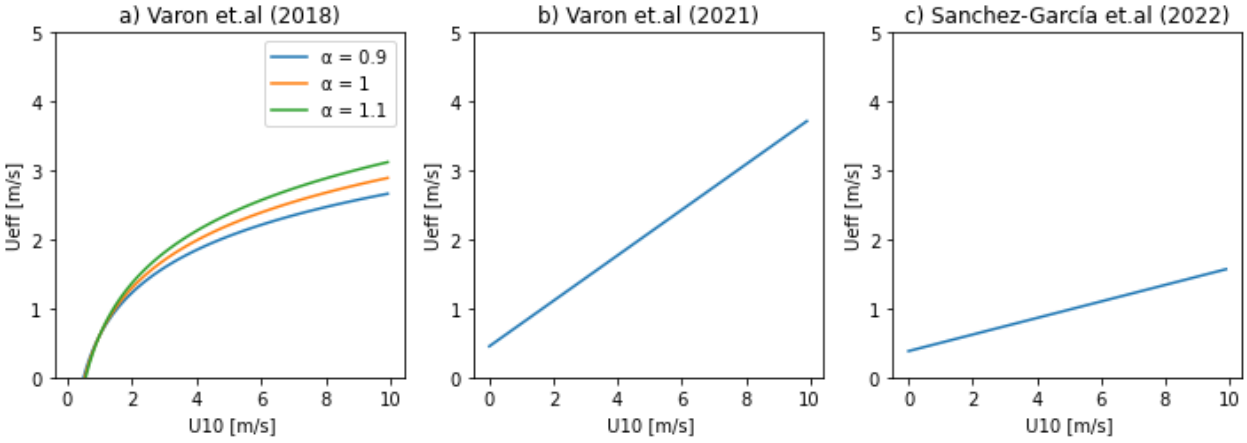

Figure 6.14 The figure shows the different relationships between U10 and Ueff by Varon et.al (2018) (a), Varon et.al (2021) (b) and Sanchez-García et.al (2022) (c) respectively, and how they vary with increasing U10 measurements.

As we can see from Eq. 5, there is a strong dependency between the mass flow rate and the wind speed and plume length. Keeping two of the three variables (Ueff, L, IME) fixed, we can in Figure 6.15 see how Q varies with the last variable. The fixed values were set to; IME = 300 kg, Ueff = 1.9 m/s and L = 300 m and were chosen because they are roughly in the middle range of the measured values of methane plumes presented in Sanchez-García et. al (2022). The mass flow rate is proportional to the effective wind speed and the IME, and inversely proportional to the plume length (Figure 6.15). This means that a doubling in either Ueff or IME will double the mass flow rate, whereas a doubling in the plume length will lead to a halving.

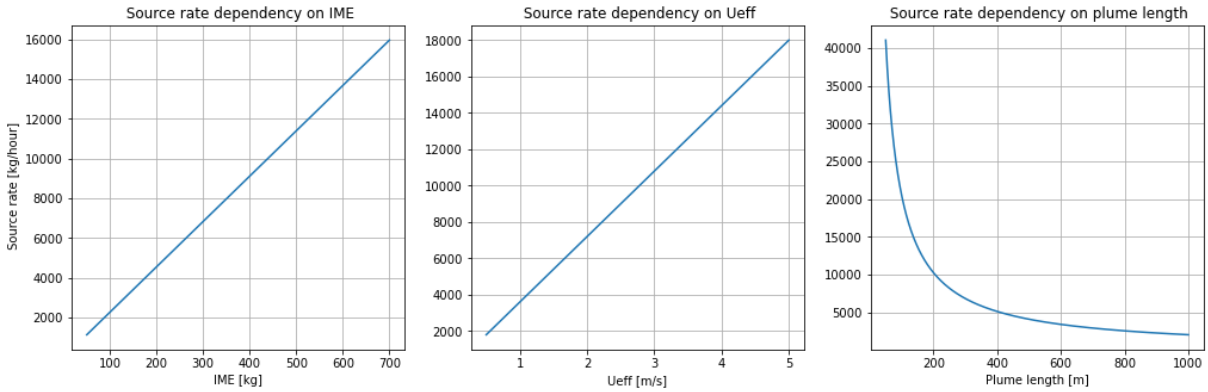

Figure 6.15 Plots showing how the source rate is dependent on respectively the mass within the frame, the effective wind speed, and the plume length.

In this thesis, the effective wind speeds are estimated as shown in Varon et al., (2021) (Eq. 7). The choice to consider this relationship was done because the satellite sensor and the method

considered during derivation of the relationship were the same as the satellite sensor and methods performed in this thesis.

By combining Eq. 7 and 9, the mass flow rate can be calculated using the following expression:

$$Q = \frac{Ueff}{L} * IME * 3600 \quad (13)$$

6.4 Test results

The two plume detection methods were tested on imagery obtained over two different locations during a total of five controlled methane releases (see Sherwin et. al 2023 and Sherwin et. al. 2024 for further information) to assess the differences between the two methods and to compare with in-situ data. The two test sites and the ground truth data are presented in Table 5.1.

6.4.1 Test site 1

The methane enhancement maps for the MBMP method and the simple Beer´s Law method is shown in Figures 6.6 and 6.8, respectively, and the corresponding masked plumes in Figures 6.11 and 6.12. As we can see from the figures, both methods produce similar shapes, however, the methane concentrations obtained with the MBMP-method is significantly higher, resulting in a higher mass flow rate estimate. In Table 6.1 the estimated mass flow rates (Q), the plume lengths (L) and the integrated mass enhancements (IME) for each of the methods are presented. For the simple Beer´s law method, the IME estimate was about 0.1 tons less, and the plume 12 m longer, resulting in a lower mass flow rate at about 3.8 tons/hour, compared to the MBMP estimate of 6.0 tons/hour. Considering the reported release rate of 3.5 tons/hour (Sherwin et. al 2023), the estimate derived using the simple Beer´s law method aligned the best with the in-situ reported release rates.

Table 6.1. The different methane enhancement retrieval methods and the derived values for IME and L, as well as the ground truth 10m-wind speed (Sherwin et al, 2023) and the mass flow rate estimates (Q) for test site 1.

Method	**IME**	**L**	**U10**	**Q**
In-situ	-	-	4.3 m/s	3.5 tons/h
MBMP	292 kg	330 m	-	6.0 tons/h
Simple Beer´s law	195 kg	342 m	-	3.8 tons/h

6.4.2 Test site 2

Figure 6.16 shows a Google Earth satellite image over the approximate location of the methane releases at test site 2. Out of the controlled releases performed in Sherwin et. al (2024), four are used to test the methods of this thesis, as they happened during Sentinel-2 satellite overpasses and had release rates within the detection limits (see section 4). The dates of the controlled releases were October 26th, November 8th, November 15^{th,} and November 18th of 2022. For comparison, November 25th the same year was used, since no releases were reported this day (Sherwin et al 2024). For three out of the four dates, the U10 wind speeds were obtained from the data appendix in Sherwin et. al. 2024, however the wind speeds for November 8th were missing, and were therefore obtained from Global Modeling and Assimilation Office (GMAO) (2015). The GMAO dataset provides the 10m meridional (north-south) and zonal (east-west) average wind speeds. The time average wind speeds from one hour prior to one hour after the satellite pass were calculated by combining the two datasets.

Figure 6.16 Satellite imagery showing test site 2. The methane is released from a point within the red rectangle. Satellite imagery from Google Earth, acquired by Airbus.

The in-situ information for the emission dates are shown in Table 6.2, together with the derived IME, L and Q for both methods.

Table 6.2. Methane enhancement retrieval methods and the derived IME, L and Q values, as well as the in situ reported wind and emission rate data. Note that the wind speeds were not reported November 8th, and the U10 this date is therefore obtained from a reanalysis product.

Date	**Method**	**IME (kg)**	**L (m)**	**U10 (m/s)**	**Q (tons/hour)**
Oct 26 2022	In-situ			2.0	1.1
	MBMP	-	-		-
	Simple Beer´s law	-	-		-
Nov 8 2022	In-situ			3.2[1]	1.2
	MBMP	23	109		1.1
	Simple Beer´s law	25	113		1.2
Nov 15 2022	In-situ			2.5	1.6
	MBMP	-	-		-
	Simple Beer´s law	-	-		-
Nov 18 2022	In-situ			1.3	1.5
	MBMP	30	209		0.6
	Simple Beer´s law	26	213		0.4

[1] *From GMAO (2015)*

For two of the dates, October 26, and November 15, no methane plumes were detected in the methane enhancements maps, see Figure 6.17. The observed apparent increases in methane concentrations in the figures were disregarded, as they were assumed to be a result of surface structures, as similar shapes appeared in all methane enhancement images of the area.

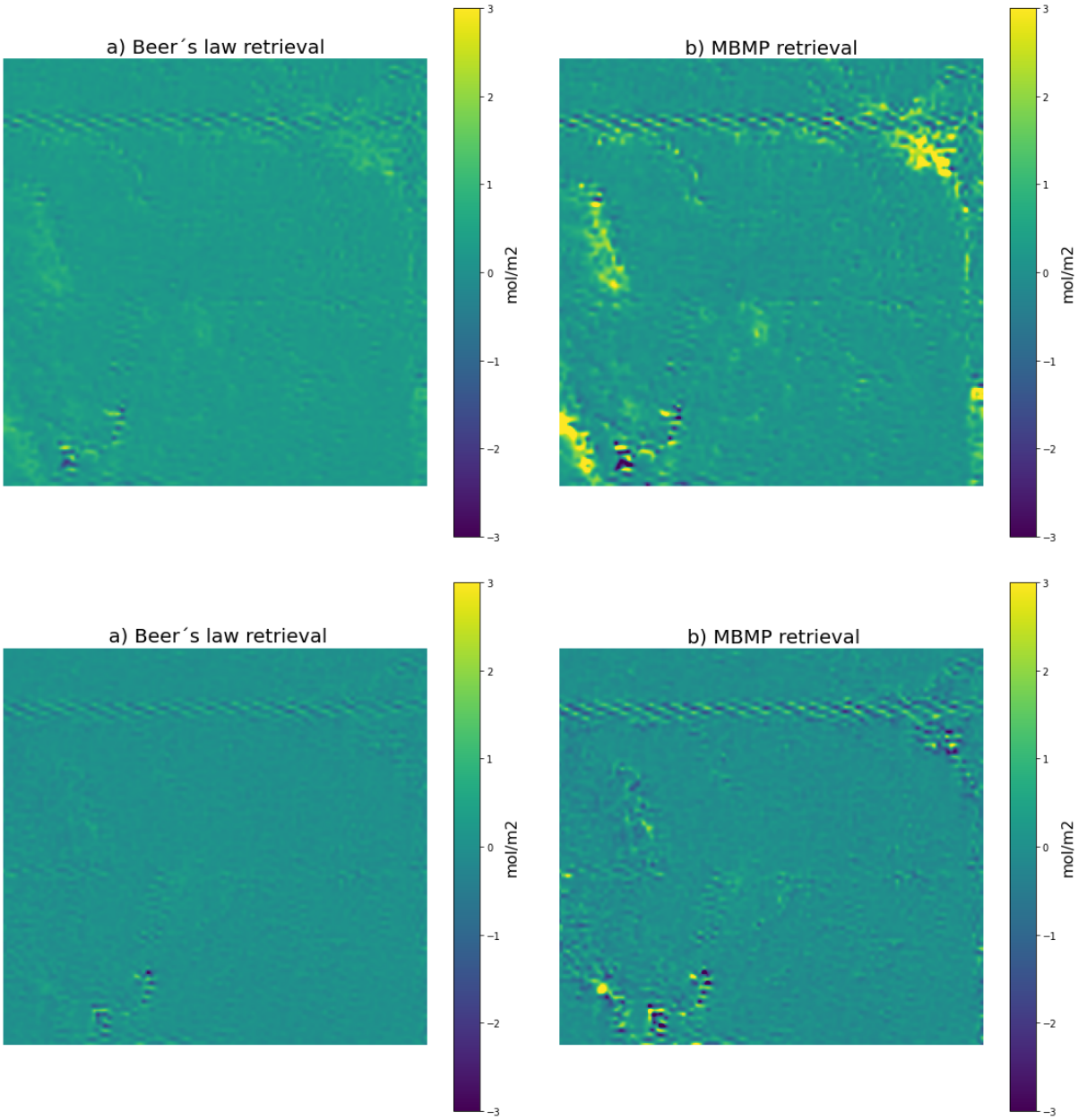

Figure 6.17 Methane enhancement maps over test site 2 the 26th October (top row) and 15th of November 2022 (bottom row), created using the simple Beer´s law method (a) and the MBMP method (b). Note that the colorbar is set to the range (-3,3) mol/m², and values outside this range might occur.

Figure 6.18 show the methane enhancement maps derived for November 8th. Using both methods presented in this chapter, a methane plume was identified, enclosed by the red circles in the ΔXCH4 maps. As one can see from the methane enhancement images in the figure several areas appear to have higher methane concentrations, however these were assumed to be a result of surface structures.

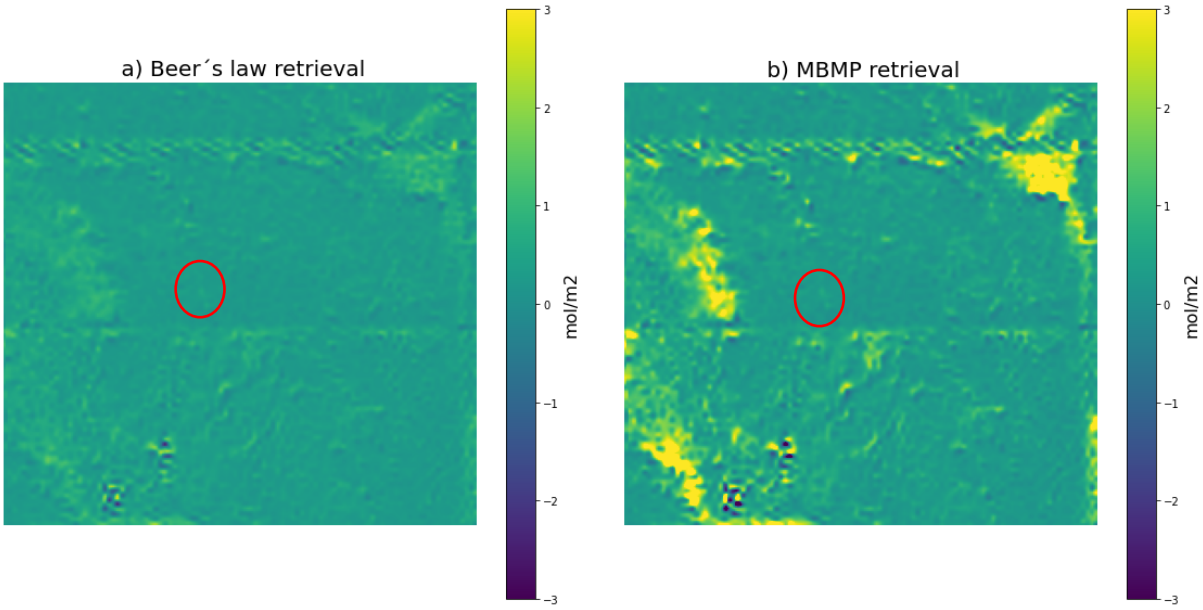

Figure 6.18 Methane enhancement maps over test site 2 the 8th of November 2022, created using the simple Beer´s law method (a) and the MBMP method (b). Note that the colorbar is set to the range (-3,3) mol/m², and values outside this range might occur.

To reduce the influence of falsely high methane concentrations, the data was cropped to a smaller area surrounding the identified plume, before a threshold mask at the 85 percentile and a smoothing 3*3 median filter were applied. The resulting masked plumes are displayed over the Google Earth satellite map in Figure 6.19a for the Beer´s law method and Figure 6.19b for the MBMP method.

a) b)

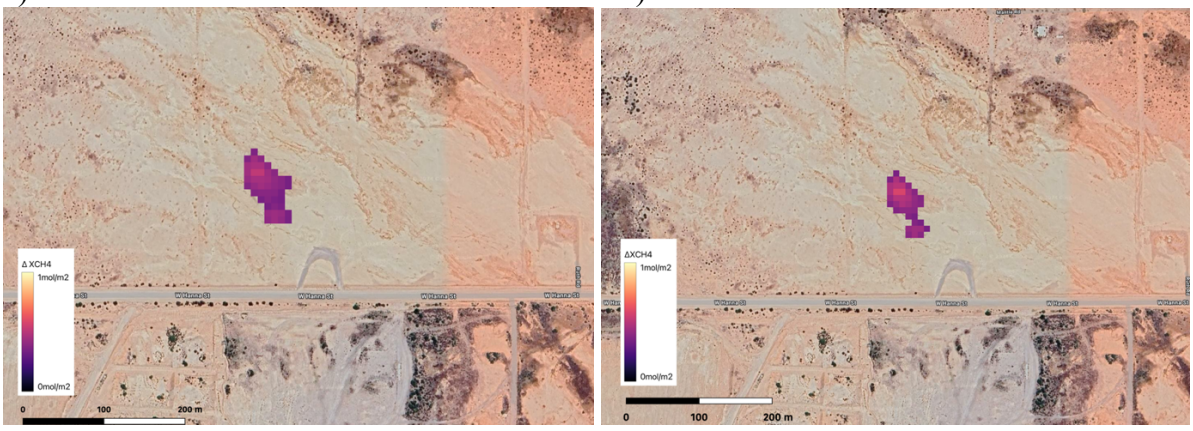

Figure 6.19 Masked plume November 8th 2022 at test site 2. Methane concentrations retrieved by a) the simple Beer's law method and b) the MBMP method. The background is Google Earth satellite imagery over the scene, acquired by Airbus.

As we can see from Figure 6.19 and Table 6.2, the two methods have very similar results for the release the 8th of November. The plume shapes are similar, however the MBMP method

gives a slightly narrower plume. The estimated mass flow rates are also very close, at 1.1 tons/hour for the MBMP retrieval, and 1.2 tons/hour for the simple Beer´s law retrieval. The ground truth data for the observed release was 1.2 tons/hour, which is close to the estimated rates by both methods, however the latter was slightly more accurate.

The last controlled release at test site 2 that was used to evaluate the methods in this study was performed the 18th of November 2022. Figure 6.20 shows the methane enhancements map created using the simple Beer´s law method (a) and the MBMP method (b). For both methods a methane plume was identified, enclosed by the red ellipses in the figure.

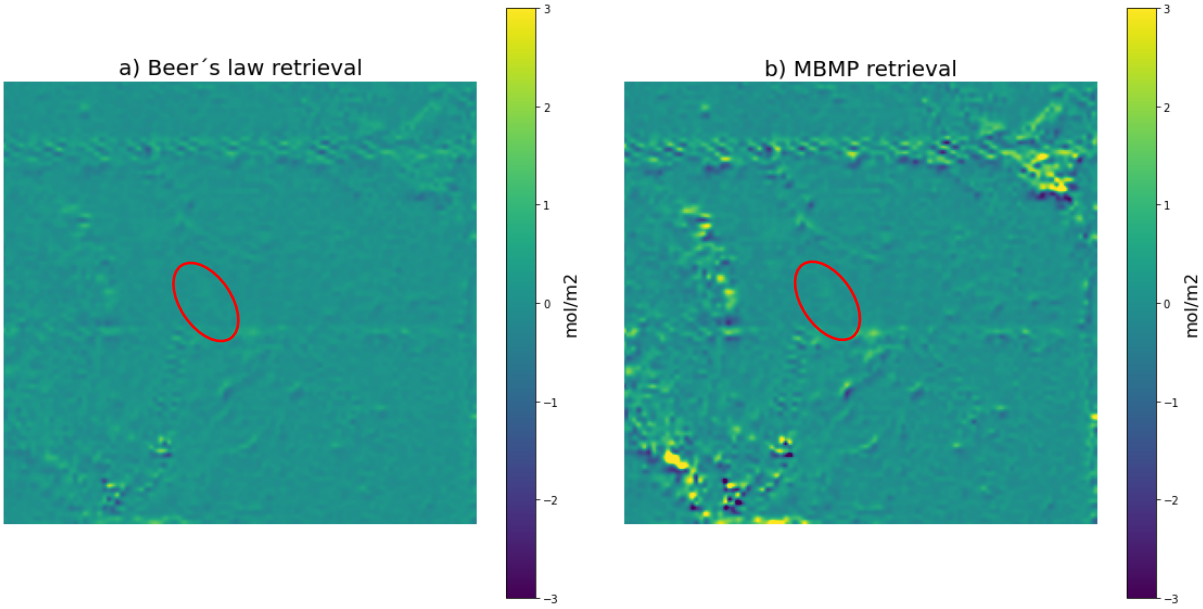

Figure 6.20 Methane enhancement maps over test site 2 the 18th of November 2022, created using the simple Beer´s law method (a) and the MBMP method (b). Note that the colorbar is set to the range (-3,3) mol/m2, and values outside this range might occur.

After the assumed methane plume was identified in each of the enhancement images, the data was cropped to a rectangle of about 450*450 m surrounding it, to reduce impact of falsely high concentrations due to surface properties. Thereafter a threshold at the 80 percentile was applied for both images, before a smoothening was performed with a 3*3 median filter. The resulting plume masks are shown in figure 6.21a for the simple Beer´s law method and 6.21b for the MBMP method.

a) b)

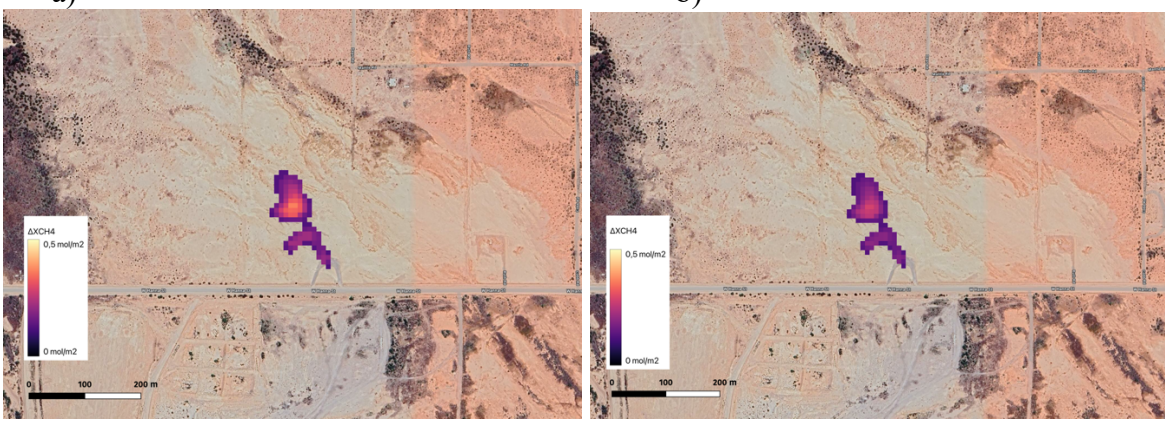

Figure 6.21 Masked methane plume from the methane enhancement image the 18th of November 2022 created with a) the simple Beer´s law method and b) the MBMP method. The plume is presented above google earth imagery acquired by Airbus

As one can see from the figures, the plume shapes and methane concentrations within the plumes are quite similar for both the methods. The estimated mass flow rate by the MBMP method this date was estimated to about 0.6 tons/hour and for the simple Beer´s law method it was 0.4 tons/hour (see Table 6.2 for specifics). The reported release rate this date was 1.5 tons/hour.

6.5 Evaluation of tested methods

For test site 1 both tested methods were able to produce methane enhancement maps with an easily distinguishable plume in the scene. The simple Beer´s law retrieval was significantly more accurate than the MBMP retrieval, with estimates 1.2 tons/hour closer to the reported release rate. In Sherwin et. al. (2023) four different teams performed retrievals over the same release, and their mass flow rate estimates were 2.3 tons/hour, 5.2 tons/hour, 5.3 tons/hour and 5.6 tons/hour. Considering the actual release rate of 3.5 tons/hour, the Simple Beer´s law method presented in this thesis is the most accurate, with 3.8 tons/hour, whereas the MBMP-method, provides the most far-off estimates. However, we were able to successfully identify the plume with both methods, and the detection accuracies are similar to the estimates in Sherwin et. al (2023).

For test site 2 there were two dates where the plumes were successfully identified, and two dates where no detections were made. In all the four controlled releases, the MBMP and the simple Beer´s law methods concluded the same in respect to whether the plumes were identified or not. All the controlled releases were in the range between 1.1 tons/hour and 1.6 tons/hour, and the one with the highest release rate was here among the non-detections. The

failure in observing the plumes for October 26th and November 15th might have to do with the direction of the plume, as the background is brighter and more homogenous north of the release location than to the southeast, thus plumes in the latter direction might be harder to distinguish. In Sherwin et. al (2024), five teams tested their methane retrieval methods over the controlled releases at test site 2. Out of the five teams, only one was able to detect the release October 26th, however, three were able to detect the release November 15th, which indicate a weakness in the methods presented here.

For the release November 8th, we detected a methane plume with a release rate of 1.1 tons/hour and 1.2 tons/hour with the MBMP and the simple Beer´s law methods, respectively. The same date the reported release rate was 1.2 tons/hour. Out of the participating teams in Sherwin et. al (2024), three were able to successfully detect the methane plume, and their release rate estimates were 3.2 tons/hour, 6.6 tons/hour and 1.1 tons/hour. For this date, the two methods in this thesis were as good as, or better than the basis of comparison. November 18th, the reported release rate was 1.5 tons/hour, and the simple Beer´s law and the MBMP-retrievals resulted in estimates of 0.4/hour and 0.6 tons/hour. The same date four out of the five participating teams in the blind test (Sherwin et. al 2024), were able to identify the plume with estimated release rates of 0.9, 0.7, 0.7, and 2.1 tons/hour. For this date, our estimations are further off the reported release rates, however, most teams have, like us, underestimated the emission rate

Even though there were difficulties identifying the methane plumes in some of the methane enhancement images, the release rate estimates for two out of the three detections agreed well with the reported values. The last date, November 18th, the methods were off by 1.1 tons/hour and 0.9 tons/hour. Even though it is a large difference, percentage wise, the release rate estimates by the participating teams in Sherwin et.al (2023 & 2024) have inaccuracies of the same scale, and greater. It was therefore decided that our estimates were sufficiently good to proceed with the presented methods.

Because of the false negative detections, and the advantage the knowledge about the release locations provided during testing of the methods, it was decided to focus on areas with assumed release rates greater than 2.0 tons/hour in the further analysis. Both the MBMP and simple Beer´s law methods had detected the same releases, and had similar estimates for the release rates, except from test site 1, where the latter was significantly more precise. A great overestimation of the MBMP for signal-to-noise ratios below 1 has also been found by others

(Rouet-Leduc 2023). Considering this, and the prolonged computation time for the MBMP-method, it was decided to continue the analysis with solely the simple Beer´s law method.

7 Results and discussion

In this thesis the study area was a New Orleans landfill, which have been monitored for a whole year (2022). This result and discussion chapter is separated into four sections, where the first section goes through the suitability of available data, the second discusses discovered challenges due to the surface properties, the third presents the results and discuss them in terms of what was expected, and lastly, the results are evaluated to determine whether they are reliable or not.

7.1 Data availability

After going through all Sentinel-2 passes over the landfill scene, 47 out of 145 images, or just above 30%, were considered suitable as they were not obscured by clouds. The number of images for each of the twelve months (controlled by the repeat cycle) where between 11 and 13, and the number of useful images ranged from 0 to 7 (see Table 7.1). In 2022, there seemed to be a trend of higher cloud density during the summer months (see Figure 7.1), however, whether this is representable for the site or not is uncertain, due to the limited amount of reviewed data.

Table 7.1 Number of Sentinel-2 images obtained over the New Orleans landfill in 2022 divided by months, and the respective number of cloud free images.

	Number of images	**Cloud free images**	**Cloud free images**
January	13	4	30.8 %
February	11	4	36.4 %
March	13	6	46.2 %
April	12	5	41.7 %
May	12	2	16.7 %
June	12	4	33.3 %
July	13	0	0.0 %
August	11	1	9.1 %
September	11	3	27.3 %
October	12	5	41.7 %
November	12	7	58.3%
December	13	6	46.2 %
Total	145	47	32.4 %

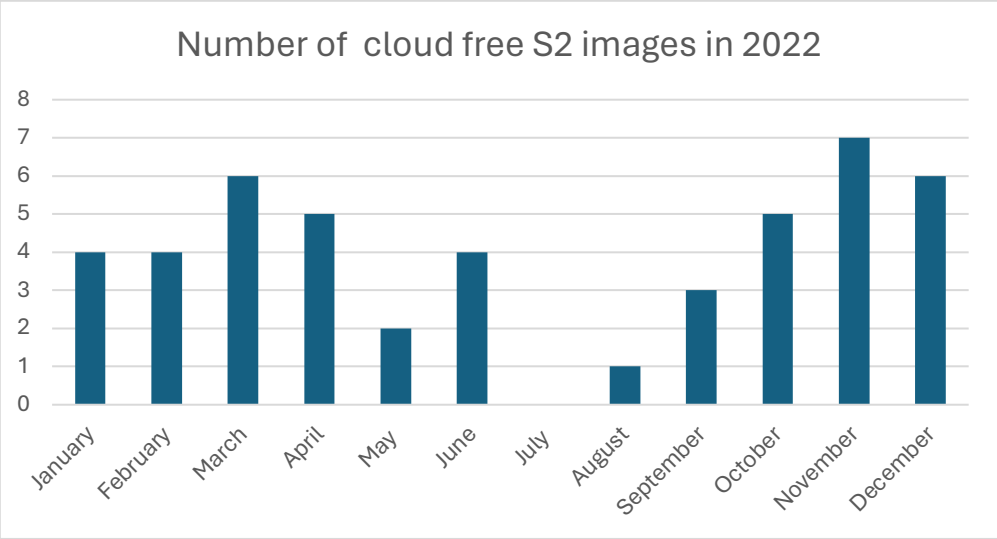

Figure 7.1 Number of cloud free satellite images over the New Orleans landfill in 2022.

7.2 Challenges with surface properties

The landfill turned out to be a challenging location for methane monitoring using the satellite data (Sentinel-2) and method (simple Beer´s law method) selected for this study. First of all, the landfill was active meaning that material was moved or disposed throughout 2022 and the area also appeared to be undergoing expansion of areal extent during the year. Therefore, there was continuous changes in the background, of varying significance.

7.2.1 Selection of reference image

The changing background of the landfill, and the effects on the associated ΔΩ-maps was a major challenge when it came to selecting proper reference images. To overcome this challenge the selected approach for this location was to choose a new suitable reference image for each date a possible plume was observed in the ΔΩ-map, instead of using the same one for all dates. In the selection process, the true color images were investigated to ensure that the background surrounding the plume remained approximately unchanged, and therefore reducing the chance of false variations in methane concentrations occurring due to surface changes in the landfill itself.

7.2.2 Identification of methane like observations

Unlike buildings and most other human infrastructures with sharp edges and easily recognizable shapes, material that is moved around or deposited at the landfill tend to appear with plume-like shapes in the ΔΩ-maps. Moreover, digging in the landfill itself may cause

methane releases, making it challenging to separate methane-like observations caused by changes in the background and actual emissions. One such example is illustrated in Figure 7.2 where the true color image and the ΔΩ image for the landfill are shown for one day in November 2022. Enclosed by the red circles in the ΔΩ images is a surface feature creating an apparent methane enhancement compared to the background, which easily could be mistaken for a methane plume without comparison with the true color images. After more thoroughly inspection, it is obvious that the observed enhancement strongly matches the observable surface feature in the true color image. Note that the example highlighted here is among one of the more extreme cases that were identified in all the data, however similar challenges occurred in a large share of the images. To ensure that methane like observations are not included, the ΔΩ-maps were investigated for obvious erroneous identifications, thus only assumed methane plumes are kept in the analysis.

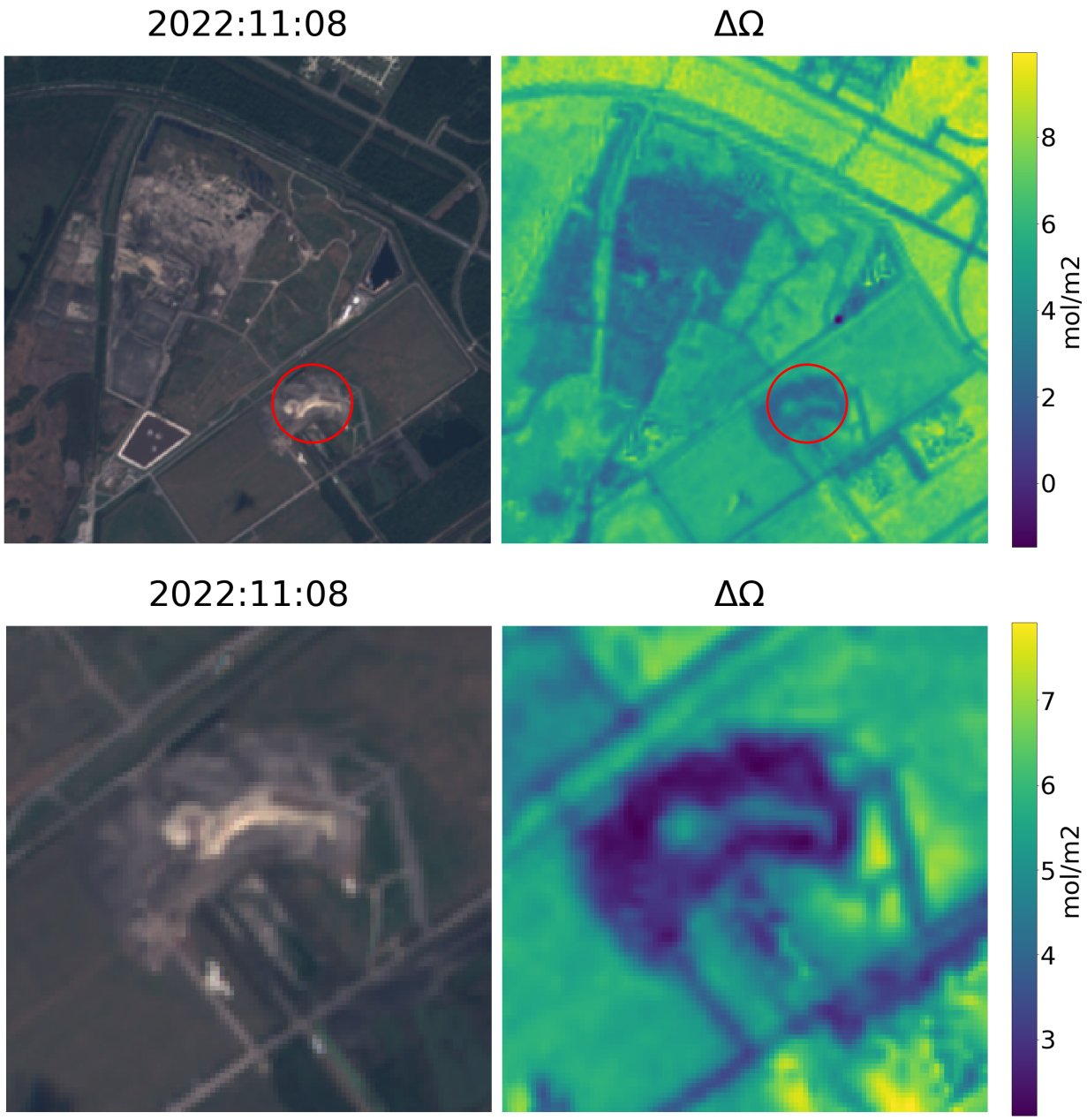

Figure 7.2 True color image (left) and ΔΩ image (right) for the whole landfill (upper row) and for a smaller section (lower row). The figure shows how surface properties of the imaged area can cause wrongly classified methane plumes, as matter on the surface occasionally have plumelike shapes, with higher apparent methane concentrations in the center which decreases with distance.

7.3 Possible methane plume detections

In this section, the detected methane plumes are presented. To account for falsely high methane concentrations, each observed possible plume was viewed with the background in mind, and apparent enhancements due to surface properties were disregarded. However, note that there is uncertainty related to whether the observed enhancements are due to methane in the atmosphere, or if it is due to surface properties that are not easily identifiable for the naked

eye considering the spatial resolution of Sentinel-2. The results are separated into the two locations mentioned section 5.3.

7.3.1 Location 1

As presented in section 5, Cusworth et. al. (2024) detected a methane plume at location 1 for all three overflights. These plumes were observed above a gas plant on the landfill, where gases from the landfill are gathered and processed for sales, and likely originated from a vent or an unlit flare (River Birch LLC n.d. & Cusworth et.al. 2024). The area is indicated with a red circle in Figure 7.3.

As presented in Table 5.2. the emission rate estimates from the aerial measurements for this point source were between approximately 0.5 tons/hour and 2.7 tons/hour. On June 4th, 2022, the reported emission rate was 2.7 tons/hour. On the same date a cloud free Sentinel-2 image was acquired approximately one hour after the plume observation, and Figure 7.3 shows the true color image and the derived ΔΩ image for this date. As one can see from the ΔΩ image, no plume is visible. This despite 2.7 tons/hour being within the assumed detection limits. There is a possibility that the releases had ceased during the hour between the airborne data collection and the satellite overpass. However, no plume was observed at this location for either of the 47 satellite passes that were investigated. Therefore, it seems more likely that the plumes originating from the gas plant are not detectable using Sentinel-2 data and the methods in this thesis. As methane detection methods by satellite generally produce the best and most accurate results over backgrounds that are homogenous and have high surface reflectance, a likely explanation is that the nonuniform background with buildings and water surrounding the emission source, see Figure 7.4, creates too challenging conditions for the method. Perhaps, scattered fractions of the plume enhancement appear in the ΔΩ image, however they are not visible and do not form a plume-like shape. This indicates that the methane concentrations are not high enough to be detected considering the background properties, hence the spectral and/or spatial resolutions of the data is too low.

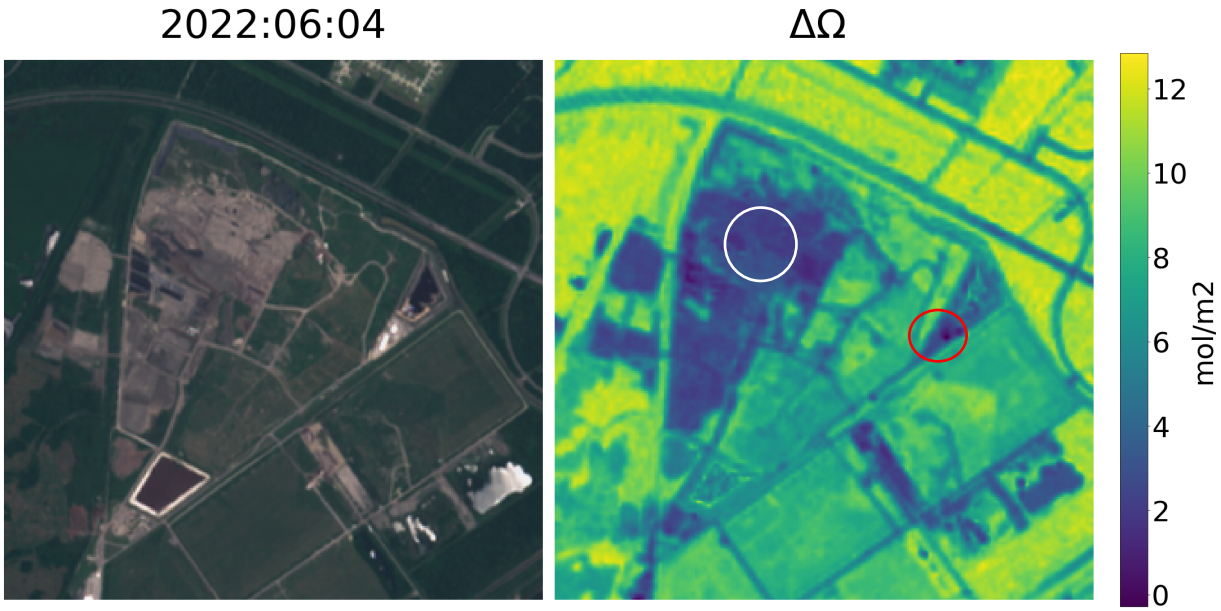

Figure 7.3 True color image (left) and ΔΩ (right) for June 4th 2022. Enclosed by the red circle is the release area of the persistent plume observed by Cusworth et. al. (2024) and enclosed by the white circle is the origin of a larger plume observed during the same overflight.

Figure 7.4 Satellite map section covering the gas plant and location 1, where plumes were observed persistently by Cusworth et. al (2024). Source: Airbus image obtained from Google Earth.

7.3.2 Location 2

For the rest of the landfill, which here is referred to as location 2, a total of 8 possible methane plumes were identified in the year of 2022. In Table 7.2 the mass flow rate estimates are presented, together with the integrated mass enhancement (IME), the 10-meter wind speed

(U10) and the plume length (L). The estimated release rates are in the range between 1.4 tons/hour and 13.6 tons/hour, which seems reasonable, considering the emission rate estimates by Cusworth et. al (2024) were between 0.4 tons/hour and 10.1 tons/hour, and the detection limitations for Sentinel-2.

Note that the second methane plume found by Cusworth et. al (2024) on June 4th 2022, with origin within the area of the white circle in Figure 7.3, was not detected in this study. Despite an estimated mass flow rate of 6.1 tons/hour (Cusworth et. al 2024), and the short time between the overflights.

Figures 7.5 - 7.11 show the masked plumes for each of the eight detections with the Google Earth satellite map in the background. Be aware that the Google Earth map is created from different images captured between 2019 and 2024, and the background is therefore not entirely accurate for how it looked during the satellite passes used for this analysis. In addition, the range of the legend varies among the images, to enhance the concentration changes within each plume.

Table 7.2. Mass flow rate estimates for possible methane plumes observed over the New Orleans landfill, including derivations of necessary parameters for the calculation.

Date	Mass flow rate (tons/hour)	IME (kg)	U10 (m/s)	L (m)
01.03.2022[1]	7.8	115	11.0	214
01.03.2022[2]	12.5	63	11.0	75
07.04.2022	9.0	178	7.7	212
25.04.2022	1.4	31	3.8	140
27.04.2022	13.6	758	2.8	274
14.09.2022	8.3	116	4.0	89
03.11.2022	5.2	141	3.3	148
18.12.2022	4.8	106	5.3	175

[1] First possible methane plume observed March 1st, 2022. [2]Second possible methane plume observed March 1st, 2022.

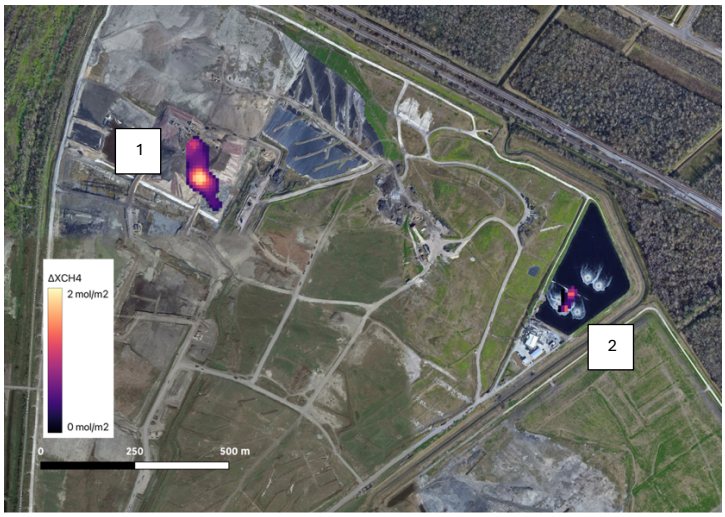

Figure 7.5 Possible methane plumes March 1st 2022. Number 1 refers to the first observed plume, and 2 to the second (see Table 7.2). The background image is provided by Google Earth.

Figure 7.6 Possible methane plume April 7th, 2022. The background image is provided by Google Earth.

Figure 7.7 Possible methane plume April 25th 2022. The background image is provided by Google Earth.

Figure 7.8 Possible methane plume April 27th, 2022. The background image is provided by Google Earth.

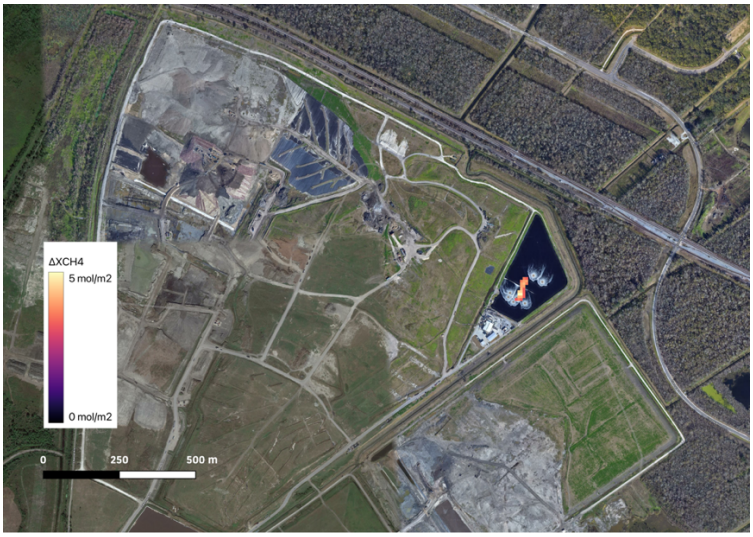

Figure 7.9 Possible methane plume September 14th, 2022. The background image is provided by Google Earth.

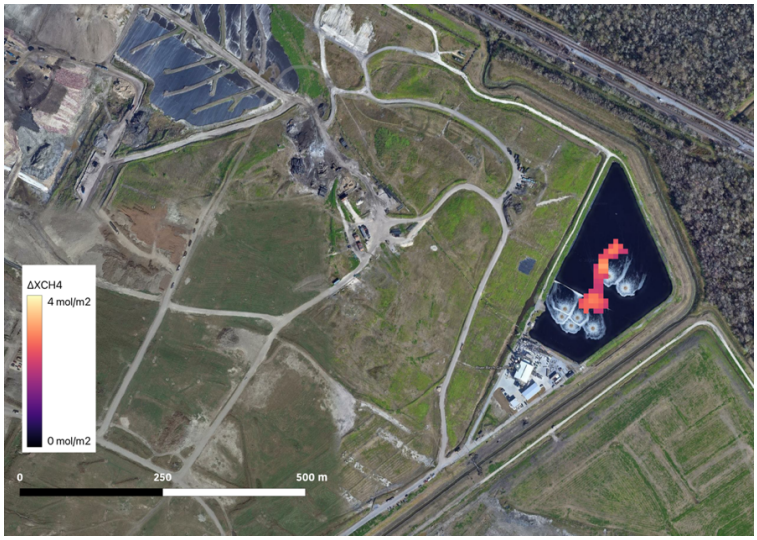

Figure 7.10 Possible methane plume November 3rd, 2022. Note that the background is cropped more than the other images in this section. The background image is provided by Google Earth.

Figure 7.11 Possible methane plume December 18th, 2022. The background image is provided by Google Earth.

7.4 Evaluation of possible methane plume detections

As one can see from Figures 7.5 – 7.11, the masked detections appear plume-like, with elongated shapes and higher concentrations towards the center. However, as explained in section 7.1 there are great uncertainties related to whether the detections are true or false positives. Therefore, a review of the detected plumes, with respect to the wind direction and the surface elements, is carried out in this section.

7.4.1 Analysis of coherence between plumes and wind estimates

In Table 7.3 the average wind intensities in the eastward and the northward direction are presented for the two hours surrounding the satellite pass for each of the detection dates. It is

expected that a methane plume would be parallel to the wind direction, as the moving air masses would take the methane with them. For the first detection date, March 1st, the estimated wind direction was approximately southwest. As one can see from Figure 7.5 the second plume (2) aligns well with the estimated wind, however, the first one (1) deviate somewhat. For April 7th, the wind direction was estimated to be southeast, with a shift towards east. The longest axis of the observed plume on this date (see Figure 7.6) is shifted compared to the estimated wind direction, as it is along the north-south axis. For April 25th the estimated wind direction was northwest, which aligns well with the long side of the plume (see Figure 7.7). April 27th the detected plume is aligned along the north-south axis (see Figure 7.8), whereas the assumed wind was towards southwest. For September 14th, the wind was estimated toward southwest. This date the longest axis of the plume is closer to the north-south direction (See Figure 7.9) than what one would expect with the estimated winds. Additionally, the concentrations seem to decrease towards north, which would align better with northwards winds. November 3rd, the estimated wind direction was to the southwest. The same date, the detected plume was along the north-south axis once again (See Figure 7.10). Lastly, the estimated wind direction for December 18th was towards southwest. The same date, the direction of the detected plume does not relate to the wind direction (see Figure 7.11).

For high wind speeds one would assume that the released methane would be transported faster with the moving air masses, thus the detected concentrations should decrease with increasing wind speeds. This relation is partly found in these results, as the highest concentrations (between ca. 3-5 mol/m^2) are found for April 27th and September 14th which had among the lowest wind speeds. The lowest concentrations (ca. 0-0.8 mol/m^2), on the other hand, were found April 25th, when the wind speeds were 3.8 m/s, which also is among the three dates with the least wind. The three next dates with the lowest concentrations were found March 1st, April 7th and December 18th, with plume concentrations between 0.5-2 mol/m^2, thus agreeing well with the fact that these were the dates with the highest wind speeds. However, the variation in wind speeds between these three dates are 5.3 – 11.0 m/s, and there are no obvious differences in methane concentrations, even though there is a great difference in concentrations between e.g. September 14th and December 18th with wind speeds 1.3 m/s apart. Therefore, we cannot conclude to see any obvious coherences between detected concentrations and wind speeds. It should, however, be mentioned that the differences in

concentrations also could be attributed to variation in actual emission rates between the emission sources and dates.

Table 7.3 Eastwards and Northwards wind speeds obtained from Giovanni (GMAO 2015) for the plume observation dates. Positive values refer to wind speeds towards east and north, respectively, whereas negative values indicate wind speeds towards west and south.

Date	Eastward U10 (m/s)	Northward U10 (m/s)	Wind speed (m/s)
01.03.2022	-7.5	-8.0	11.0
07.04.2022	6.6	- 4.0	7.7
25.04.2022	-2.5	2.9	3.8
27.04.2022	- 1.9	- 2.0	2.8
14.09.2022	-3.3	-2.2	4.0
03.11.2022	-2.9	-1.5	3.3
18.12.2022	-3.0	- 4.4	5.3

To summarize, the detected methane plumes do not match the wind direction estimates very well, as one would expect the longest axis of the plume to align with the wind direction. Additionally, as far as what was observed during this study, there does not seem to be any relation between the magnitude of the wind speed and the concentrations of the plume, even though one would expect higher wind speeds to dissolve the plume faster and therefore lead to lower overall concentration in the image. Considering the low coherence between wind data and the properties of the detected plumes, the wind does not support the probability of the observed plumes being true positive detections. Only two out of the eight plumes are aligned along the estimated wind direction, and no clear relation between wind speed and plume shapes and concentrations were found. However, the wind data that is used in the analysis is obtained from a dataset with spatial resolutions that are much lower than the area of the observation site (55.6 × 60.1 km.). The local wind directions and intensities that would have been measured in-situ might therefore be very different from what is presented in Tables 7.2 and 7.3.

7.4.2 Plume shapes versus true color images

Even though the selection of possible methane plumes was strict regarding whether the observed enhancements were a result of background features, there are some similarities that can be observed for some of the plumes. This section goes through each of the plumes ΔΩ images (enclosed by the red circles) and compare them to the true color image of the same satellite pass. The masked plumes are shown above in Figures 7.5 - 7.11.

For March 1st, the true color image and the methane enhancement map are shown in Figure 7.12. For plume 1, the background true color image and the ΔΩ image have little in common at first glance. However, when inspecting the images further, there are some similarities present. The sharp "arc" that the possible plume enhancement appears to have, can remind of the shape of the dark brown area in the true color image (enclosed by the blue circle in the figure). However, the shapes do not appear identical. For plume 2, we were not able to relate the enhancements to ground items with the same shape, but the detection is over water, which is a challenging background, and will be discussed further in section 7.4.3.

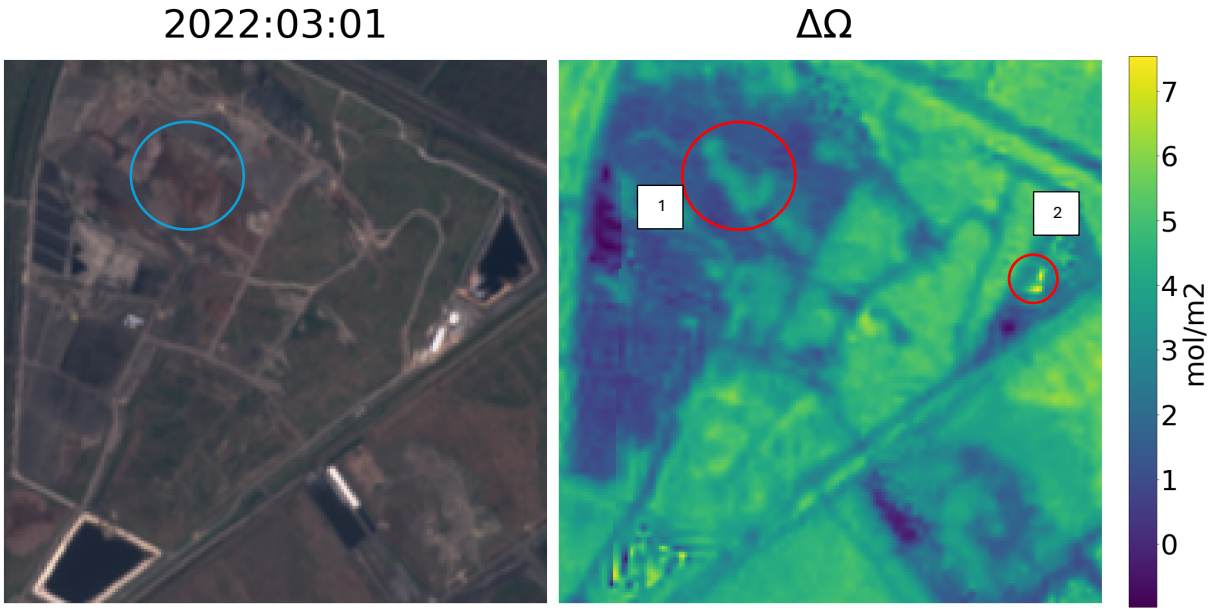

Figure 7.12 True color image of the landfill March 1st, 2022, together with the derived ΔΩ image. Enclosed by the red circles are the plumes that were detected this date. Enclosed by the blue circle is the area of plume 1 in the true color image.

For April 7th, the methane enhancement and true color images are shown in Figure 7.13. The possible plume enhancement (enclosed by the red circle in the ΔΩ image) have obvious similarities with the background at the same location (enclosed by the blue circle). Both the detected plume and a lighter surface element are narrow in the north-end and widens towards the south. The shapes are, however, not identical, as the detected plume appears to be slightly shifted counterclockwise compared to the true color ground element. Additionally, the detected plume appears longer, and this is enhanced after the plume is masked (see Figure 7.6).

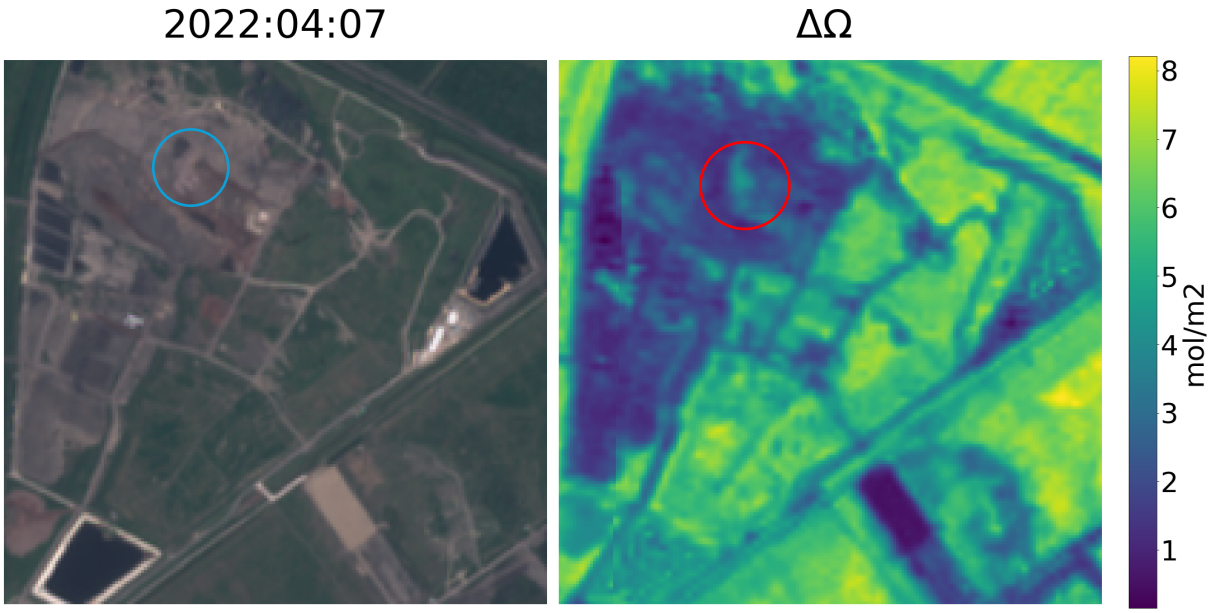

Figure 7.13. True color image of the landfill April 7th, 2022, together with the derived ΔΩ image. Enclosed by the red circle is the plume that was detected on this date. The blue circle (left) indicate possible plume area of the True Color image.

For the possible methane plume detection April 25th, we were not able to relate the shape of the plume to any visible background elements in the true color image (see Figure 7.14)

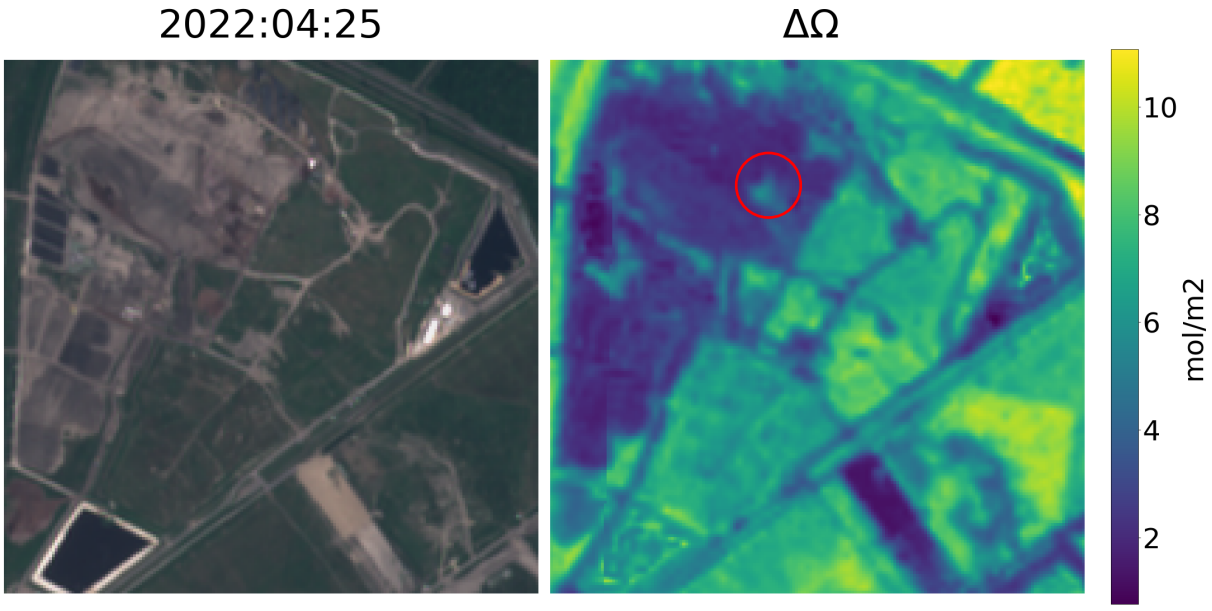

Figure 7.14 True color image of the landfill April 25th, 2022, together with the derived ΔΩ image. Enclosed by the red circle is the plume that was detected on this date.

In Figure 7.15 the true color image and the derived ΔΩ image for April 27th is presented. The possible methane plume is enclosed by the red circle. At first glance, the plume does not seem to resemble any surface items. However, after more thorough inspections, some similarities are present. As one can see from the figure, the north-end of the plume has an almost right-

angled outline, which also is visible in the true color image. In the figure the referred area is marked with yellow arrows in both images. Even though there is a clear coherence between the plume shape in the north-end and the background items, the rest of the plume shape is not easily distinguishable from the true color image.

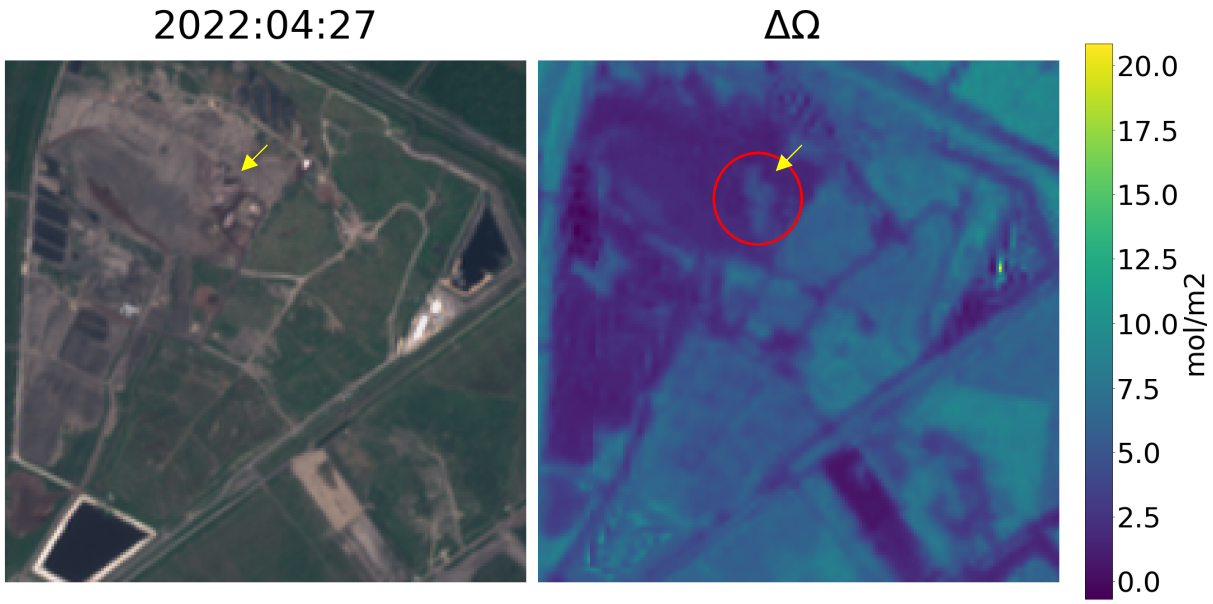

Figure 7.15 True color image of the landfill April 27th, 2022, together with the derived ΔΩ image. Enclosed by the red circle is the plume that was detected on this date.

For September 14th and November 3rd, no similarities between the shapes of the detected plumes and the background were identified (see Figure 7.16). The plumes are shown enclosed by the red circles in the ΔΩ images, and for both dates the plume is detected over water, and the challenges with detection over water will be elaborated further in section 7.4.3, as mentioned previously.

Lastly, the ΔΩ image is presented together with the true color image for December 12th in Figure 7.17. The detected plume (enclosed by the red circle) appears to resemble parts of a light grey feature in the background (enclosed by the blue circle). The plume has an elongated shape and is tilted at angle of about 30 degrees from the north-south axis. Parts of the surface feature have the same orientation and similar shape; hence the detected plume might be a result of the surface composition. The feature in question is highlighted in Figure 7.17 by the parallel, orange, line segment right next to it.

However, the light-grey surface feature is larger than the plume detection, and assuming the substrate within the whole feature is the same, one would expect a different plume shape. To

investigate this further, the true color and ΔΩ image for December 23rd was inspected (see Figure 7.18). As one can see from this figure, the light grey feature in the true color image is almost unchanged from December 18th, yet there are no obvious enhancements with similar plume-like shapes in the same location of the ΔΩ. Because the shape of the plume is not definitely the same as the surface feature, even though there are some similarities, and because the plume disappears even though the background remains approximately the same for the following satellite pass, it seems reasonable that the plume might be due to atmospheric methane.

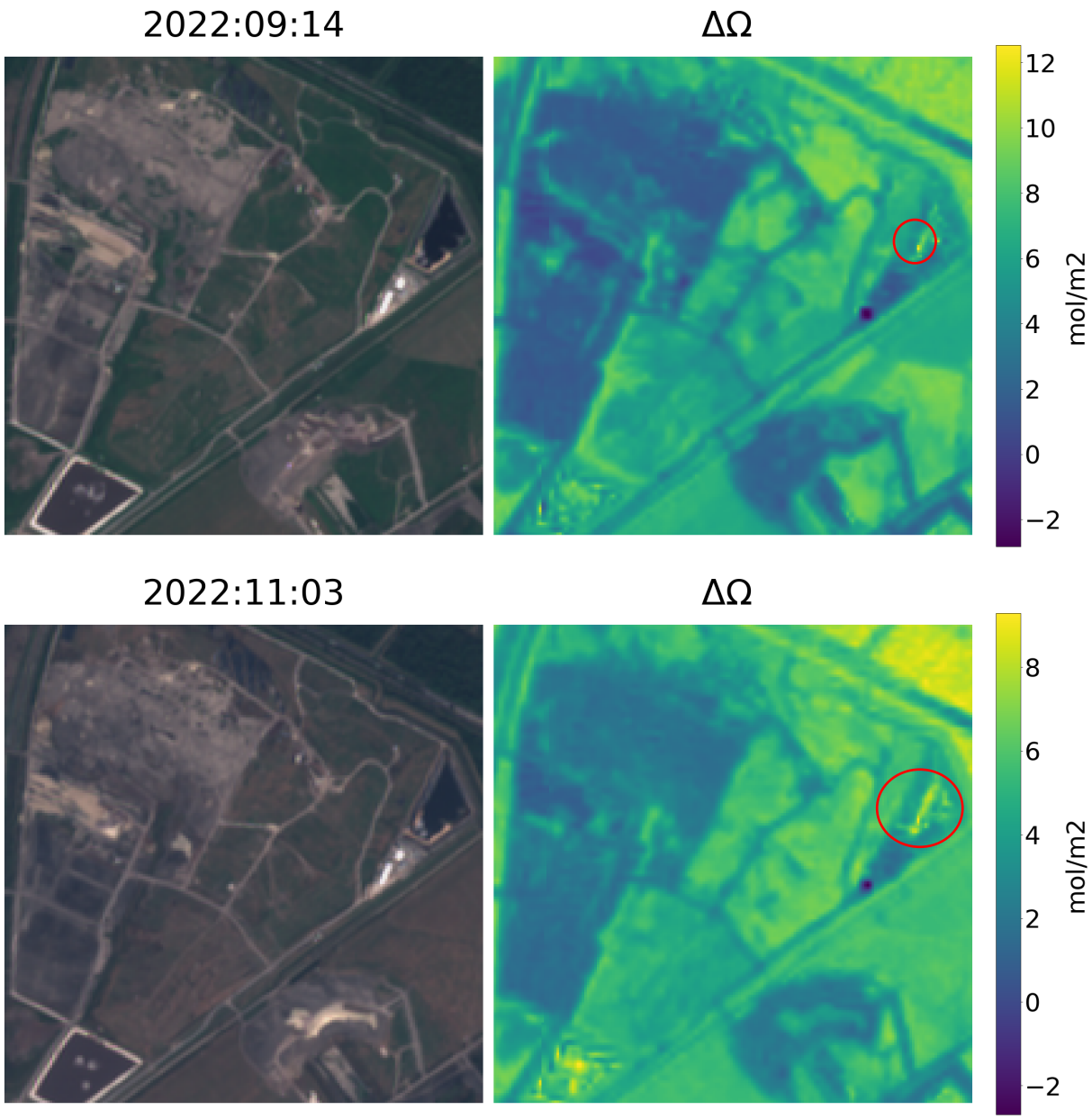

Figure 7.16. True color image (left) and derived ΔΩ image (right) for September 14th (upper row) and November 3rd (lower row). Enclosed by the red circles are the plume detections for the respective dates. Note that the range of the legend differs.

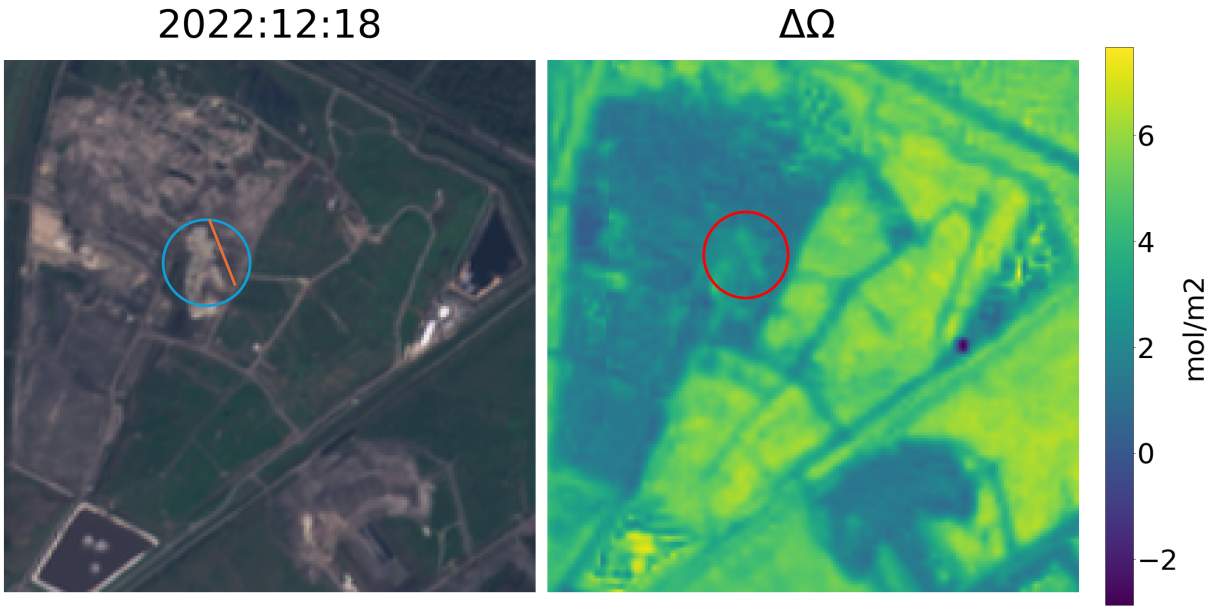

Figure 7.17. True color image and derived ΔΩ image for December 12th. Enclosed by the red circle is the possible methane plume detected in the ΔΩimage. The orange line is placed next to and parallel to a surface feature that resemble the detected plume.

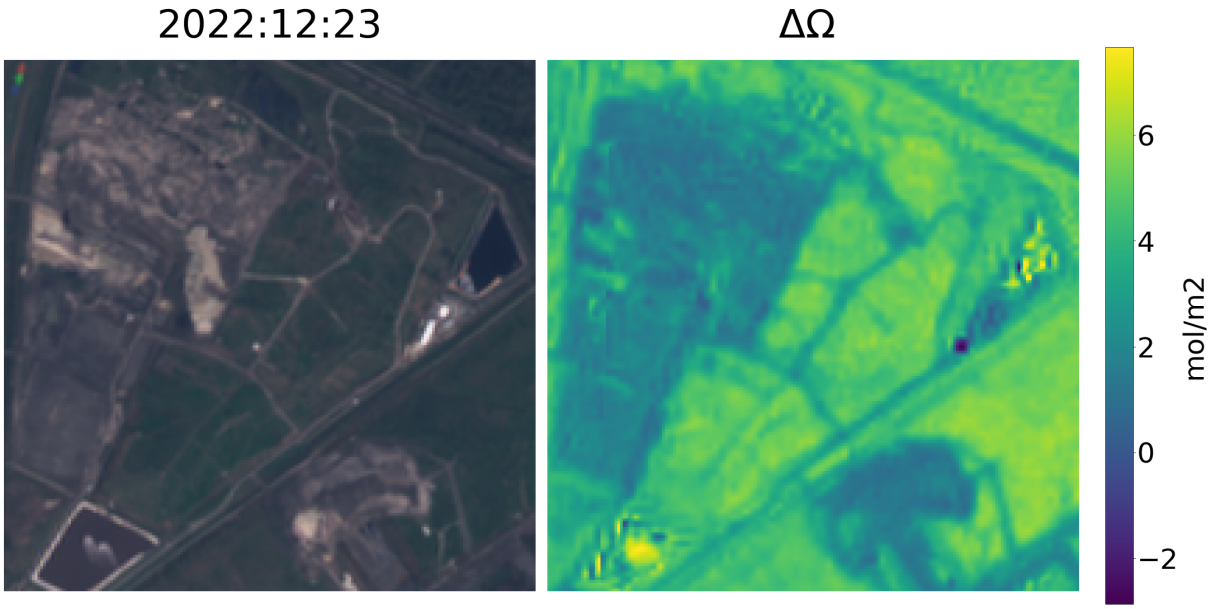

Figure 7.18 True color image and derived ΔΩ image for December 23rd. Note that the colorbar is fixed to match the one in figure 7.17, and values outside this range might have been truncated.

After comparing the ΔΩ enhancement images for the detected methane plumes to the true color images, most of the detections over non-water surfaces have shapes resembling surface features. Assuming that the detected methane plumes are actual, the similar shapes that are observed between the plumes and the surface features, could be explained by work, and digging in the landfill creating conditions were larger releases from the ground can arise. There is, however, a great possibility that there are surface features we are not able to identify

correctly with the naked eye that causes false readings. For example, if two mounds of different matter are disposed or dug up next to each other, and have similar absorption properties in the SWIR spectrum, they could appear as one single features in the ΔΩ image, even though they are easily distinguishable in the true color image. Hence, they could, even though there is no methane in the scene, be interpreted as one single methane plume if they combined have a plume-like shape.

7.4.3 Detections over water

Three out of the eight plume detections, detected March 1st, September 14th, and November 3rd, appear over a water covered area. Water is known to be a challenging background surface for methane detection, mainly due to the strong absorption in the SWIR-spectrum, which limits the reflection measured by the sensor, making it more difficult to separate methane SWIR absorption from sea surface roughness and instrument noise (Irakulis-Loitxate et al. 2022, ESA 2022, Valverde 2024). The high SWIR absorption of water can lead to falsely high methane enhancements and thus false positive plume detections due to e.g. water bodies and changes in surface moisture within the scene (Sherwin et. al 2024, Rouet-Leduc, B., & Hulbert, C., 2024, Zhang et. al 2023). The effect surface water can have on the methane enhancement maps may indicate that the observed plumes in the water-filled area can be false detections. Considering this, it is reasonable to assume that the detections found over this area were false. This is also supported by the concentrations found in the plumes over this area, as they appear to be much higher than what was found for the test sites (see e.g. Figure 6.18 & 6.20). For example, for March 1st, the concentrations of the methane plume appear to be more than 4 moles/m^2, whereas the concentrations for the test sites generally were between 0.5 and 2 moles/m^2. However, it should be mentioned that the area in question is very close to the persistent plume in location 1 that was observed by Cusworth et. al (2024) (See Figure 5.2.). Additionally, there is wastewater treatment infrastructure and a gas plant in the area, thus the chance of large methane releases occurring should not be disregarded completely. The challenging water background makes it difficult to detect methane, thus it is a possibility that only high-concentration releases are detectable over such areas, which supports the fact that the three detected releases here are large (12.5, 8.3 & 5.2 tons/hour for March 1st, September 14th and November 3rd.)

8 Conclusion

There are several contributing factors making the landfill investigated here a challenging location for methane detection. One is the satellite data used and most importantly the spatial and spectral resolutions of Sentinel-2. As the sensor is not specifically designed for methane detection and monitoring, the setup is not ideal for smaller and diffuse emissions. Moreover, methane detecting algorithms utilizing satellite data generally works best over homogenous and bright surfaces, and most have been developed for point source emissions. For the landfill investigated here we are looking at non-uniform backgrounds and as it is an active landfill the background also changes throughout the year (2022). The background is relatively dark, made up of mostly dark soils and vegetation, and it is therefore reasonable to assume a lower performance for the detection algorithm over the area, compared to the test sites.

Considering how vaguely the plumes in the test sites stand out from the background under ideal conditions, it seems probable that at least some of the plume detections over this landfill are a result of false readings, and that the actual methane concentrations above the landfill were not high enough to appear in the enhancement images. The fact that the methods in this study were not able to successfully detect the methane plumes June 4th, even though the emission rates found by Cusworth et. al (2024) were greater than several of the detections presented here (see section 6.4) support the conclusion. Higher concentration releases may overcome the issue with the heterogenous background, or using imagery from another sensor with higher spectral resolution for methane sensitive wavelengths might aid the detection. A higher spatial resolution may also help successful detection.

Several surface features of the land fill appear plume-like in the $\Delta\Omega$ images and can thus more easily be confused with methane plumes, compared to structures like buildings, parking lots etc. In addition, three out of the detected plumes are located over water, and low performance over such areas indicate that these detections may be inaccurate. The wind directions and wind speeds used for the quantification and evaluations are of such low spatial resolution, that they neither are considered to support nor contradict the plume detection algorithms success.

To conclude the findings in this thesis, the New Orleans land fill is challenging to monitor using Sentinel-2 data, due to its dark, heterogenous and changing background, and even though it is possible that some of the detections here are true methane plumes, it is more

likely false readings due to challenging surface properties and insufficient methane concentrations for the method that is used.

9 Further research

From what we could find in this study, the spectral resolution of Sentinel-2 and existing methods are not adequate to successfully monitor landfills and identify releases, even if the releases are of considerable size. However, compared to in situ measurements, remote sensing has a great advantage of covering large areas simultaneously, thus making it possible to identify unknown methane release sources. Considering this, we suggest exploring the performance of PRISMA images over landfills, as the spectral resolution is much higher compared to Sentinel-2, and with a spatial resolution of 30m which is less than at least some of the plume lengths found by Cusworth et. al (2024) over the U.S. landfills. The newly launched MethaneSAT aims to deliver freely available global emission data. The satellite is supposed to be able to identify excess methane of 3 ppb and monitor diffuse methane releases in areas down to about 1km^2, as well as point sources with a detection limit of 0.5 tons/hour (MethaneSAT n.d.). Thus, MethaneSAT could be a promising option for monitoring the releases in landfills, and this should be investigated further. Considering the large datasets of Sentinel-2 data available from 2015 and onwards, developing new methods for methane detection using the satellite that perform well over active landfills would be interesting. Even though detecting plumes and quantifying emission rates might be difficult with the spectral and spatial resolutions of the sensor, investigating seasonal or interannual trends and variations may be possible.

10 References

Allen, D. T. (2014). Methane emissions from natural gas production and use: reconciling bottom-up and top-down measurements. *Current Opinion in Chemical Engineering*, *5*, 78-83.

Blindheim, U. & Levy, F.E.S. (2022). *Metan.* Store norske leksikon. https://snl.no/metan#:~:text=kan%20v%C3%A6re%20eksplosive.-,Dannelse,i%20deponier%20for%20organisk%20avfall. [Last accessed May 28th 2024]

Britannica, T. Editors of Encyclopaedia (2024). *methane*. *Encyclopedia Britannica*. https://www.britannica.com/science/methane [Last accessed May 28th 2024]

Buseth, J.M. (2023)(1) Methane detection from satellites – a literature review. [Unpublished project paper, UiT The Arctic University of Norway]

Buseth, J.M. (2023)(2) Methane – understanding emission sources and climate consequences. [Unpublished written exam, UiT The Arctic University of Norway]

Chen, Z., Jacob, D. J., Gautam, R., Omara, M., Stavins, R. N., Stowe, R. C., Nesser, H., Sulprizio, M. P., Lorente, A., Varon, D. J., Lu, X., Shen, L., Qu, Z., Pendergrass, D. C., & Hancock, S. (2023). Satellite quantification of methane emissions and oil–gas methane intensities from individual countries in the Middle East and North Africa: implications for climate action. *Atmospheric Chemistry and Physics*, *23*(10), 5945–5967. https://doi.org/10.5194/acp-23-5945-2023

Cusworth, D. H., Duren, R. M., Ayasse, A. K., Jiorle, R., Howell, K., Aubrey, A., Green, R. O., Eastwood, M. L., Chapman, J. W., Thorpe, A. K., Heckler, J., Asner, G. P., Smith, M. L., Thoma, E., Krause, M. J., Heins, D., & Thorneloe, S. (2024). Quantifying methane emissions from United States landfills. *Science*, *383*(6690), 1499–1504. https://doi.org/10.1126/science.adi7735

De Gouw, J. A., Veefkind, J. P., Roosenbrand, E., Dix, B., Lin, J. C., Landgraf, J., & Levelt, P. F. (2020). Daily satellite observations of methane from oil and gas production regions in the United States. *Scientific reports*, *10*(1), 1379.

Dogniaux, M., Maasakkers, J. D., Varon, D. J., & Aben, I. (2023). Report on Landsat 8 and Sentinel-2B observations of the Nord Stream 2 pipeline methane leak. Under review for Atmospheric Measurement Techniques (AMT). doi :https://doi.org/10.31223/X53M42

eoPortal (2012). *PRISMA (Hyperspectral)*. https://www.eoportal.org/satellite-missions/prisma-hyperspectral#eop-quick-facts-section [Acsessed: 13th of December 2023]

Ehret, T., De Truchis, A., Mazzolini, M., Morel, J., D'Aspremont, A., Lauvaux, T., Duren, R., Cusworth, D., & Facciolo, G. (2022). Global Tracking and Quantification of Oil and Gas Methane Emissions from Recurrent Sentinel-2 Imagery. *Environmental Science & Technology*, *56*(14), 10517–10529. https://doi.org/10.1021/acs.est.1c08575

Gorroño, J., Varon, D. J., Irakulis-Loitxate, I., & Guanter, L. (2023). Understanding the potential of Sentinel-2 for monitoring methane point emissions. *Atmospheric Measurement Techniques*, *16*(1), 89-107.

Groshenry, A., Giron, C., Lauvaux, T., d'Aspremont, A., & Ehret, T. (2022). Detecting methane plumes using prisma: Deep learning model and data augmentation. *arXiv preprint arXiv:2211.15429*.

Guanter, L., Irakulis-Loitxate, I., Gorroño, J., Sánchez-García, E., Cusworth, D. H., Varon, D. J., Cogliati, S., & Colombo, R. (2021). Mapping methane point emissions with the PRISMA spaceborne imaging spectrometer. *Remote Sensing of Environment*, *265*, 112671. https://doi.org/10.1016/j.rse.2021.112671

Global Modeling and Assimilation Office (GMAO) (2015), MERRA-2 tavg1_2d_slv_Nx: 2d,1-Hourly, Time-Averaged, Single-Level, Assimilation, Single-Level Diagnostics V5.12.4, Greenbelt, MD, USA, Goddard Earth Sciences Data and Information Services Center (GES DISC), Accessed: 2024-05-16, doi: 10.5067/VJAFPLI1CSIV

Hayden, A., & Christy, J. (2023). Maxar's WorldView-3 Enables Low-Concentration Methane Detection from Space., doi: https://doi.org/10.31223/X51T1C

IEA (2021), *Methane Tracker 2021*, IEA, Paris https://www.iea.org/reports/methane-tracker-2021, License: CC BY 4.0

IEA (2023), *Global Methane Tracker 2023*, IEA, Paris https://www.iea.org/reports/global-methane-tracker-2023, License: CC BY 4.0

IEA (2024), *Global Methane Tracker 2024*, IEA, Paris https://www.iea.org/reports/global-methane-tracker-2024, License: CC BY 4.0

IPCC, 2023: Section 2,3. In: Climate Change 2023: Synthesis Report. Contribution of Working Groups I, II and III to the Sixth Assessment Report of the Intergovernmental Panel on Climate Change [Core Writing TeamS, H. Lee and J. Romero (eds.)]. IPCC, Geneva, Switzerland, pp. 35-115, doi: 10.59327/IPCC/AR6-9789291691647

IPCC, 2023: Summary for Policymakers. In: Climate Change 2023: Synthesis Report. Contribution of Working Groups I, II and III to the Sixth Assessment Report of the Intergovernmental Panel on Climate Change [Core Writing Team, H. Lee and J. Romero (eds.)]. IPCC, Geneva, Switzerland, pp. 1-34, doi: 10.59327/IPCC/AR6-9789291691647.001

Irakulis-Loitxate, I., Gorroño, J., Zavala-Araiza, D., & Guanter, L. (2022). Satellites Detect a Methane Ultra-emission Event from an Offshore Platform in the Gulf of Mexico. *Environmental Science & Technology Letters*, *9*(6), 520–525. https://doi.org/10.1021/acs.estlett.2c00225

Irakulis-Loitxate, I., Guanter, L., Liu, Y. N., Varon, D. J., Maasakkers, J. D., Zhang, Y., ... & Jacob, D. J. (2021). Satellite-based survey of extreme methane emissions in the Permian basin. *Science Advances*, *7*(27), eabf4507.

Irakulis-Loitxate I, Roger J, Gorroño J, Valverde A, Guanter L. (2023) Detection of Methane Point Sources with High-Resolution Satellites. *Environmental Sciences Proceedings*; 28(1):29. https://doi.org/10.3390/environsciproc2023028029

Jia, M., Li, F., Zhang, Y., Wu, M., Li, Y., Feng, S., ... & Jiang, F. (2022). The Nord Stream pipeline gas leaks released approximately 220,000 tonnes of methane into the atmosphere. *Environmental Science and Ecotechnology*, *12*, 100210.

Kochanov R.V, Gordon I. E, Rothman L.S., Wcislo, P, Hill, C. Wilzewski J.S, HITRAN Application Program ming Interface (HAPI): A comprehensive approach to working with spectroscopic data, J. Quant. Spectrosc. Rad iat. Transfer 177, 15-30 (2016) DOI: 10.1016/j.jqsrt.2016.03.005

Landsat-8 (n.d.). United States Geological Survey. https://www.usgs.gov/landsat-missions/landsat-8#:~:text=Landsat%208%20images%20have%2015,km%20(115%20mi)%20swath. [Last accessed: 2024-05-14]

Lorente, A., Borsdorff, T., Butz, A., Hasekamp, O., Schneider, A., Wu, L., ... & Landgraf, J. (2021). Methane retrieved from TROPOMI: improvement of the data product and validation of the first 2 years of measurements. *Atmospheric Measurement Techniques*, *14*(1), 665-684.

Lorente, A., Borsdorff, T., Martinez-Velarte, M. C., Butz, A., Hasekamp, O. P., Wu, L., and Landgraf, J (2022). Evaluation of the methane full-physics retrieval applied to TROPOMI ocean sun glint measurements, Atmos. Meas. Tech., 15, 6585–6603, https://doi.org/10.5194/amt-15-6585-2022

Mamen, J. & Benestad, R. (2023). Drivhuseffekten [The greenhouse effect]. Store norske leksikon. https://snl.no/drivhuseffekten [Last accessed 2024-05-27]

Maryland department of the environment (MDE) (2023). *Maryland's Climate Pollution Reduction Plan.* [Appendix: Methane measurement and monitoring] https://mde.maryland.gov/programs/air/ClimateChange/Pages/Maryland%27s-Climate-Pollution-Reduction-Plan.aspx [Last accessed 2024-05-27].

MethaneSAT. (n.d.). MethaneSAT. https://www.methanesat.org/satellite/ [Last accessed 2024 05-29]

National Academies of Sciences, Engineering, and Medicine. 2018. *Improving Characterization of Anthropogenic Methane Emissions in the United States.* Washington, DC: The National Academies Press. doi: https://doi.org/10.17226/24987.

Ocko, I. B., Sun, T., Shindell, D., Oppenheimer, M., Hristov, A. N., Pacala, S. W., Mauzerall, D. L., Xu, Y., & Hamburg, S. P. (2021). Acting rapidly to deploy readily available methane mitigation measures by sector can immediately slow global warming. *Environmental Research Letters*, *16*(5), 054042. https://doi.org/10.1088/1748-9326/abf9c8

Pandey, S., van Nistelrooij, M., Maasakkers, J. D., Sutar, P., Houweling, S., Varon, D. J., ... & Aben, I. (2023). Daily detection and quantification of methane leaks using Sentinel-3: a tiered satellite observation approach with Sentinel-2 and Sentinel-5p. *Remote Sensing of Environment*, *296*, 113716.

PRISMA (Hyperspectral) (2012). https://www.eoportal.org/satellite-missions/prisma-hyperspectral#prisma-hyperspectral-precursor-and-application-mission [Last accessed 2024-05-14]

Radman, A., Mahdianpari, M., Varon, D. J., & Mohammadimanesh, F. (2023). S2MetNet: A novel dataset and deep learning benchmark for methane point source quantification using Sentinel-2 satellite imagery. *Remote Sensing of Environment*, *295*, 113708.

River Birch LLC (n.d.) CHWMEG inc. https://chwmeg.org/detail.asp?ID=472 [Last accessed 2024-05-23]

Rouet-Leduc, B., & Hulbert, C. (2024). Automatic detection of methane emissions in multispectral satellite imagery using a vision transformer. *Nature Communications*, *15*(1). https://doi.org/10.1038/s41467-024-47754-y

Rouet-Leduc, B., Kerdreux, T., Tuel, A., & Hulbert, C. (2023). Autonomous Detection of Methane Emissions in Multispectral Satellite Data Using Deep Learning. *arXiv preprint arXiv:2308.11003*.

Sánchez-García, E., Gorroño, J., Irakulis-Loitxate, I., Varon, D. J., & Guanter, L. (2022). Mapping methane plumes at very high spatial resolution with the WorldView-3 satellite. *Atmospheric Measurement Techniques*, *15*(6), 1657-1674.

Satellites detect methane plume in Nord Stream leak (2022). ESA. https://www.esa.int/Applications/Observing_the_Earth/Satellites_detect_methane_plume_in_Nord_Stream_leak [Last accessed May 25th 2022].

Saunois, M., Stavert, A. R., Poulter, B., Bousquet, P., Canadell, J. G., Jackson, R. B., Raymond, P. A., Dlugokencky, E. J., Houweling, S., Patra, P. K., Ciais, P., Arora, V. K., Bastviken, D., Bergamaschi, P., Blake, D. R., Brailsford, G., Bruhwiler, L., Carlson, K. M., Carrol, M., Castaldi, S., Chandra, N., Crevoisier, C., Crill, P. M., Covey, K., Curry, C. L., Etiope, G., Frankenberg, C., Gedney, N., Hegglin, M. I., Höglund-Isaksson, L., Hugelius, G., Ishizawa, M., Ito, A., Janssens-Maenhout, G., Jensen, K. M., Joos, F., Kleinen, T., Krummel, P. B., Langenfelds, R. L., Laruelle, G. G., Liu, L., Machida, T., Maksyutov, S., McDonald, K. C., McNorton, J., Miller, P. A., Melton, J. R., Morino, I., Müller, J., Murguia-Flores, F., Naik, V., Niwa, Y., Noce, S., O'Doherty,

S., Parker, R. J., Peng, C., Peng, S., Peters, G. P., Prigent, C., Prinn, R., Ramonet, M., Regnier, P., Riley, W. J., Rosentreter, J. A., Segers, A., Simpson, I. J., Shi, H., Smith, S. J., Steele, L. P., Thornton, B. F., Tian, H., Tohjima, Y., Tubiello, F. N., Tsuruta, A., Viovy, N., Voulgarakis, A., Weber, T. S., van Weele, M., van der Werf, G. R., Weiss, R. F., Worthy, D., Wunch, D., Yin, Y., Yoshida, Y., Zhang, W., Zhang, Z., Zhao, Y., Zheng, B., Zhu, Q., Zhu, Q., and Zhuang, Q. (2020). The Global Methane Budget 2000–2017, *Earth Syst. Sci. Data*, 12, 1561–1623, https://doi.org/10.5194/essd-12-1561-2020.

Schuit, B. J., Maasakkers, J. D., Bijl, P., Mahapatra, G., Van Den Berg, A., Pandey, S., Lorente, A., Borsdorff, T., Houweling, S., Varon, D. J., McKeever, J., Jervis, D., Girard, M., Irakulis Loitxate, I., Gorroño, J., Guanter, L., Cusworth, D. H., & Aben, I. (2023). Automated detection and monitoring of methane super-emitters using satellite data. *Atmospheric Chemistry and Physics*, *23*(16), 9071–9098. https://doi.org/10.5194/acp-23-9071-2023

Sentinel-2 MSI User Guide (n.d.). European space agency. https://sentinels.copernicus.eu/web/sentinel/user-guides/sentinel-2-msi [Last accessed: 2024-05-12]

Sentinel-2 MSI Technical Guide (n.d.) European space agency. https://sentinels.copernicus.eu/web/sentinel/technical-guides/sentinel-2-msi [Last accessed: 2024-05-14]

Sentinel-3 SLSTR User guide (n.d.) European space agency. https://sentinels.copernicus.eu/web/sentinel/user-guides/sentinel-3-slstr [Last accessed: 2024-05-12]

Sentinel-5P (n.d.). Sentinelhub. https://custom-scripts.sentinel-hub.com/custom-scripts/sentinel/sentinel-5p/#:~:text=The%20TROPOspheric%20Monitoring%20Instrument%20(TROPOMI,3%20(2305%2D2385nm). [Last accessed: 2024-05-12]

Sentinel-5P TROPOMI User Guide (n.d.) European space agency. https://sentinels.copernicus.eu/web/sentinel/user-guides/sentinel-5p-tropomi [Last acsessed 2024-05-12]

Sheng, J., Song, S., Zhang, Y., Prinn, R. G., & Janssens-Maenhout, G. (2019). Bottom-up estimates of coal mine methane emissions in China: A gridded inventory, emission factors, and trends. *Environmental Science & Technology Letters*, *6*(8), 473-478.

Sherwin, E. D., Rutherford, J. S., Chen, Y., Aminfard, S., Kort, E. A., Jackson, R. B., & Brandt, A. R. (2023). Single-blind validation of space-based point-source detection and quantification of onshore methane emissions. *Scientific Reports*, *13*(1), 3836.

Sherwin, E. D., El Abbadi, S. H., Burdeau, P. M., Zhang, Z., Chen, Z., Rutherford, J. S., ... & Brandt, A. R. (2024). Single-blind test of nine methane-sensing satellite systems from three continents. *Atmospheric Measurement Techniques*, *17*(2), 765-782.

United Nations (n.d.) (1) For a livable climate: Net-zero commitments must be backed by credible action. https://www.un.org/en/climatechange/net-zero-coalition [Last accessed May 27th 2024]

United Nations (n.d.)(2) The Paris Agreement. https://www.un.org/en/climatechange/paris-agreement [Last accessed 2024-05-27]

Varon, D. J., Jacob, D. J., McKeever, J., Jervis, D., Durak, B. O., Xia, Y., & Huang, Y. (2018). Quantifying methane point sources from fine-scale satellite observations of atmospheric methane plumes. *Atmospheric Measurement Techniques*, *11*(10), 5673-5686

Varon, D. J., Jervis, D., McKeever, J., Spence, I., Gains, D., & Jacob, D. J. (2021). High-frequency monitoring of anomalous methane point sources with multispectral Sentinel-2 satellite observations. *Atmospheric Measurement Techniques*, *14*(4), 2771-2785.

Valverde, A., Irakulis-Loitxate, I., Roger, J., Gorroño, J., & Guanter, L. (2024). Satellite Characterization of Methane Point Sources by Offshore Oil and Gas PlatForms. *Environmental Sciences Proceedings*, *28*(1), 22.

Watine-Guiu, M., Varon, D. J., Irakulis-Loitxate, I., Balasus, N., & Jacob, D. J. (2023). Geostationary satellite observations of extreme and transient methane emissions from oil and gas infrastructure. *Proceedings of the National Academy of Sciences*, *120*(52), e2310797120.

Wiström, L.M. Kristiansen J.R. & Grøn, Ø (2021). Elektromagnetisk spektrum [Electromagnetic spectrum]. Store norske leksikon. https://snl.no/elektromagnetisk_spektrum#:~:text=Elektromagnetisk%20spektrum%20er%20alle%20typer,lengst%20b%C3%B8lgengde%20og%20lavest%20frekvens). [Last accessed 2024-05-14]

WorldView-3 (n.d.). European space agency. https://earth.esa.int/eogateway/missions/worldview-3 (Last accessed 2024-05-12)

Zhang, Z., Sherwin, E. D., Varon, D. J., & Brandt, A. R. (2022). Detecting and quantifying methane emissions from oil and gas production: algorithm development with ground-truth calibration based on Sentinel-2 satellite imagery. *Atmospheric Measurement Techniques*, *15*(23), 7155-7169.

Zhang, S., Ma, J., Zhang, X., & Guo, C. (2023). Atmospheric remote sensing for anthropogenic methane emissions: Applications and research opportunities. *Science of the Total Environment*, *893*, 164701. https://doi.org/10.1016/j.scitotenv.2023.164701

11 Appendix

In this appendix the true color images of the New Orleans landfill and the respective derived ΔΩ for all cloud free satellite overpasses in 2022. Note that the images that have been presented in the thesis are excluded from the appendix.

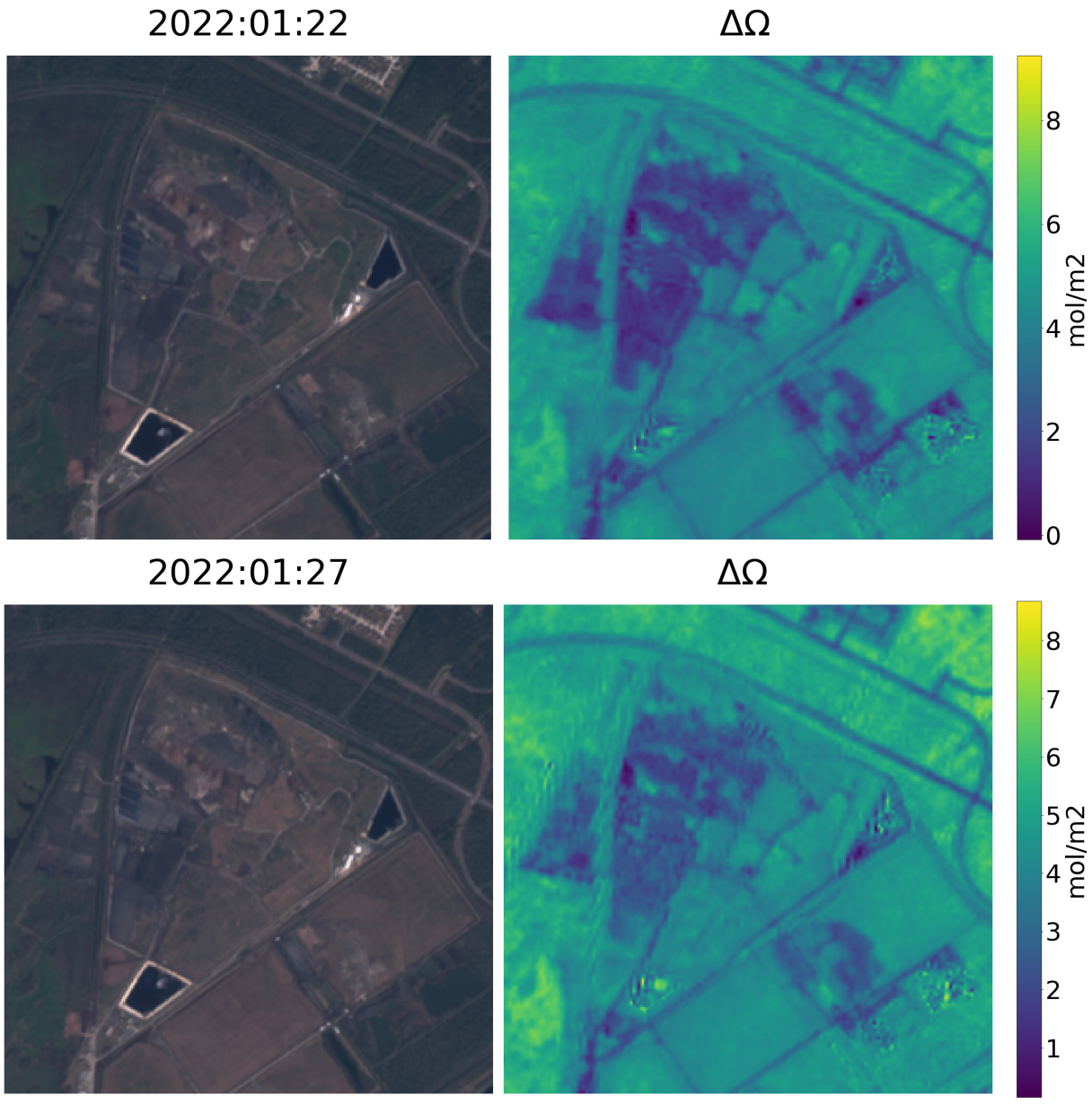

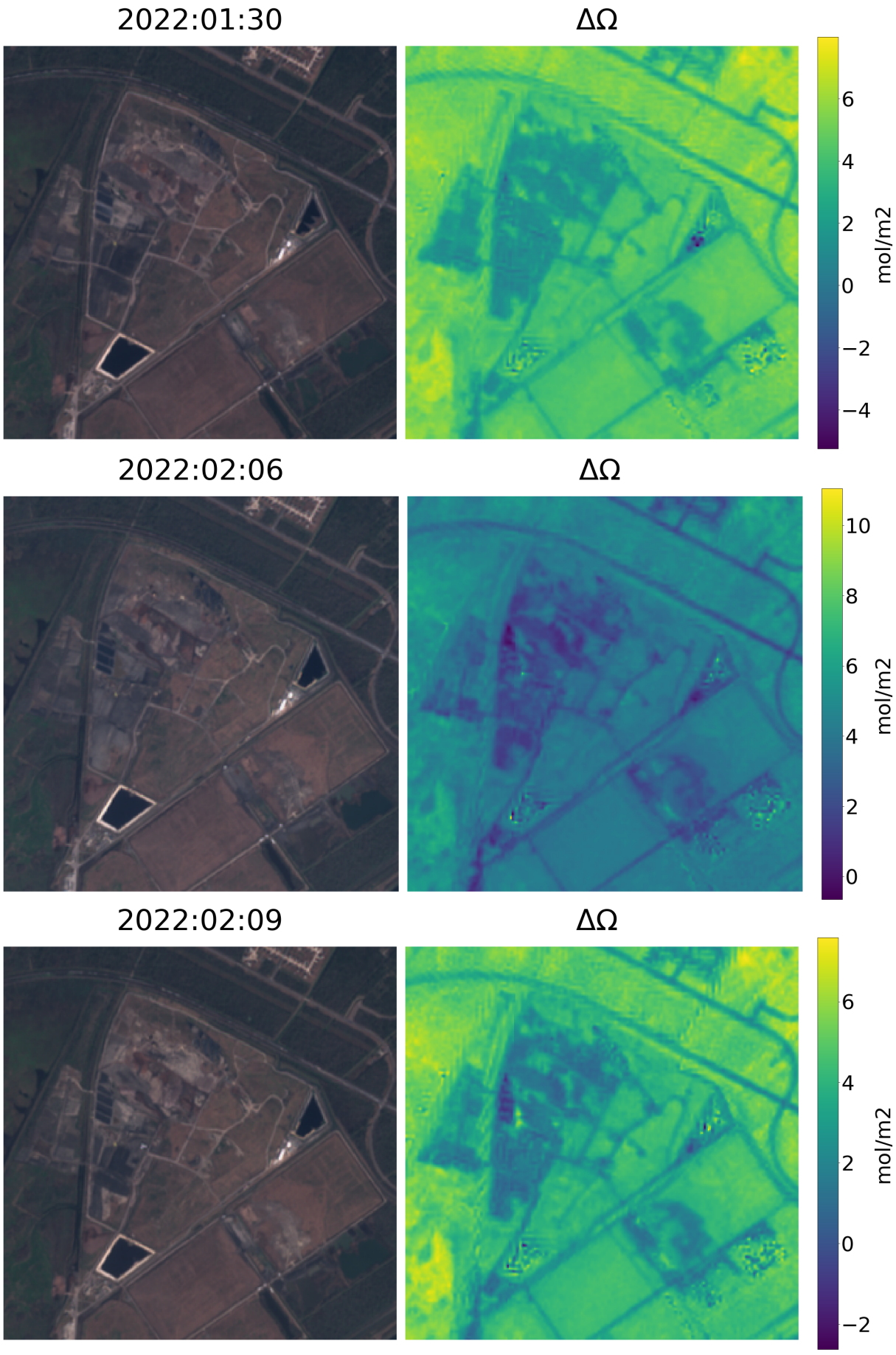
2022:01:30
ΔΩ
6
4
2
0
−2
−4
mol/m2
2022:02:06
ΔΩ
10
8
6
4
2
0
mol/m2
2022:02:09
ΔΩ
6
4
2
0
−2
mol/m2

2022:02:11 ΔΩ

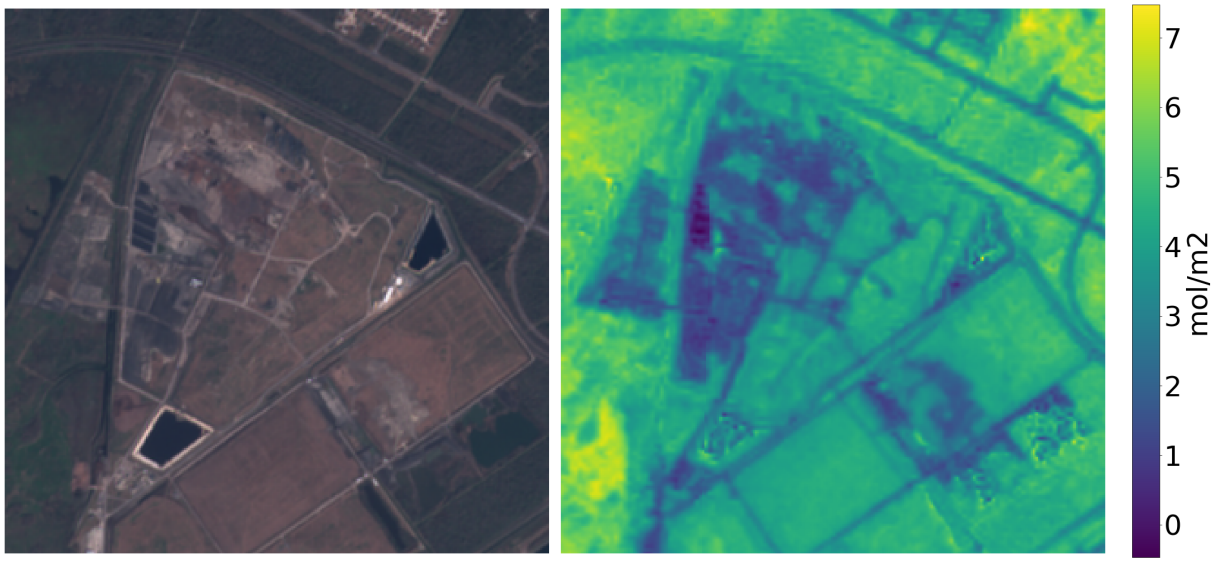

2022:02:14 ΔΩ

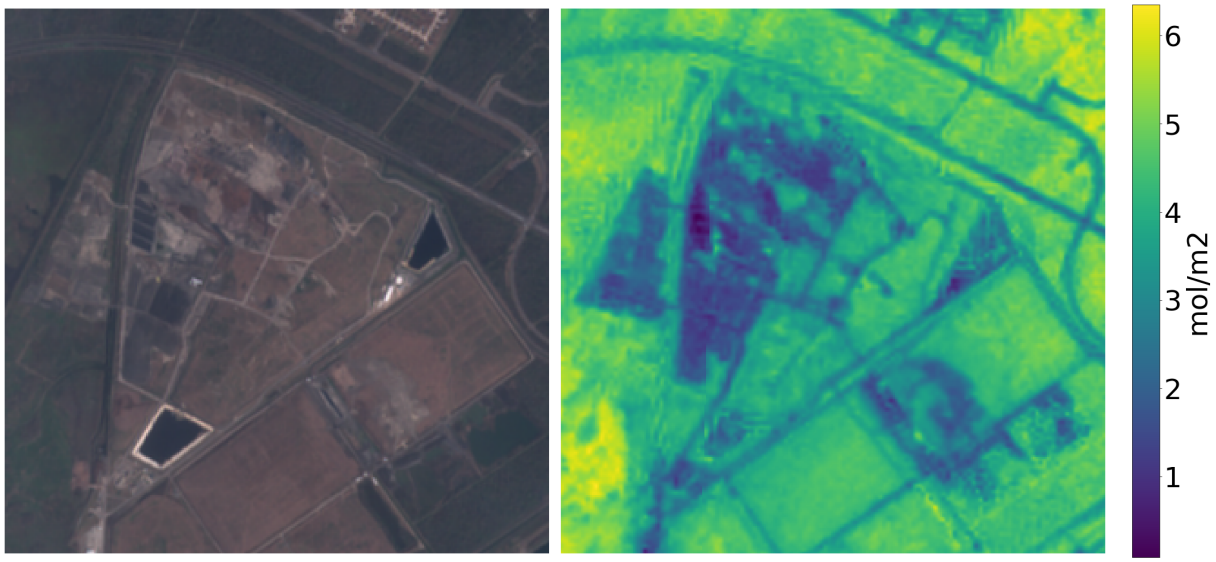

2022:03:06 ΔΩ

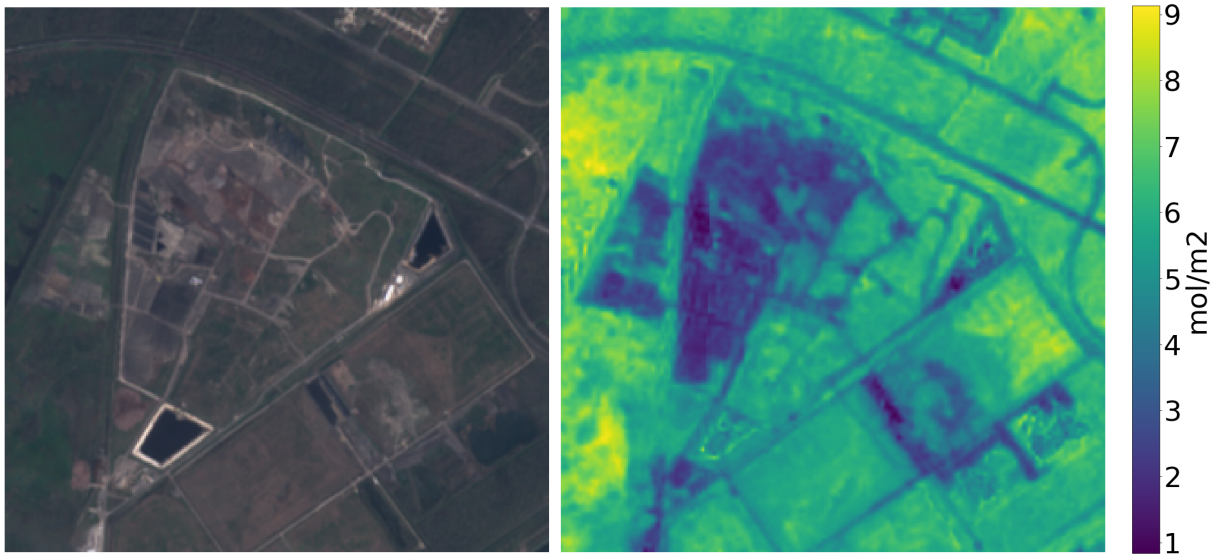

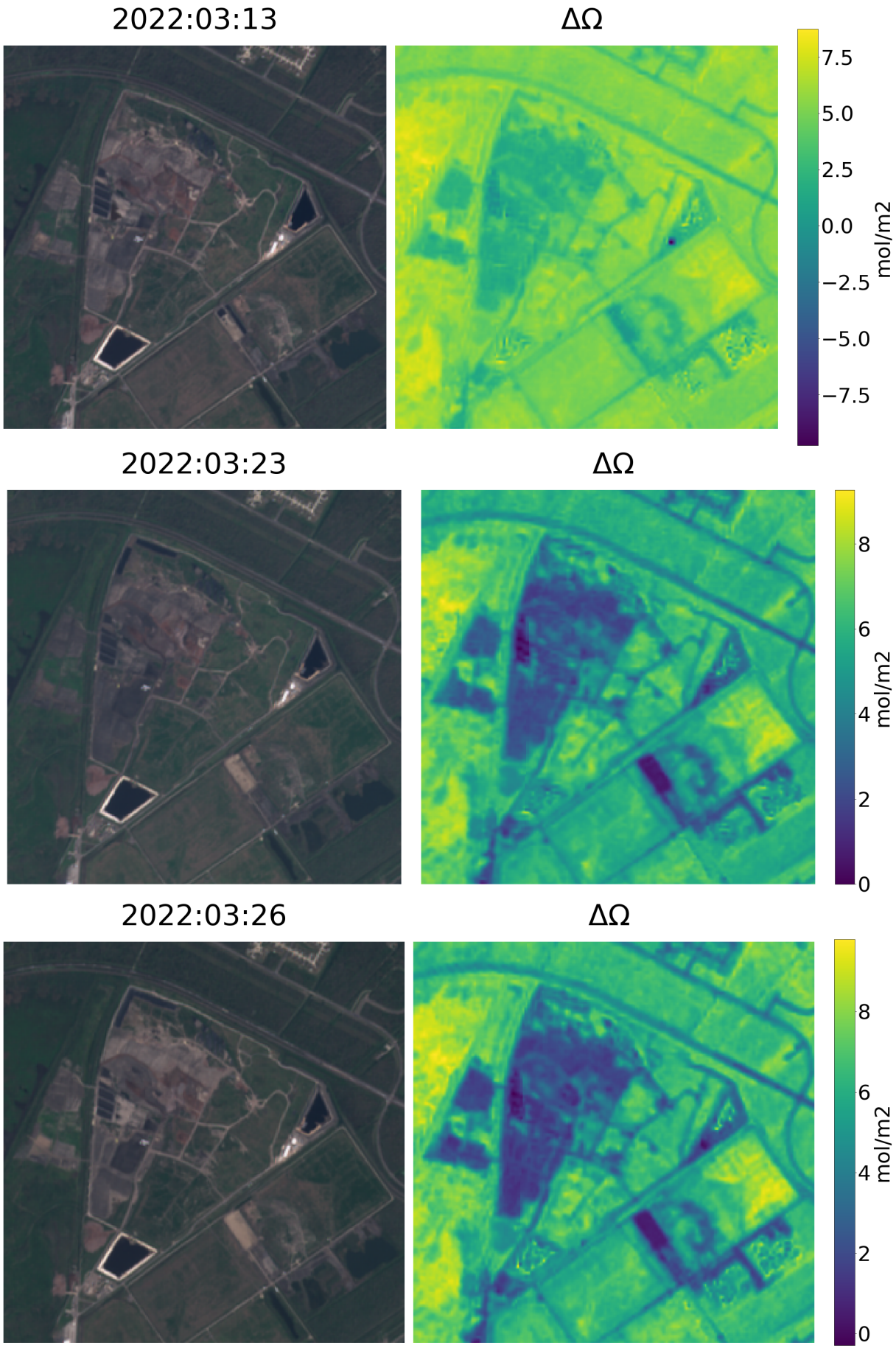
2022:03:13
ΔΩ
7.5
5.0
2.5
0.0
−2.5
−5.0
−7.5
mol/m2
2022:03:23
ΔΩ
8
6
4
2
0
mol/m2
2022:03:26
ΔΩ
8
6
4
2
0
mol/m2

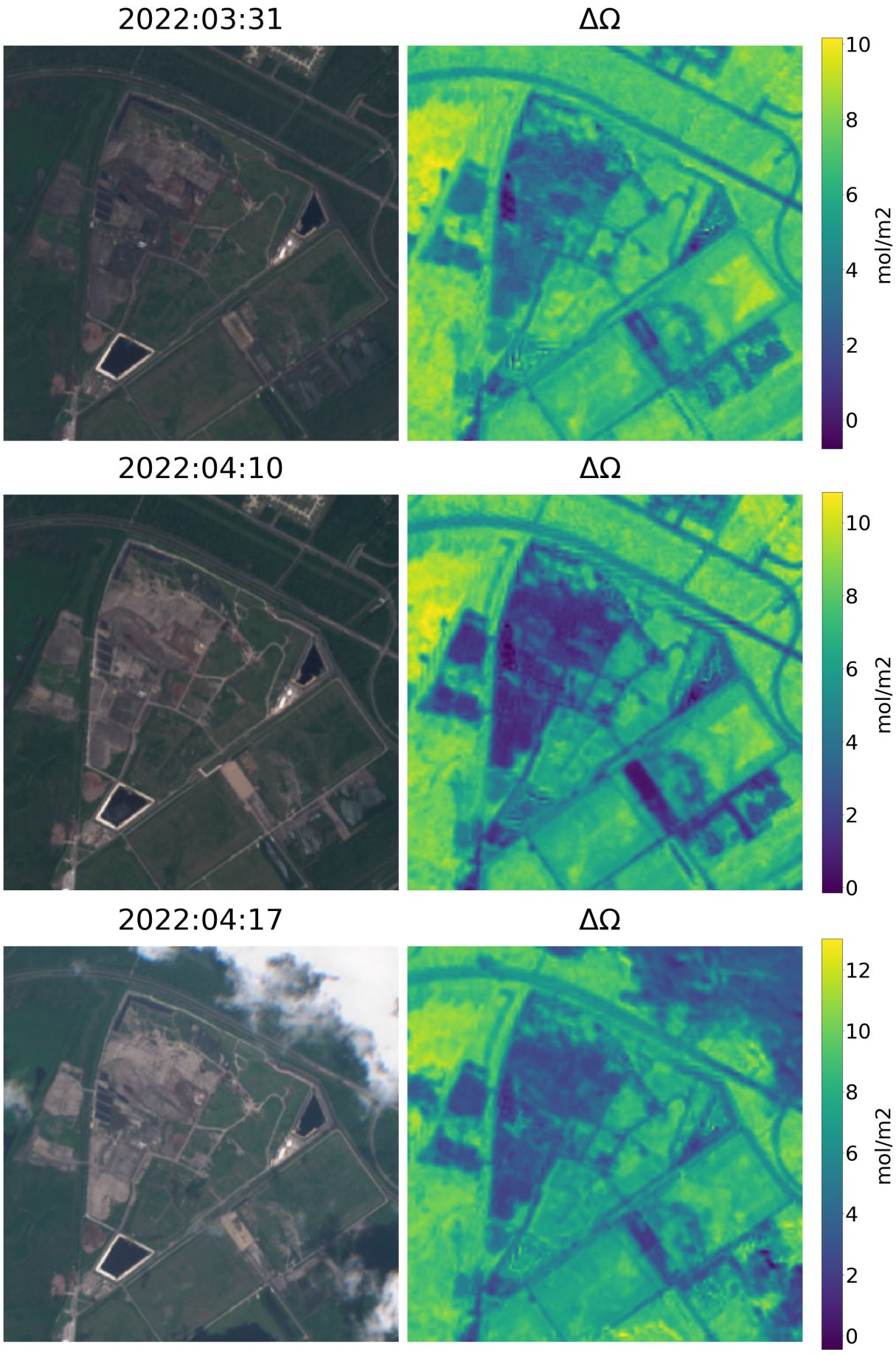
2022:03:31
ΔΩ
10
8
6
4
2
0
mol/m2
2022:04:10
ΔΩ
10
8
6
4
2
0
mol/m2
2022:04:17
ΔΩ
12
10
8
6
4
2
0
mol/m2

2022:05:12 ΔΩ

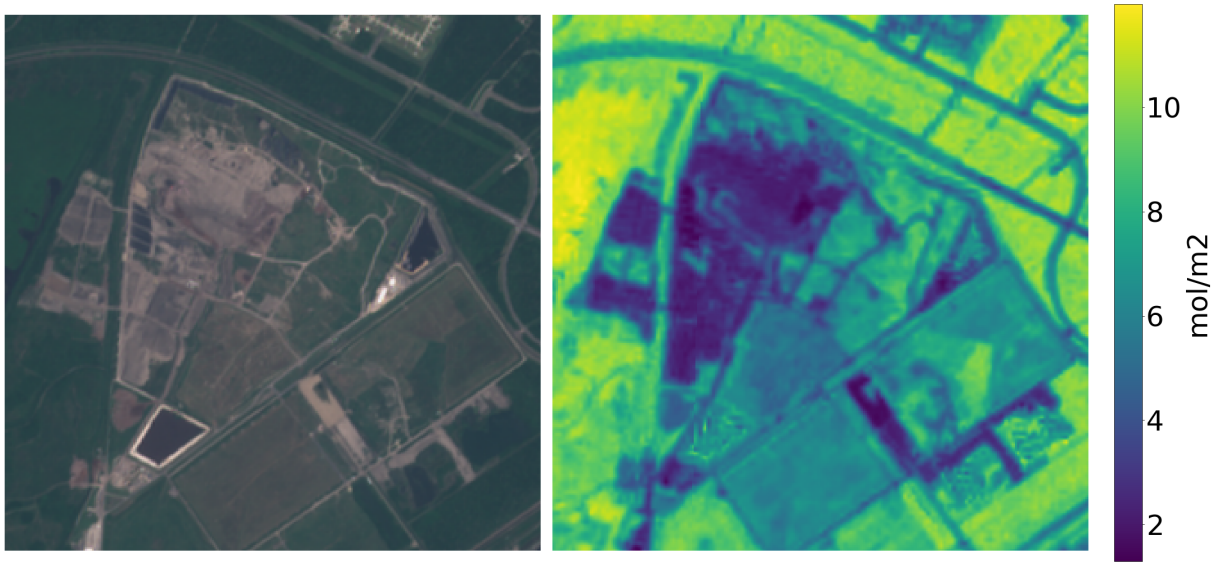

2022:05:27 ΔΩ

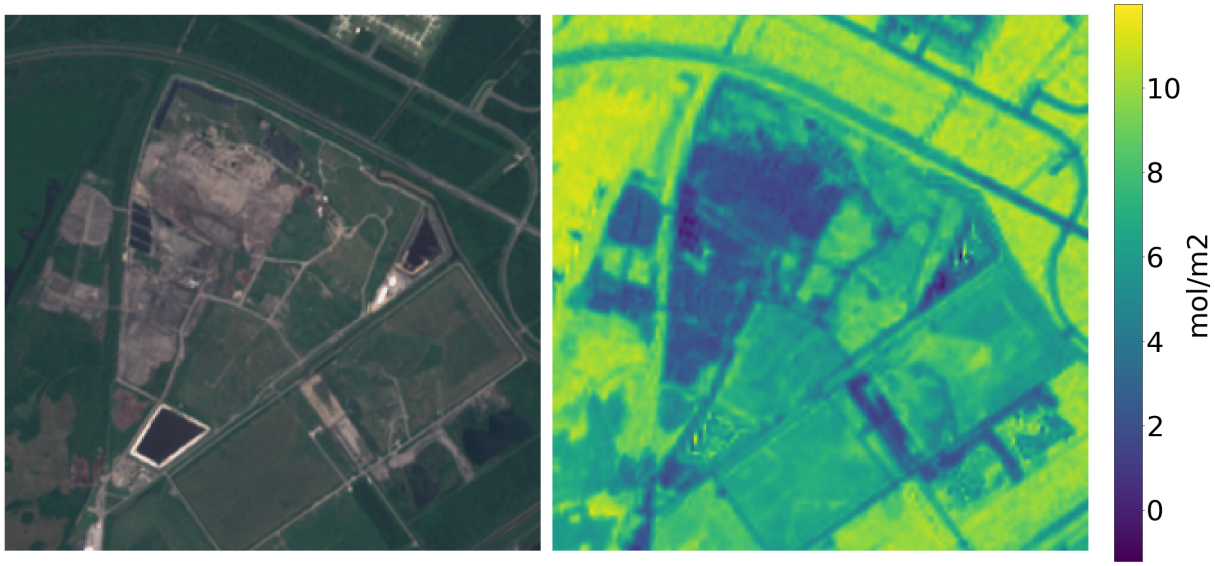

2022:06:06 ΔΩ

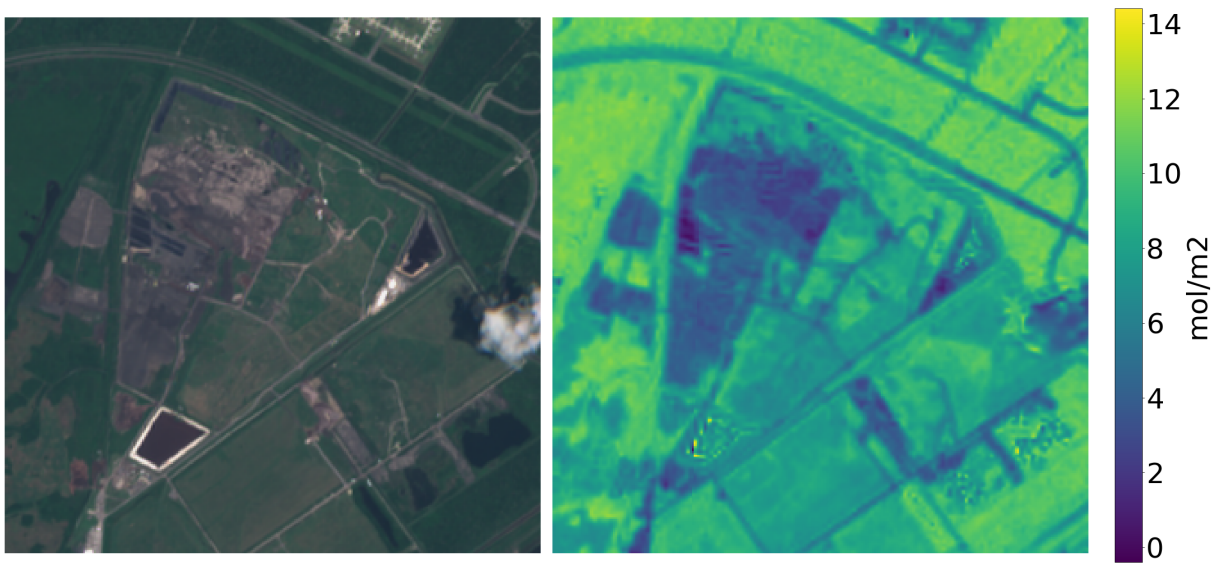

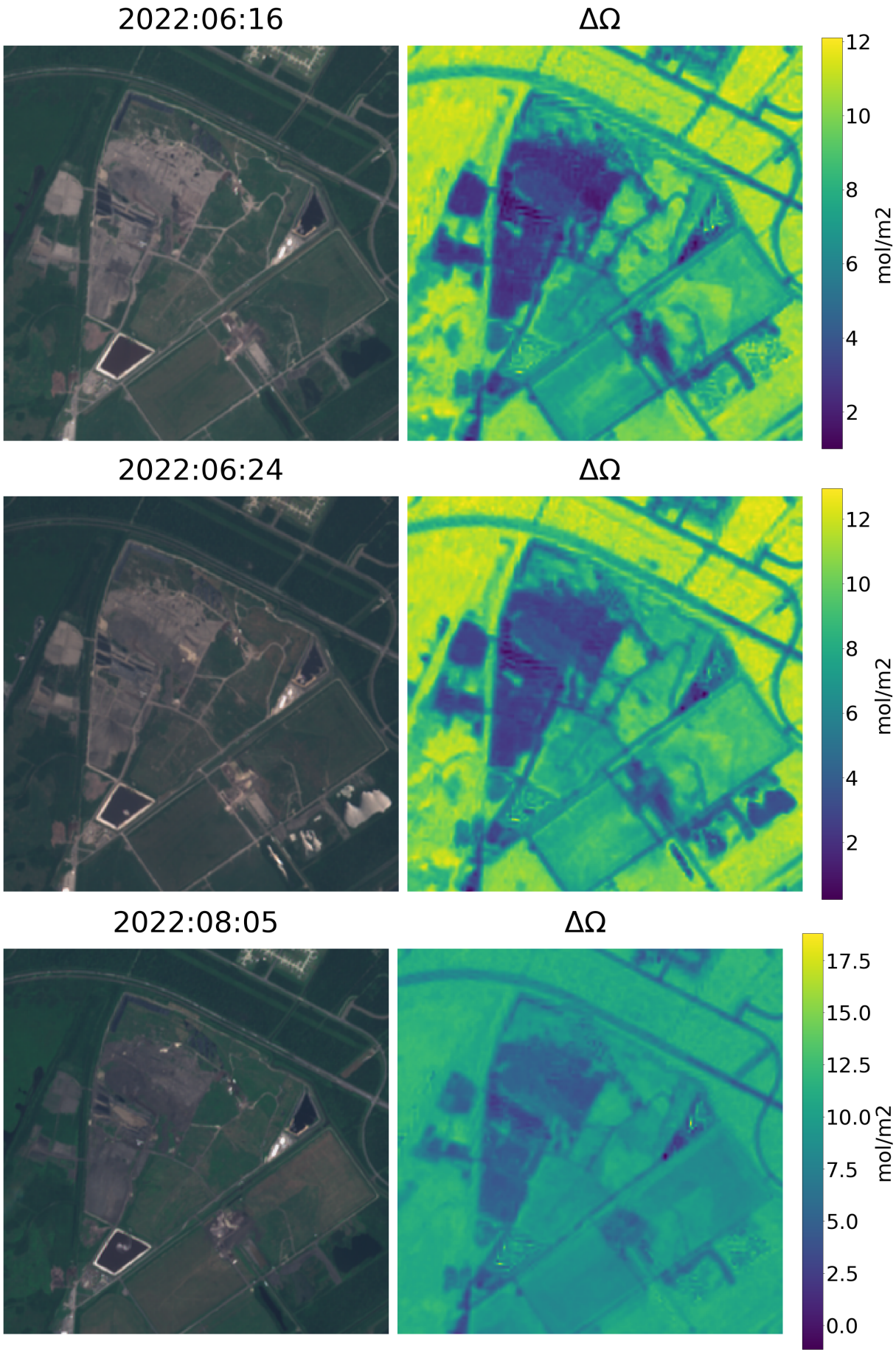
2022:06:16
ΔΩ
12
10
8
6
4
2
mol/m2
2022:06:24
ΔΩ
12
10
8
6
4
2
mol/m2
2022:08:05
ΔΩ
17.5
15.0
12.5
10.0
7.5
5.0
2.5
0.0
mol/m2

2022:09:27 ΔΩ

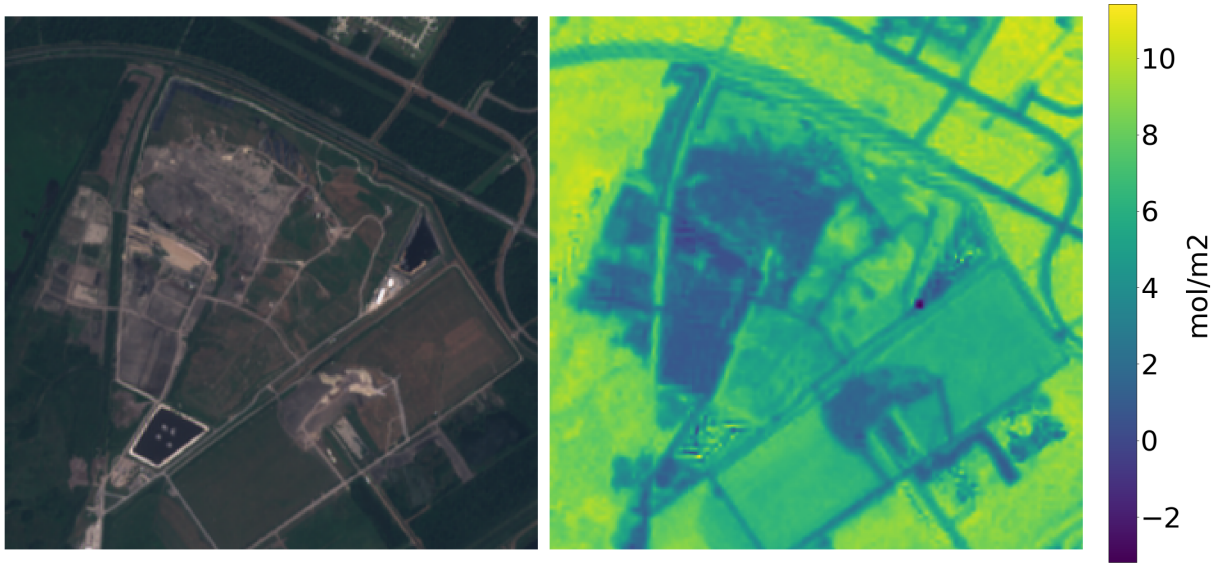

2022:09:29 ΔΩ

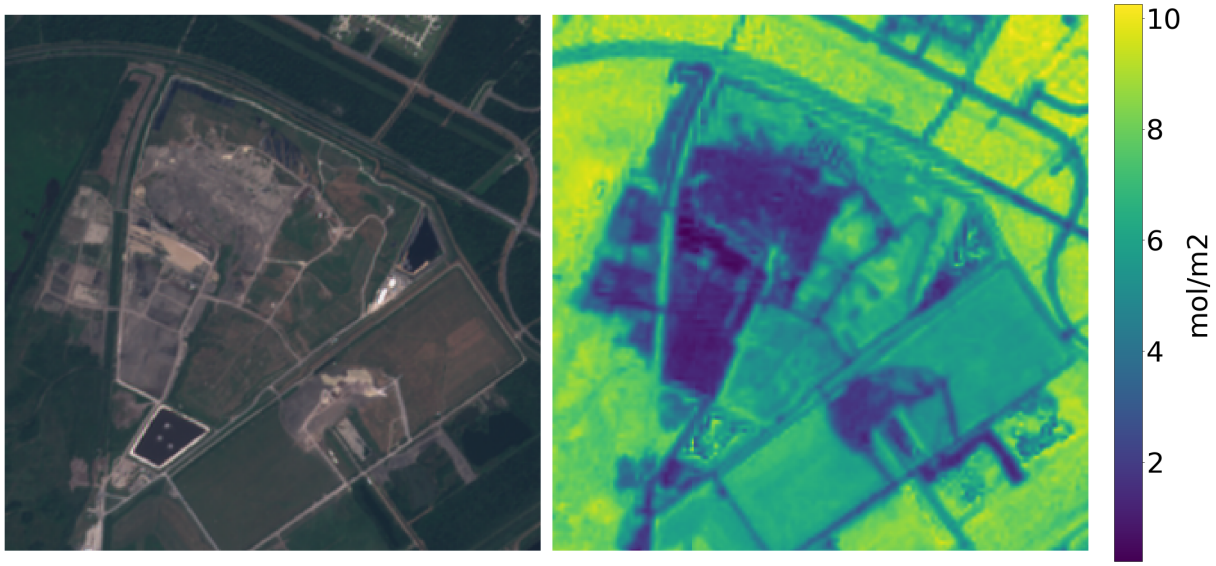

2022:10:02 ΔΩ

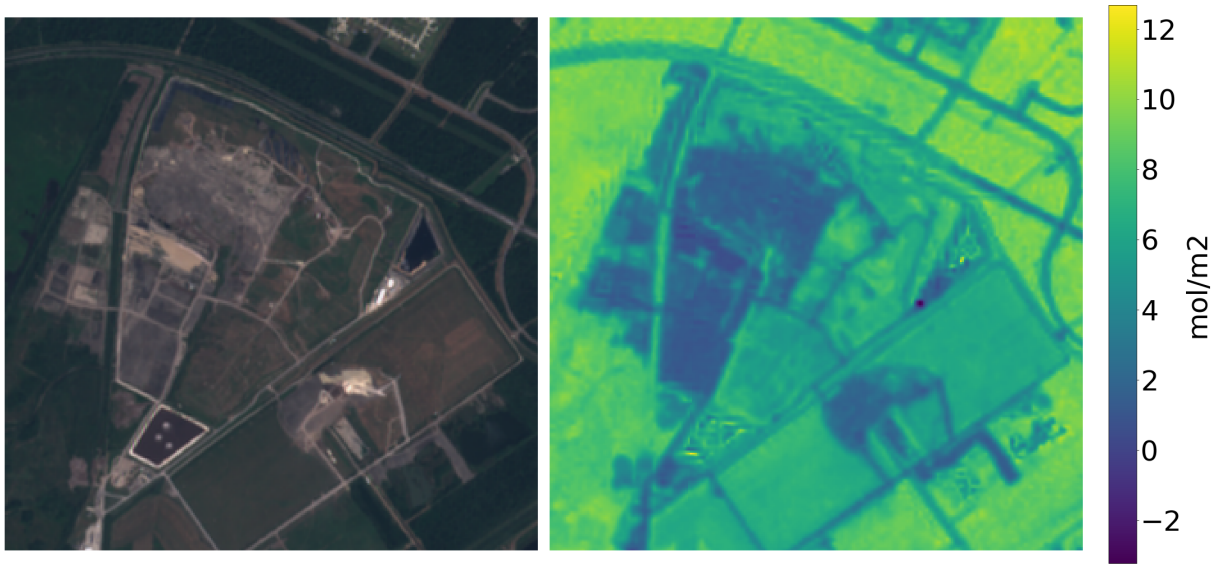

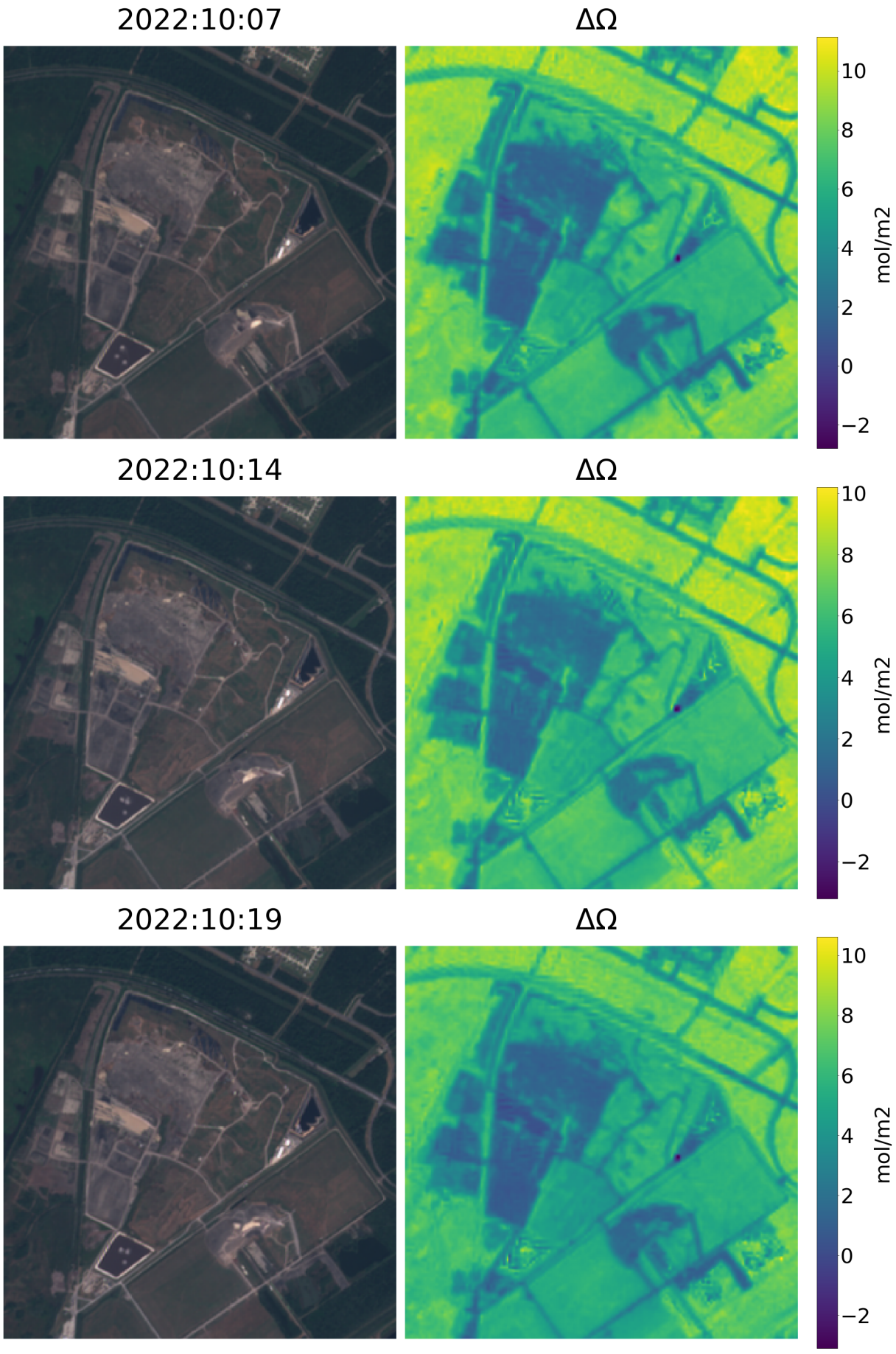
2022:10:07
ΔΩ
2022:10:14
ΔΩ
2022:10:19
ΔΩ
10
8
6
4
2
0
−2
mol/m2

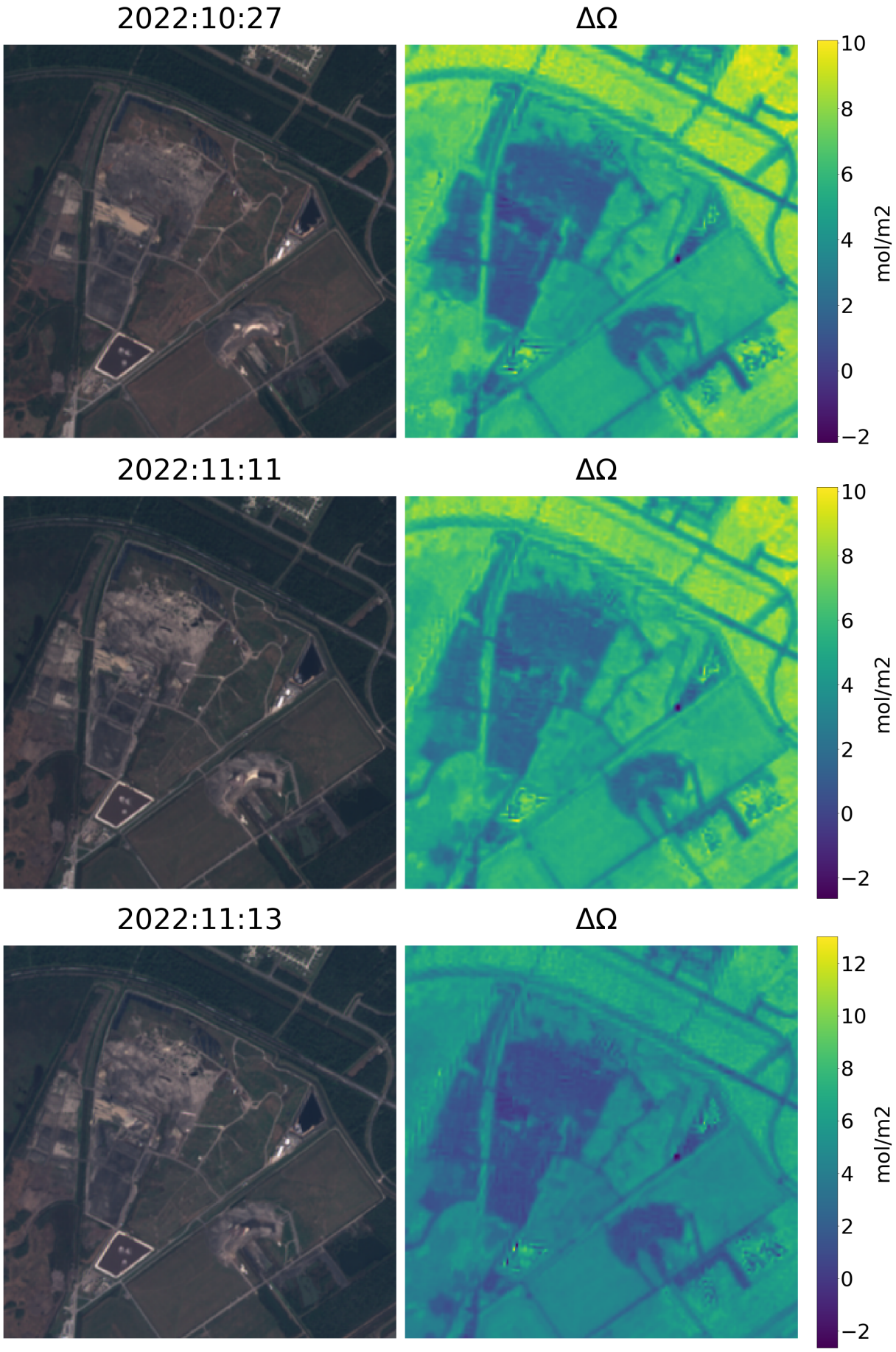
2022:10:27
ΔΩ
10
8
6
4
2
0
−2
mol/m2
2022:11:11
ΔΩ
10
8
6
4
2
0
−2
mol/m2
2022:11:13
ΔΩ
12
10
8
6
4
2
0
−2
mol/m2

2022:11:18 ΔΩ

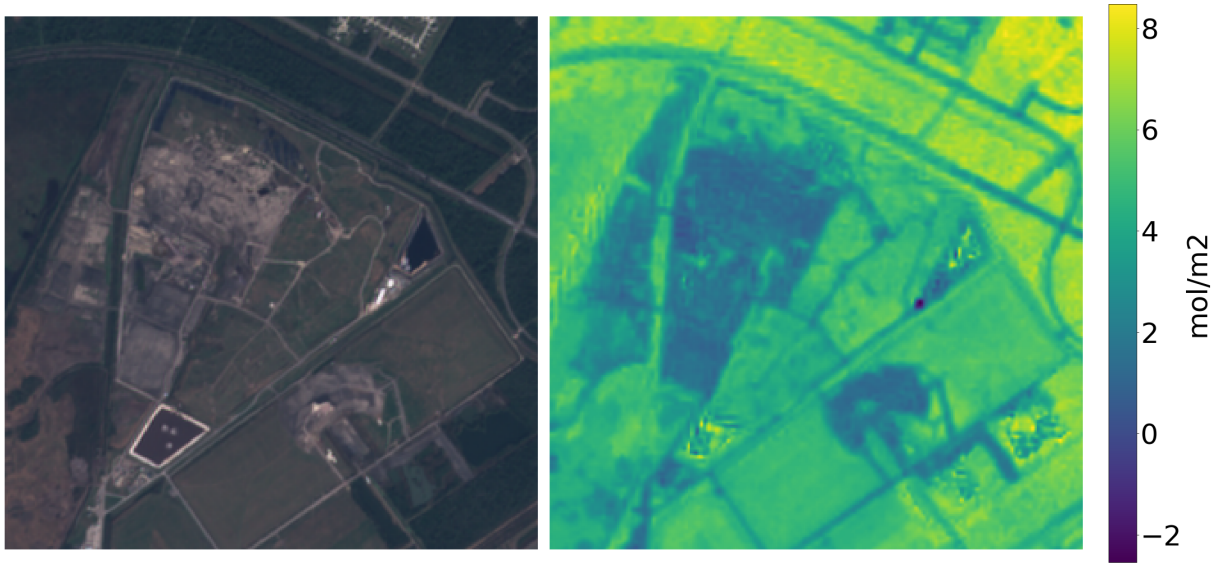

2022:11:21 ΔΩ

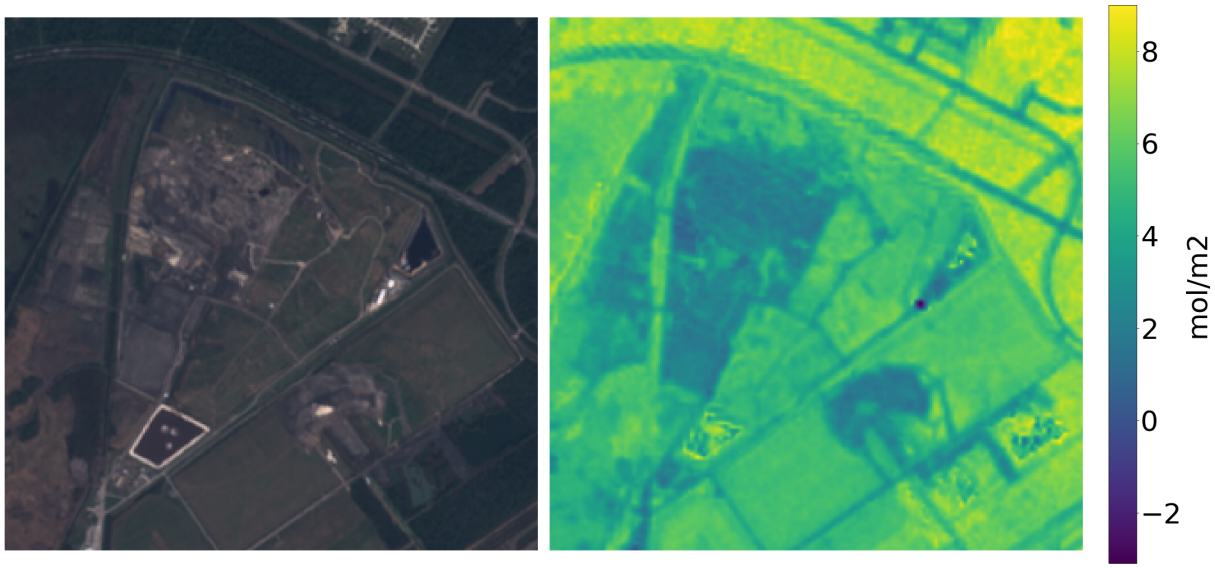

2022:11:23 ΔΩ

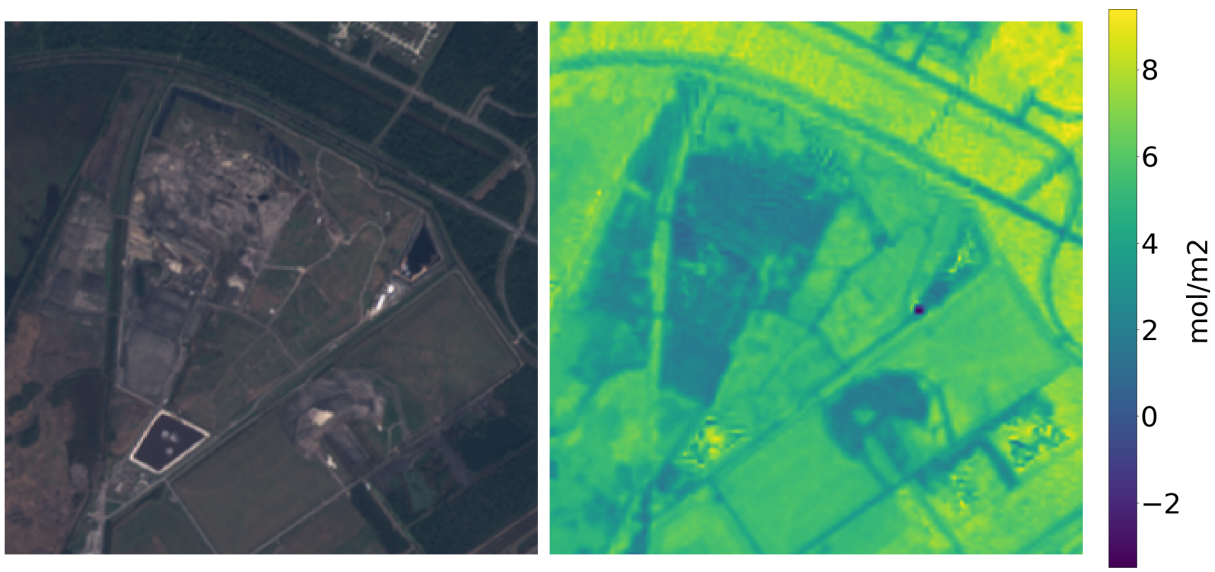

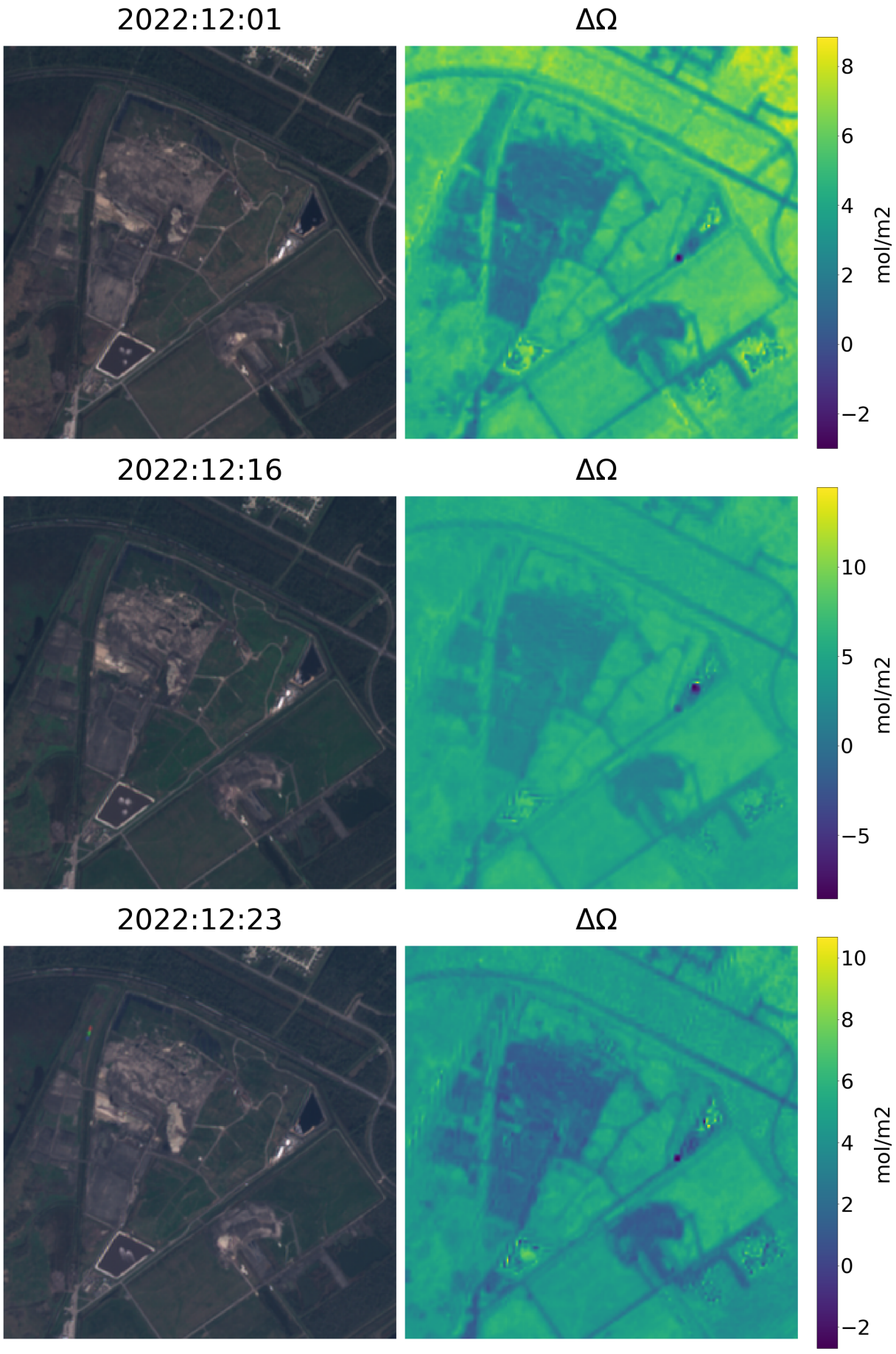
2022:12:01
ΔΩ
8
6
4
2
0
−2
mol/m2
2022:12:16
ΔΩ
10
5
0
−5
mol/m2
2022:12:23
ΔΩ
10
8
6
4
2
0
−2
mol/m2

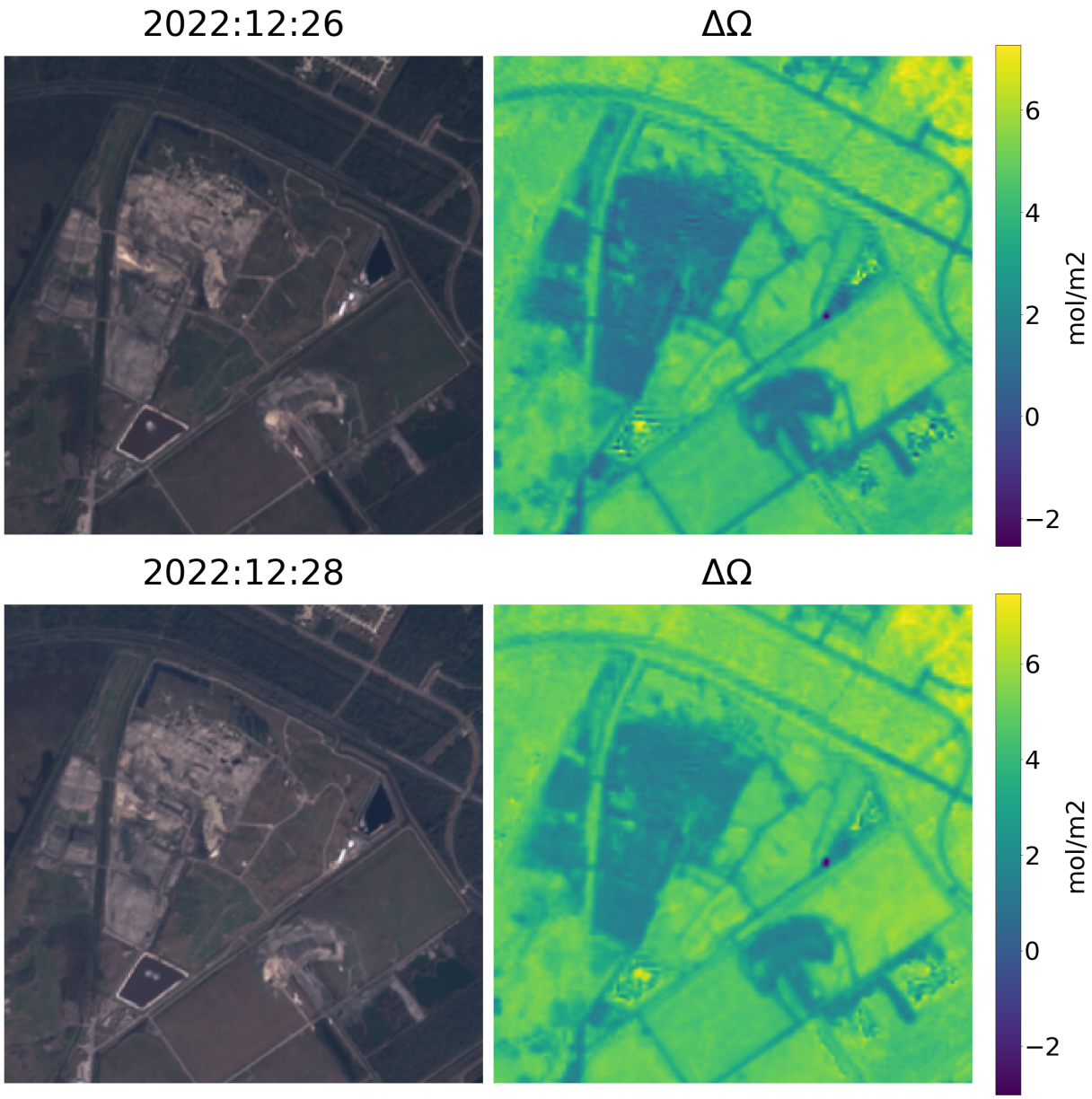
2022:12:26
ΔΩ
6
4
2
0
−2
mol/m2
2022:12:28
ΔΩ
6
4
2
0
−2
mol/m2